JSCSEN 90(6) 709-836(2025)

ISSN 1820-7421(Online)

Journal of the Serbian Chemical Society

Electronic version

VOLUME 90

No 6

BELGRADE 2025

Available on line at

www.shd.org.rs/JSCS/

The **Journal of the Serbian Chemical Society** (formerly Glasnik Hemijskog društva Beograd), one volume (12 issues) per year, publishes articles from the fields of chemistry. The **Journal** is financially supported by the **Ministry of Education, Science and Technological Development of the Republic of Serbia.**
Articles published in the **Journal** are indexed in **Clarivate Analytics products: Science Citation Index-Expanded™** – accessed *via* **Web of Science®** and **Journal Citation Reports®**.
Impact Factor announced on 28 June, 2023: **1.000; 5-year Impact Factor**: **1.100**.
Articles appearing in the **Journal** are also abstracted by: **Scopus, Chemical Abstracts Plus (CAplus℠), Directory of Open Access Journals, Referativnii Zhurnal (VINITI), RSC Analytical Abstracts, EuroPub, Pro Quest** and **Asian Digital Library.**

Publisher:	**Serbian Chemical Society**, Karnegijeva 4/III, P. O. Box 36, 1120 Belgrade 35, Serbia tel./fax: +381–11–3370–467, E-mails: **Society** – shd@shd.org.rs; **Journal** – jscs@shd.org.rs Home Pages: **Society** – http://www.shd.org.rs/, **Journal** – http://www.shd.org.rs/JSCS/
Internet Service:	Contents, Abstracts and full papers (from Vol 64, No. 1, 1999) are available in the electronic form at the Web Site of the **Journal** (http://www.shd.org.rs/JSCS/).
Former Editors:	**Nikola A. Pušin** (1930–1947), **Aleksandar M. Leko** (1948–1954), **Panta S. Tutundžić** (1955–1961), **Miloš K. Mladenović** (1962–1964), **Đorđe M. Dimitrijević** (1965–1969), **Aleksandar R. Despić** (1969–1975), **Slobodan V. Ribnikar** (1975–1985), **Dragutin M. Dražić** (1986–2006).
Editor-in-Chief:	BRANISLAV Ž. **NIKOLIĆ**, Serbian Chemical Society (E-mail: jscs-ed@shd.org.rs)
Deputy Editor:	DUŠAN **SLADIĆ**, Faculty of Chemistry, University of Belgrade
Sub editors:	
Organic Chemistry	DEJAN **OPSENICA**, Institute of Chemistry, Technology and Metallurgy, University of Belgrade JÁNOS **CSANÁDI**, Faculty of Science, University of Novi Sad
Biochemistry and Biotechnology	OLGICA **NEDIĆ**, INEP – Institute for the Application of Nuclear Energy, University of Belgrade
Inorganic Chemistry	BILJANA **GLIŠIĆ**, Faculty of Science, University of Kragujevac
Theoretical Chemistry	MATIJA **ZLATAR**, Institute of Chemistry, Technology and Metallurgy, University of Belgrade MILOŠ **MILIČIĆ**, Faculty of Chemistry, University of Belgrade
Physical Chemistry	LJILJANA **DAMJANOVIĆ-VASILIĆ**, Faculty of Physical Chemistry, University of Belgrade
Electrochemistry	SNEŽANA **GOJKOVIĆ**, Faculty of Technology and Metallurgy, University of Belgrade
Analytical Chemistry	RADA **BAOŠIĆ**, Faculty of Chemistry, University of Belgrade
Polymers	BRANKO **DUNJIĆ**, Faculty of Technology and Metallurgy, University of Belgrade
Thermodynamics	MIRJANA **KIJEVČANIN**, Faculty of Technology and Metallurgy, University of Belgrade
Chemical Engineering	TATJANA **KALUĐEROVIĆ RADOIČIĆ**, Faculty of Technology and Metallurgy, University of Belgrade
Materials	RADA **PETROVIĆ**, Faculty of Technology and Metallurgy, University of Belgrade
Metallic Materials and Metallurgy	ANA **KOSTOV**, Mining and Metallurgy Institute Bor, University of Belgrade
Environmental and Geochemistry	VESNA **ANTIĆ**, Faculty of Agriculture, University of Belgrade
History of and Education in Chemistry	DRAGICA **TRIVIĆ**, Faculty of Chemistry, University of Belgrade
English Language Editors:	LYNNE **KATSIKAS**, Serbian Chemical Society VLATKA **VAJS**, Serbian Chemical Society JASMINA **NIKOLIĆ**, Faculty of Technology and Metallurgy, University of Belgrade
Technical Editors:	VLADIMIR **PANIĆ**, Institute of Chemistry, Technology and Metallurgy, University of Belgrade, MARIO **ZLATOVIĆ**, Faculty of Chemistry, University of Belgrade
Journal Manager & Web Master:	MARIO **ZLATOVIĆ**, Faculty of Chemistry, University of Belgrade
Office:	VERA **ĆUŠIĆ**, Serbian Chemical Society

Editorial Board

From abroad: **R. Adžić**, Brookhaven National Laboratory (USA); **A. Casini**, University of Groningen (The Netherlands); **G. Cobb**, Baylor University (USA); **D. Douglas**, University of British Columbia (Canada); **G. Inzelt**, Etvos Lorand University (Hungary); **J. Kenny**, University of Perugia (Italy); **Ya. I. Korenman**, Voronezh Academy of Technology (Russian Federation); **M. D. Lechner**, University of Osnabrueck (Germany); **S. Macura**, Mayo Clinic (USA); **M. Spiteller**, INFU, Technical University Dortmund (Germany); **M. Stratakis**, University of Crete (Grecce); **M. Swart**, University de Girona (Cataluna, Spain); **G. Vunjak-Novaković**, Columbia University (USA); **P. Worsfold**, University of Plymouth (UK); **J. Zagal**, Universidad de Santiago de Chile (Chile).

From Serbia: **B. Abramović**, **V. Antić**, **R. Baošić**, **V. Beškoski**, **J. Csanadi**, **Lj. Damjanović-Vasilić**, **A. Dekanski**, **V. Dondur**, **B. Dunjić**, **M. Đuran, B. Glišić, S. Gojković**, **I. Gutman**, **B. Jovančićević**, **I. Juranić**, **T. Kaluđerović Radiočić**, **L. Katsikas**, **M. Kijevčanin**, **A. Kostov**, **V. Leovac**, **S. Milonjić**, **V.B. Mišković-Stanković**, **O. Nedić**, **B. Nikolić**, **J. Nikolić**, **D. Opsenica**, **V. Panić**, **M. Petkovska**, **R. Petrović**, **I. Popović**, **B. Radak**, **S. Ražić**, **D. Sladić**, **S. Sovilj**, **S. Šerbanović**, **B. Šolaja**, **Ž. Tešić**, **D. Trivić**, **V. Vajs, M. Zlatović**.

Subscription: The annual subscription rate is **150.00 €** including postage (surface mail) and handling. For Society members from abroad rate is **50.00 €**. For the proforma invoice with the instruction for bank payment contact the Society Office (E-mail: shd@shd.org.rs) or see JSCS Web Site: http://www.shd.org.rs/JSCS/, option Subscription.
Godišnja pretplata: Za članove SHD: **2.500,00 RSD**, za penzionere i studente: **1000,00 RSD**, a za ostale: **3.500,00 RSD**:za organizacije i ustanove: **16.000,00 RSD**. Uplate se vrše na tekući račun Društva: **205-13815-62**, poziv na broj **320**, sa naznakom "pretplata za JSCS".

Nota: Radovi čiji su svi autori članovi SHD prioritetno se publikuju.
Odlukom Odbora za hemiju Republičkog fonda za nauku Srbije, br. 66788/1 od 22.11.1990. godine, koja je kasnije potvrđena odlukom Saveta Fonda, časopis je uvršten u kategoriju međunarodnih časopisa (**M-23**). Takođe, aktom Ministarstva za nauku i tehnologiju Republike Srbije, 413-00-247/2000-01 od 15.06.2000. godine, ovaj časopis je proglašen za publikaciju od posebnog interesa za nauku. **Impact Factor** časopisa objavljen 28. juna 2023. godine je **1,000**, a petogodišnji **Impact Factor 1,100**.

Journal of the Serbian Chemical Society
JSCS-info@shd.org.rs • www.shd.org.rs/JSCS

J. Serb. Chem. Soc. Vol. 90, No. 6 (2025)

CONTENTS*

Published by the Serbian Chemical Society
Karnegijeva 4/III, P.O. Box 36, 11120 Belgrade, Serbia
Printed by the Faculty of Technology and Metallurgy
Karnegijeva 4, P.O. Box 35-03, 11120 Belgrade, Serbia

* For colored figures in this issue please see electronic version at the Journal Home Page: http://www.shd.org.rs/JSCS/

Journal of the Serbian Chemical Society
JSCS@tmf.bg.ac.rs • www.shd.org.rs/JSCS
J. Serb. Chem. Soc. *90* (6) 709–725 (2025)
JSCS–5415
Original scientific paper
Published 23 June, 2025

Green synthesis of silver nanoparticles utilizing *Gardenia latifolia* extract, characterization and *in vitro* antibacterial activity

SATYAM SRIVASTAVA[1], PRASHANSHA SRIVASTAVA[2], GAURAV RAJ DWIVEDI[2], VENKATNARAYAN RAMANATHAN[3] and HARISH CHANDRA UPADHYAY[1]*

[1]*Laboratory of Chemistry, Department of Applied Sciences, Rajkiya Engineering College (affiliated with Dr. A.P.J. Abdul Kalam Technical University, Lucknow), Churk, Sonbhadra-231206, India,* [2]*Department of Microbiology, ICMR – Regional Medical Research Centre, Gorakhpur-273013, India and* [3]*Department of Chemistry, Indian Institute of Technology (BHU), Varanasi-221005, India*

(Received 6 March, revised 11 April, accepted 17 April 2025)

Abstract: Biogenic silver nanoparticle (AgNPs) formulations were synthesized using alcoholic extract from the bark of *Gardenia latifolia* Ait. as a reducing agent and a capping ligand for the silver ions present in an aqueous silver nitrate solution. The synthesis of AgNPs was noted by color, the presence of notable peaks in Fourier-transformed infrared spectra (FT-IR), and Raman spectra. High-resolution transmission electron microscopy (HRTEM) analyses of all the AgNP formulations confirmed the crystalline and spherical characteristics along with smooth surface that was further supported by low particle size (*Zavg*, <50 nm), low polydispersity index (*PDI*), and negative zeta potential. The crude extract and its various fractions did not show significant activity against *Staphylococcus aureus* MTCC-96 and the Methicillin-resistant *S. aureus* (MRSA) clinical isolate, yet in a combinatorial study, a concentration of 10 µg/mL, they reduced the minimum inhibitory concentration (*MIC*) of ethidium bromide (EtBr) to half against the MRSA clinical isolate, supporting the drug resistance reversal property of *G. latifolia* extracts and fractions. The *in vitro* evaluations of AgNP formulations against MRSA, *Staphylococcus epidermidis*, *Escherichia coli* and *Klebsiella pneumoniae* revealed *MIC* ranging from 30.00 to 2.81 µg/mL. Among all, AgNP–**F3** may find its use in the development of cost-effective broad-spectrum antibacterial medications.

Keywords: biofabrication; AgNPs; HR-TEM; MRSA; drug resistance.

* Corresponding author. E-mail: harishcu@recsonbhadra.ac.in
https://doi.org/10.2298/JSC250306029S

INTRODUCTION

Plants and natural substances have traditionally played a vital role in historical medicinal practices, including Ayurveda, traditional Chinese medicine and native American healing, for the treatment of numerous health issues.[1,2] Traditional medicines use a single herb or a combination of two or more herbs as herbal formulations for the treatment of various diseases and debilities.[3] Besides being directly used in remedies, plants have significantly contributed to the advancement of modern medicine, acting as a valuable source of bioactive substances with therapeutic capabilities.[4–6] Throughout history, plants have been essential to traditional medical practices and continue to be a vital source of inspiration and materials for current drug discovery efforts.[7,8] Plants produce a variety of secondary metabolites, including alkaloids, terpenoids, flavonoids and polyphenols, which display a range of biological effects.[9,10] These compounds can function directly as medications or serve as lead compounds for the development of synthetic pharmaceuticals.[11] Although herbal formulations offer advantages, they encounter notable drawbacks, including fluctuations in the concentration of active ingredients that can vary based on the origin of the plant, the time of year, and the methods used for extraction.[12] Additionally, their low solubility and stability lead to poor bioavailability, which restricts their effectiveness in clinical settings.[13,14]

Nanoparticles (NPs) have transformed the fields of drug discovery and development by providing novel approaches to address issues related to drug delivery, effectiveness and safety.[15] These nanoparticles, generally measuring between 1 and 100 nm, display distinctive physicochemical characteristics, such as tiny size, elevated surface area-to-volume ratio and tunable surface chemistry, which renders them highly efficient in improving therapeutic results.[16] Silver nanoparticles (AgNPs) have become a significant area of interest in antimicrobial research owing to their remarkable attributes, such as a wide-ranging antimicrobial action and the capability to fight against antibiotic-resistant microorganisms.[14] Conventional techniques for synthesizing nanoparticles typically involve environmental and health hazards. On the other hand, green synthesis offers a sustainable and economical alternative.[17] The production of AgNPs through bio-fabrication utilizing plant extracts presents a sustainable, economical and environment-friendly option compared to traditional chemical and physical methods.[18] This eco-friendly synthesis method utilizes the inherent reducing, capping, and stabilizing properties found in plant extracts, including flavonoids, alkaloids, phenols and proteins, to generate AgNPs.[13,15]

Gardenia latifolia Ait., also referred to as “Indian boxwood”, is a deciduous tree that belongs to the Rubiaceae family.[19] This plant is indigenous to the tropical and subtropical areas of India, Bangladesh and Southeast Asia.[20] It is well--known in traditional medicine practices for its ethnomedicinal uses and is

known with many vernacular names, *viz*. Papra and Ban pindalu (Hindi), Parpataki (Sanskrit), Varkura (Bengali), Ghogari (Marathi), and Pedda bikki and Peddakaringuva (Telagu).[21] The various plant parts of *G. latifolia* are used to cure a variety of diseases as folklore remedies by villagers and tribes, as well as in well--developed Ayurveda and Siddha systems.[21–24] The leaves of *G. latifolia* are used to cure snake bites.[21] The stem bark extract with pepper and garlic is given in the treatment of fever.[24] The bark of *G. latifolia* is also used to cure skin diseases,[22] stomach troubles, constipation and caries.[25] The resinous sap extracted from the stem tips is applied to the sores of the hands and feet in the rainy season.[25] Fruit paste is given to cure amoebiasis, and the gum is used to cure cutaneous diseases.[25] The root is useful in the treatment of heavy bleeding during the menstrual cycle while the seed along with the leaf of the piper is taken for regular menstruation in women.[26] In the Ballari district of Karnataka (India), fruit pulp is used to cure fever.[27] The alcoholic extracts of the leaf, bark, and fruit of *G. latifolia* showed potent antioxidant and anti-inflammatory properties, which were later supported by the presence of glycosides, flavonoids, phenols, saponins, tannin and anthraquinones in phytochemical investigations.[21] In Bangladesh, different parts of *G. latifolia* are reported to be used traditionally in the treatment of a wide range of human diseases such as stomach pain, fevers, skin diseases, snake bites, inflammatory pain, caries, hemorrhage and ephemeral fever.[19] The leaf extract of *G. latifolia* showed analgesic, antipyretic, *α*-amylase enzyme inhibition, membrane stabilizing, antioxidant effect and antimicrobial activities.[28] There are several reports on the biological activity of fruit extracts of *G. latifolia*.[20,29] Despite a few reports on the fruits and leaf extract of *G. latifolia*, there is no detailed report on the phytochemical investigations and biological activity of the bark extract. In given frame of context, the present work deals with the primary phytochemical screening of *G. latifolia* bark extract, a sustainable synthesis of AgNPs using *G. latifolia* bark extract, characterization and antibacterial activity assessment of extracts and AgNPs for their possible use in the development of a broad-spectrum, cost-effective antibacterial formulation for treating multidrug-resistant bacterial infections.

EXPERIMENTAL

Chemicals and reagents

The solvents used in the extraction and fractionation were purchased from Merck/ /Thermo Fisher, India, Pvt. Ltd. Silver nitrate (analytical grade) and water (HPLC grade) used for the synthesis of AgNPs were purchased from Loba Chemie Pvt. Ltd., India. All the other chemicals and reagents were of analytical/synthetic grade, procured from Sigma–Aldrich Pvt. Ltd., India. All the solvents and reagents were used without further purification.

Collection of plant material

The authenticated samples of *G. latifolia* stem bark were collected in October 2023 from the Hathi Nala forest area of Sonbhadra (24°18'8.43"N and 83°5'31.8"E), Uttar Pradesh, India,

under the supervision of Dr. Deepak Gond, Department of Botany, C.M.P. College, University of Allahabad, India.

Extraction and fractionation

The bark of *G. latifolia*, which was shade-dried and ground into a powder, underwent extraction and fractionation following the previously outlined procedure (Fig. S-1 of the Supplementary material to this paper).[14,30] In summary, 1.2 kg of plant material was extracted three times using 2 L of methanol, and the solvent was removed under a vacuum with a rotary evaporator-chiller (Buchi, India) to produce methanolic extract. Next, the dried extract was dissolved in warm-distilled water and successively partitioned with 500 mL of *n*-hexane, chloroform and *n*-butanol three times each, with the collected fractions being dried separately under a vacuum, resulting in *n*-hexane, chloroform and *n*-butanol fractions (Fig. S-1).

Phytochemical investigation of the methanolic extract

The thin-layer chromatography (TLC) profile of the crude extract and the fractions of hexane, chloroform and *n*-butanol were individually analyzed on ready-made TLC plates (silica gel $60F_{254}$, Merck, India) in different solvent systems to assess the presence of phytoconstituents preliminary. The developed TLC plates were initially observed under UV light at 254 and 365 nm, then treated with a vanillin–sulphuric acid (1:5) solution in ethanol and subsequently heated at 95 °C for 5 min for visualization. Further, the analysis of the alcoholic extract was conducted to assess the presence of secondary metabolites utilizing standard methods.[9,31]

Synthesis of AgNPs

A 1 % *G. latifolia* bark extract was made by dissolving 1 g of the dried methanolic extract in 100 ml of ethanol, followed by sonication for 20 min using an ultrasonic cleaner (Science Tech, India) and subsequent filtration. A green synthetic method using a bottom-up approach was utilized, employing different concentrations (2 and 3 mM) of aqueous silver nitrate ($AgNO_3$) solution along with various volumes (25 and 50 μL) of 1 % plant extract solution to determine the optimal combination with suitable colloidal characteristics. To begin with, 3.5 mL of 2 mM and 3 mM $AgNO_3$ solutions were separately combined drop by drop with 25 μL/50 μL of the plant extract, and the total volume was brought up to 4 mL using millipore water, resulting in the final extract concentrations of 62.5/125 μg/mL. All four reaction mixtures were placed in screw-capped glass vials and maintained on an orbital shaker (Remi, India) for 24 h, during which they were continuously monitored for any color changes, indicating the formation of AgNPs. Following the incubation period, color alterations were noted and verified using spectroscopy. Afterward, each formulation was centrifuged and rinsed three times with Millipore water and then redeveloped.

Characterization of AgNPs

Organoleptic properties. Initially, the samples were observed visually to detect any color changes, the presence of aggregates, and levels of turbidity.

Raman spectroscopy. The Raman spectra were recorded using an alpha-300 Access confocal Raman spectrometer (WITec, Germany) that featured a UHTS 300S_VIS spectrometer with a 600 g/mm BLZ 500 nm grating. Excitation lasers of 532 nm at 3–5 mW power were employed. Subsequently, the data were processed for noise removal and baseline correction using polynomial functions.

Fourier-transformed infrared (FT-IR) spectroscopy. Fourier-transformed infrared spectra (FT-IR) spectroscopy was performed using a Nicolet iS5 spectrometer (Thermo Fisher Sci-

entific, USA) within the range of 400–4000 cm^{-1}, where samples were directly added to the diamond surface and the spectra were recorded considering water as the solvent for blank.

High-resolution transmission electron microscopy (HRTEM) and selected area electron diffraction (SAED). The surface morphology and SAED pattern of samples were investigated by HRTEM (FEI, TECNAI G2, USA) equipped with a HAADF detector at 200 kV. In HRTEM analysis, the sample was diluted five times with ultrapure water, and one drop of the samples was placed on a carbon-coated copper grid. The excess water was soaked with clean filter paper and dried overnight to remove the residual water.

Dynamic light scattering (DLS) analysis. Particle size (*Zavg*), polydispersity Index (*PDI*) and zeta potential (*ZP*) of AgNPs were measured by DLS method on Zetasizer Ultra (ZSU5700, Malvern Panalytical Ltd., UK) at 25°C.

In vitro *antibacterial activity*

Procurement of bacterial strains. The pathogenic *Staphylococcus aureus* MTCC-96, clinical isolates of *S. aureus (*which was resistant to methicillin and named MRSA), *Staphylococcus epidermidis*, *Klebsiella pneumoniae* and *Escherichia coli* were obtained from the ICMR-RMRC, Gorakhpur repository. Mueller–Hinton agar and broth (MHA and MHB, Hi-Media, Mumbai, India) were employed as media for bacterial culturing. Colony counts were assessed utilizing MHA plates.

Antibacterial activity assessment. The minimum inhibitory concentrations (*MIC*s) were established using a twofold serial dilution broth method in Mueller–Hinton broth using 96--well microtiter plates following the guidelines set by the Clinical & Laboratory Standards Institute (CLSI) for broth micro-dilution.[32,33] The extracts and fractions were diluted to achieve final concentrations ranging from 1000 to 1.95 μg/mL, and they were evaluated against *S. aureus* MTCC-96 and MRSA strains. In the study involving AgNPs, the strains of MRSA, *S. epidermidis*, *K. pneumoniae* and *Escherichia coli* were tested using a 30 μL aliquot from each (2/3 mole, aqueous) sample as the stock solution, which ensured concentrations of 30 μg/mL of AgNPs for samples **F1** and **F2** and 45 μg/mL of AgNPs for samples **F3** and **F4** as their initial concentrations. The starting inoculum concentration was 5×10^5 cfu/mL. The inoculated plates were incubated at 37 °C for 24 h, after which visual assessments were made, and the *MIC* was noted as the final dilution that showed no turbidity in accordance with CLSI guidelines. Ciprofloxacin was used as a positive control.

Combinatorial study. The combination experiments at a fixed 10 μg/mL concentration of extract and fractions were conducted using ethidium bromide (EtBr) concentrations between 0.48 and 250 μg/mL.[2,34] The microtitre plates were incubated with 10 μL of a diluted overnight culture of the test organism MRSA, adjusted to a titer equivalent to the 0.5 McFarland standard. Following inoculation, the microtitre plates were incubated at 37 °C for 24 h.[4]

RESULTS AND DISCUSSION

Phytochemical investigations

A methanolic extraction from 1.2 kg of shade-dried and ground bark of *G. latifolia* resulted in 84 g of a dried extract. Furthermore, the fractionation of 60 g dried methanolic extract yielded *n*-hexane (2.5 g), chloroform (0.6 g), and *n*-butanol (13.2 g) fractions (Fig. S-1). The TLC of the extract and its fractions in several combinations of hexane, chloroform, and methanol revealed the presence of plant secondary metabolites (Fig. S-2 of the Supplementary material). The

phytochemical investigation of the crude methanolic extract of *G. latifolia* bark revealed the existence of saponins, tannins, glycosides, terpenoids, phenolic compounds and flavonoids; nonetheless, alkaloids were not found in the crude extract (Table S-I of the Supplementary material). The results are more or less consistent with previous research reporting several bioactive groups of compounds in the extracts obtained from various parts of *G. Latifolia*.[21,35,36]

Synthesis of AgNPs

The eco-friendly and sustainable approach of synthesizing AgNPs with plant extracts serves as a cost-efficient alternative to traditional chemical methods.[14,16,18] This method provides greater biocompatibility, minimizes toxicity, decreases energy usage, and improves biological characteristics, making it suitable for use in medicine, agriculture and environmental science.[13,15] Using aqueous silver nitrate as a source for silver cations, the initial step includes reducing Ag^+ to Ag by utilizing plant secondary metabolites such as flavonoids, phenols, alkaloids, terpenoids and proteins to provide electrons.[37] After the metallic Ag is generated, it begins to aggregate into tiny clusters of 15–2000 atoms, which are subsequently enclosed by capping agents that are, in turn, the secondary metabolites of the plant.[38]

In our initial phytochemical studies, the bark extract of *G. latifolia* showed the presence of various types of bioactive secondary metabolites with hydroxyl, carboxylic and carbonyl groups, which could effectively reduce and cap silver ions.[20,35] To determine the optimal concentration of extract and silver ions, four different formulations were synthesized using 3.5 mL of 2 or 3 mM silver nitrate solution along with 25/50 μL of 1 % alcoholic extract from the bark of *G. latifolia* (Table I).

TABLE I. The concentrations of $AgNO_3$ and *G. latifolia* bark extract in various AgNP-formulations

AgNP-formulation	3.5 mL of $AgNO_3$, mM	1 % alcoholic extract, μL
F1	2	25
F2	2	50
F3	3	25
F4	3	50

Characterization of AgNPs

The initial sign in the formation of metal nanoparticles is a color change, which occurs because of the vibration of the plasmon base, a unique optical characteristic of noble metals.[16] In this study, the synthesis of AgNPs involved the gradual addition of the extract to the $AgNO_3$ solution accompanied by continuous shaking. This process resulted in a color change of the reaction mixture from colorless to brown, indicating the formation of AgNPs (Fig. 1).

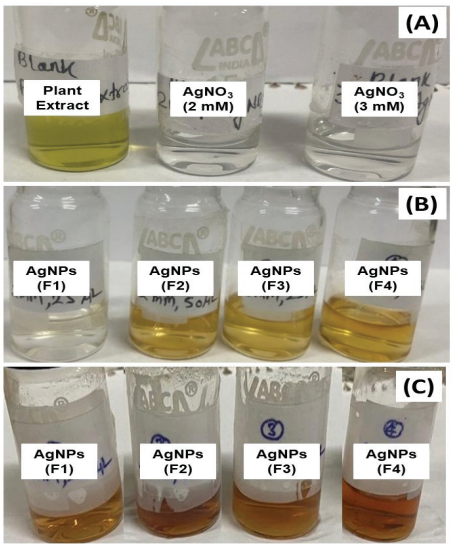

Fig. 1. Organoleptic changes observed in the reaction mixture during green synthesis of AgNPs before incubation (A) AgNP formulations after 1 h (B), and AgNP formulations after 24 h (C).

FT-IR spectroscopy. FT-IR, a technique that detects significant functional groups in plant extracts, serves as a crucial method for characterizing biofabricated AgNPs. Nanoscale silver particles synthesized through biofabrication are generally stabilized by phytochemicals that interact with the surfaces of the metal at a molecular level.[39] FT-IR analysis serves as a tool to investigate the characteristics of these molecular interactions and the associated functionalities, as noted in previous studies referencing specific functional group peaks.[14] In the present study, this examination might also reveal how silver nitrate engages with the secondary metabolites present in the bark extract of *G. latifolia*, which function as reducing and capping agents. A change in peak absorption or intensity indicates that a reaction has occurred between silver ions and the plant secondary metabolites containing functional groups, leading to the synthesis of nanoparticles. The FT-IR absorbance bands of the extract and the AgNP formulations in the range of 500 to 4000 cm^{-1} are presented in Fig. 2. The analysis revealed absorbance peaks at 3407, 2927, 2854, 1685, 1629, 1520, 1456, 1281, 1075 and 1048 cm^{-1}, primarily indicating the presence of carbonyl, alcoholic, and phenolic functional groups. A thorough examination of the FT-IR spectrum for the produced AgNPs revealed a strong and broad peak at 3452 (AgNP-F1), 3431 (AgNP-F2 and AgNP-F3) and 3442 (AgNP-F4), which appears to have shifted from 3407, the prominent peak of the extract. The significant peak observed at 1384 cm^{-1} could be attributed to the C–N stretching of secondary amines, amino acids, peptides, and proteins present in the plant extract, which might form a layer around the synthesized silver to serve as a capping agent.[40] The spectra of synthesized AgNPs revealed a few additional prominent and broad surface plas-

mon peaks ranging from 1400 to 1700 cm^{-1}, representing a significant band peak for silver ions.[16,18]

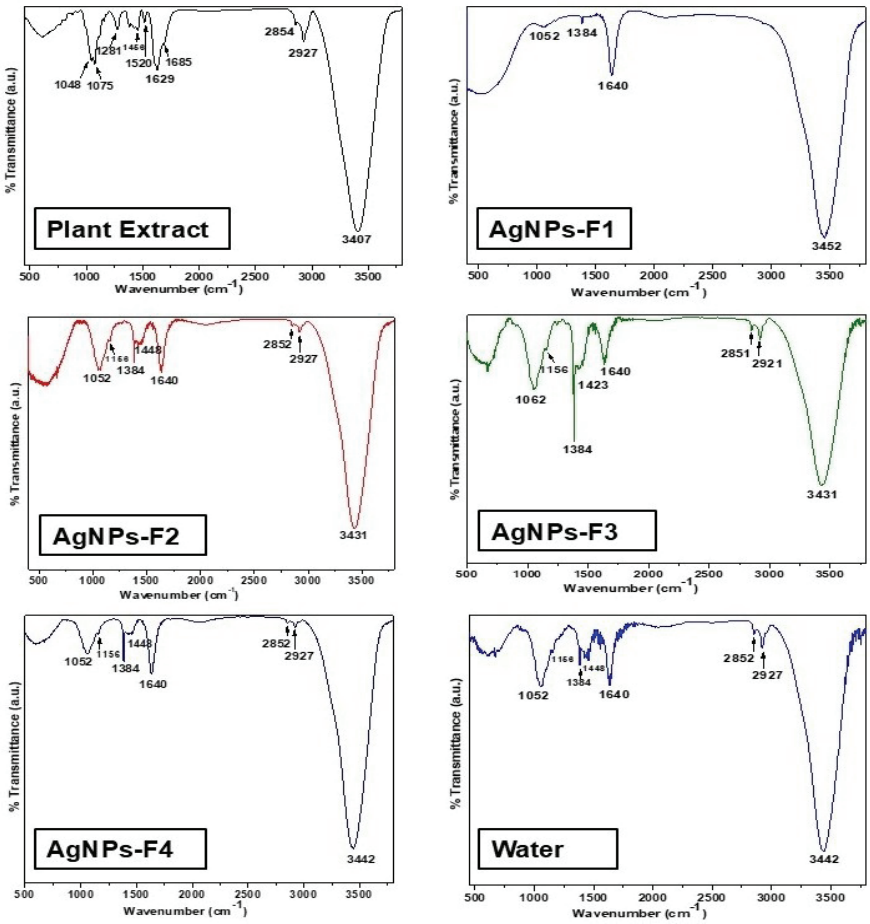

Fig. 2. Fourier transform infrared spectrum of plant extract and AgNP formulations.

Raman spectroscopy. Raman spectroscopy serves as an effective tool for analyzing AgNPs because of their distinctive surface-enhanced Raman scattering (SERS) characteristics. This enhancement takes place when molecules attach to the surface of silver nanoparticles, rendering it particularly beneficial for detecting chemical species and functional groups that are attached to the surface and play a role in the synthesis or stabilization process.[41] Raman spectroscopy was utilized over a spectrum from 200 to 4000 cm^{-1} to detect any possible changes in the reaction spectra leading to the synthesis of AgNPs (Fig. 3). In the case of the aqueous silver nitrate solution, no distinct peak was found in the range of 200–

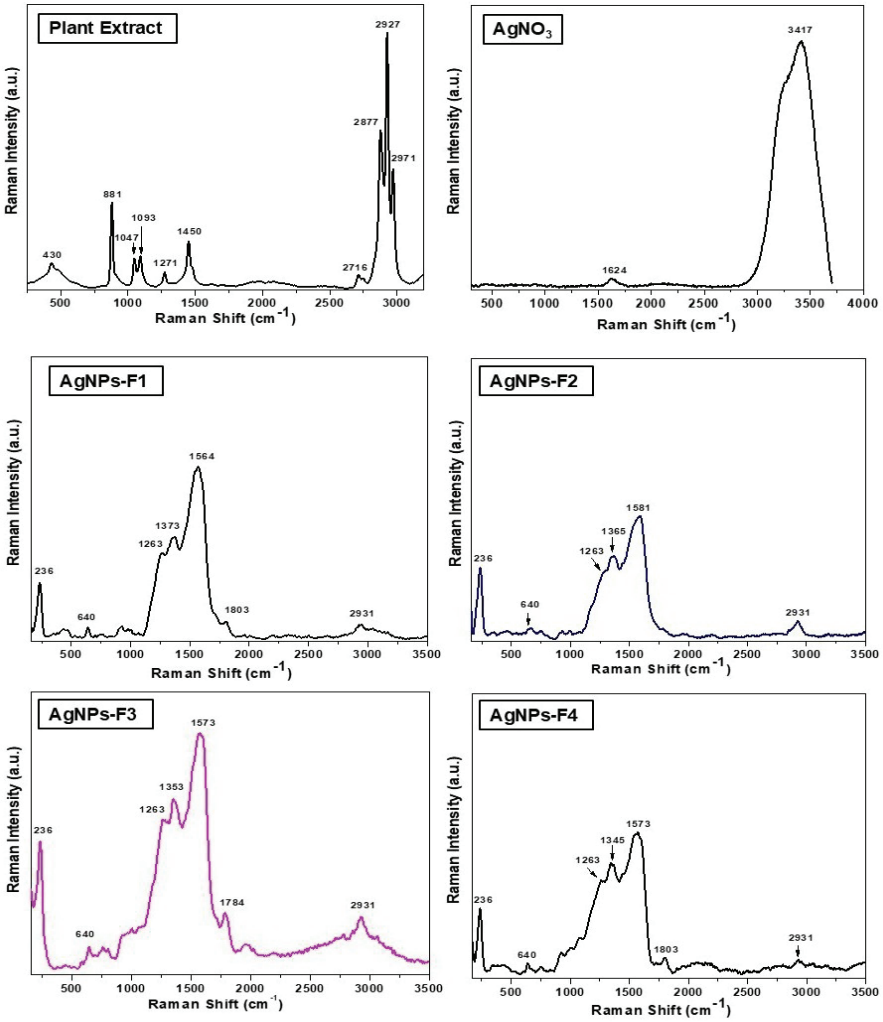

Fig. 3. Raman spectrum of plant extract and AgNP formulations.

–1500 cm^{-1}, suggesting that there were no organic components present. In contrast, the alcoholic extract exhibited distinct peaks for carbohydrates at 430, 881, 1047 and 1093 cm^{-1}, along with a pronounced peak probably for the phosphate group in DNA at 1271 cm^{-1}. Additionally, there were higher-frequency bond vibrations related to CH, NH and OH stretching in lipids at 2716, 2877, 2927 and 2971 cm^{-1}, which is supported by the literature.[42] The AgNP formulations revealed through Raman spectroscopy a fingerprint region ranging from 400 to 1500 cm^{-1}, along with the emergence of a pronounced peak at 236 cm^{-1}, attributed to the O=Ag_2/Ag–N stretching vibrations, which further confirms the conversion of Ag^+ to Ag.[43,44] The Raman spectrum exhibited prominent peaks at 1373 cm^{-1}

and 1564 cm^{-1} for the biosynthesized AgNP-F1, at 1365 and 1581 cm^{-1} for the biosynthesized AgNP-F2, at 1353 and 1573 cm^{-1} for the biosynthesized AgNP–**F3**, and at 1345 and 1573 cm^{-1} for the biosynthesized AgNP–**F4**, corresponding to the D and G bands. This is indicative of organic materials derived from the plant extract that function as capping agents.[41]

HR-TEM and SAED analysis. HR-TEM and SAED offer essential information regarding the nanoscale sizes, shapes, crystallinity and structural characteristics of the synthesized nanoformulations. The arrangement of spots in the chosen area diffraction pattern creates the TEM image, where each spot signifies a fulfilled diffraction state of the crystalline structure of the nanoparticle.[45] The various diffraction spots corresponding to different diffraction states reflect the crystallinity of the specimen. The HR-TEM photomicrographs of the produced AgNP formulations distinctly exhibited the presence of uniformly shaped spherical AgNPs with smooth surfaces, maintaining a consistent distance from one another, except for a few agglomerated AgNPs observed in certain areas of the AgNP formulation **F2** and occasionally in **F4** (see Figs. S3 and S4 of the Supplementary material). It was noted that the AgNP formulations created with a smaller quantity of plant extract (**F1** and **F3**) demonstrate consistent size and distribution of AgNPs with smooth surfaces (Fig. 4).

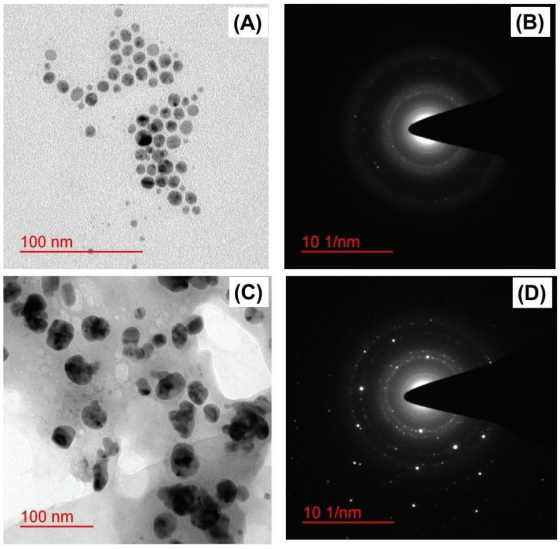

Fig. 4. HRTEM photomicrograph of: AgNP–**F1** (A) and AgNP–**F3** (C), SAED spot pattern of AgNP–**F1** (B) and AgNP–**F3** (D).

DLS analysis. DLS analysis is a reliable and economical method for determining the diffusion coefficient of suspended nanoparticles in a solution undergoing Brownian motion by analyzing the fluctuations in light intensity scattered

by the nanoparticles in the medium.[45] The intensity of the scattered light is inversely proportional to the diffusion coefficient of the nanoparticles and provides information on the hydrodynamic size of the nanoparticles. The average particle size (*Zavg*), polydispersity index (*PDI*) and zeta potential (*ZP*) of silver nanoparticles (AgNPs) were assessed through DLS techniques in bio-fabricated AgNP solutions, and all the relevant data is presented in Figs. S-5–S-8 of the Supplementary material. The *Zavg* indicates the mean diameter of nanoparticles in a sample, which was measured at 32.3±0.109 nm for formulation **F3** and 47.2±0.243 nm for formulation **F4** of the synthesized AgNPs. The *Zavg* values observed in this research are considered optimal for extract-mediated AgNPs.[14] The *PDI* is a dimensionless metric that indicates the uniformity of the particle size distribution in a sample. It is calculated based on the width of the size distribution curve. A lower *PDI* value approaching zero indicates that the nanoparticle sample is monodispersed, suggesting that the particles have comparable sizes, which is essential for the biological activity of extract-mediated AgNPs.[14] The *PDI* of the synthesized AgNP formulations **F3** and **F4** was measured at 0.102±0.0003, and 0.182±0.0002 respectively, suggesting a uniform distribution of the small-sized AgNPs. ZP refers to the electric potential at the particle surface, which is an indicator of the stability of nanoparticle dispersions. A high zeta potential indicates strong electrostatic repulsion between nanoparticles, which prevents aggregation and leads to better stability in suspension. The AgNP formulations **F3** and **F4** showed *ZP* at –20.65±0.897 and –5.657±1.023 mV (Fig. 5), hence may be considered to have appreciable stability in colloidal systems. Based on its smaller average particle size, lower *PDI*, and higher negative zeta potential, the AgNP formulation **F3** is deemed the optimal nanoformulation produced through a green synthesis method utilizing *G. latifolia* bark extract.

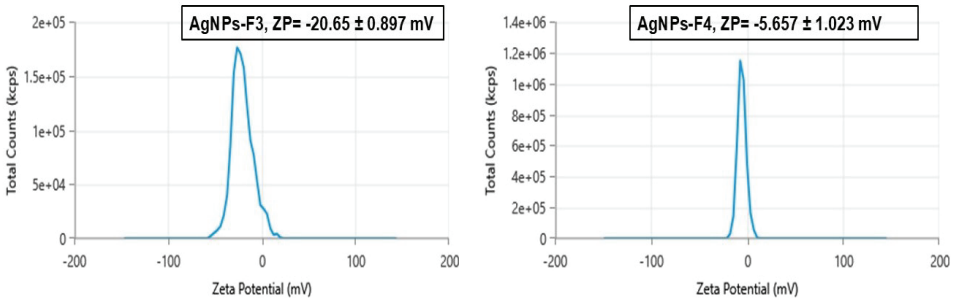

Fig. 5. Zeta potential of AgNP formulations **F3** and **F4**.

Antibacterial activity of extract, fractions and AgNPs

The crude methanolic extract of the bark of *G. latifolia* did not show any inhibitory effect on the *S. aureus* MTCC-96, and the MRSA clinical isolate (*MIC*

> 1000 μg/mL). Further, the medium polar chloroform fraction showed nominal activity (*MIC* = 1000 μg/mL) against *S. aureus* MTCC-96 while the non-polar hexane fraction and the polar n-butanol fraction were found inactive against both the *S. aureus strains* (*MIC* > 1000 μg/mL). In a combinatorial investigation, a concentration of 10 μg/mL of extracts and fractions was applied to evaluate a reduction in the *MIC* of EtBr against the MRSA clinical isolate. The crude methanolic extract and hexane and chloroform fractions reduced the *MIC* of EtBr to half (Table II), showing a synergistic effect with EtBr. The results suggest that the extract of the bark of *G. latifolia* may find its use in overcoming the drug resistance caused by *S. aureus* by inhibiting bacterial efflux pumps.

TABLE II. *In vitro* antibacterial activity of *G. latifolia* extract and fractions; Extr.: crude alcoholic extract, Fract.: fractions of crude extract, GL: crude alcoholic extract of *G. latifolia* bark, GLH: hexane fraction, GLC: chloroform fraction, GLB: *n*-butanol fraction, EtBr: ethidium bromide, Cipro.: ciprofloxacin

Extr./Fract.	*MIC* / μg mL^{-1} against *S. aureus* strains		
	MTCC-96	MRSA	EtBr against MRSA in combination with 10 μg/mL Extr./Fract.
GL	>1000	>1000	3.90
GLH	>1000	>1000	3.90
GLC	1000	>1000	3.90
GLB	>1000	>1000	15.62
EtBr	–	7.81	–
Cipro.	0.19	7.80	–

To evaluate the antibacterial effectiveness of the synthesized AgNP formulations, two strains of each gram-positive MRSA clinical isolate and *S. epidermidis*, as well as gram-negative *E. coli* and *K. pneumoniae*, were utilized under *in vitro* conditions. The measured *MIC* values varied from 30.00 to 2.81 μg/mL (Table III). The AgNP formulation **F3** exhibited demonstrated *MIC* values of 11.25, 2.81, 11.25 and 11.25 μg/mL, while the formulation **F1** demonstrated a *MIC* of 15.00, 3.75, 15.00 and 15.00 μg/mL against the MRSA, *S. epidermidis*, *E. coli* and *K. pneumoniae*, respectively. Among all formulations, AgNP formulation **F3** exhibited the strongest antibacterial activity against all the tested bacterial strains.

Concerning the positive control ciprofloxacin (*MIC* = 7.80 μg/mL), the *MIC* of AgNP–**F3** was measured at 11.25 μg/mL, which was the highest among all the AgNP formulations. The antibacterial effectiveness of AgNP–**F3** was observed to be over 11 times greater against the gram-positive *S. epidermidis* (*MIC* = 2.81 μg/mL) and more than 5 times greater against the gram-negative *E. coli* (*MIC* = 11.25 μg/mL) in comparison to ciprofloxacin, which exhibited *MIC* values of 31.25 and 62.5 μg/mL, respectively, for both bacterial strains. The antibacterial efficacy of AgNP–**F3** against the gram-negative bacterium *K. pneumoniae* (*MIC*

= 11.25 μg/mL) was significantly lower than that of ciprofloxacin (*MIC* = 0.97 μg/mL), yet it was the most potent among all AgNP formulations. The remarkable antibacterial effectiveness of the AgNP formulation **F3** (synthesized by reacting 3.5 mL of 3 mM aqueous $AgNO_3$ with 25 μL of 1 % plant extract) can be linked to the higher concentration of homogenous extract-stabilized AgNPs without aggregation in atom clusters. Despite the silver ion concentration being consistent, increasing the amount of extract (as in the case of **F2** and **F4**), plausibly due to a higher concentration of secondary metabolites, aggregation of silver atoms in the cluster has taken place, which is evident in HR-TEM analysis. It is evident that with an increase in size, the nano characteristic diminishes, leading to a decrease in antibacterial activity.

TABLE III. *In vitro* antibacterial activity of *G. latifolia* bio-fabricated AgNPs

AgNP Formulation	*MIC* / μg mL^{-1} against:			
	MRSA	*S. epidermidis*	*E. coli*	*K. pneumoniae*
F1	15.00	3.75	15.00	15.00
F2	30.00	7.50	15.00	30.00
F3	11.25	2.81	11.25	11.25
F4	22.50	5.63	22.50	22.50
$AgNO_3$	15.00	7.50	30.00	30.00
Ciprofloxacin	7.80	31.25	62.50	0.97

The antibacterial effect of AgNPs can occasionally surpass those of traditional antibiotics like penicillin, especially for those dealing with the resistance shown by various microbial strains to these antibiotics.[46,47] AgNPs demonstrate promising antibacterial properties through a distinctive mechanism that simultaneously affects multiple targets, leading to the death of various bacterial strains.[45,48] Due to their composition of 20–15,000 silver atoms and typically having a diameter of less than 100 nm, AgNPs possess a significant surface area that enables them to interact with proteins on bacterial surfaces and compromise the integrity of the cell wall.[49] Although the mechanism of action of AgNPs still needs to be explored, numerous studies suggest that the exceptional antibacterial properties of AgNPs can be linked to their extremely small size and increased surface area, allowing them to effectively disrupt membranes, enter microbial cells, and subsequently transform into silver ions within the cytoplasm, leading to damage to the internal structures as a secondary effect.[49] The production of free radicals by AgNPs could be regarded as an additional method for the elimination of bacterial cells. These free radicals harm the bacterial cell membrane, causing it to become porous, which ultimately results in cell death.[50,51] It has been noted that the engagement of AgNPs with the sulfur and phosphorus present in bacterial DNA can cause problems in DNA replication, ultimately leading to the termination of the microbes.[50,51] Moreover, the phytochemicals of the plant extract

as the capping ligand in the biofabricated AgNPs might be greatly enhancing the biological activity by interacting synergistically with AgNPs.

CONCLUSION

A rapid and environment-friendly protocol for the bio-fabrication of silver nanoparticles has been developed using *G. latifolia* bark extract, providing a superior alternative to traditional chemical and physical methods. The formation of AgNPs was monitored using FT-IR and Raman spectroscopy. The final characterization of the AgNPs was performed through HR-TEM, SAED, and DLS analysis, which confirmed that the extract-stabilized AgNPs were optimally sized, with a smooth surface and uniform distribution. However, the plant bark extract and fractions exhibited only moderate drug-resistance reversal potential against MRSA, the synthesized AgNPs displayed noteworthy antibacterial properties when tested *in vitro* against both gram-positive and gram-negative bacterial strains. Among all the formulations tested, AgNP–**F3** demonstrated the most favorable characteristics for extract-encapsulated AgNPs and displayed the highest antibacterial efficacy against both the gram-positive methicillin-resistant *S. aureus* clinical isolate and *S. epidermidis*, as well as the gram-negative strains *E. coli* and *K. pneumoniae*. The antibacterial potency of AgNP–**F3** was found to be more than 11 times superior against the gram-positive *S. epidermidis* and over 5 times more effective against the gram-negative *E. coli* when compared to the antibiotic ciprofloxacin. We recommend conducting further *in vivo* investigations of AgNP formulation **F3** for its development as a broad-spectrum antibacterial agent.

SUPPLEMENTARY MATERIAL

Additional data and information are available electronically at the pages of journal website: https://www.shd-pub.org.rs/index.php/JSCS/article/view/13282, or from the corresponding author on request.

Acknowledgements. The financial assistance provided by DRDO-LSRB, India research project #413 is sincerely acknowledged. Satyam and Harish thank the Director of Rajkiya Engineering College, Sonbhadra, for his constant encouragement and for providing all types of facilities for this study.

ИЗВОД

ЗЕЛЕНА СИНТЕЗА НАНОЧЕСТИЦА СРЕБРА ПРИМЕНОМ ЕКСТРАКТА *Gardenia latifolia*, ЊИХОВА КАРАКТЕРИЗАЦИЈА И *IN VITRO* АНТИБАКТЕРИЈСКА АКТИВНОСТ

SATYAM SRIVASTAVA[1], PRASHANSHA SRIVASTAVA[2], GAURAV RAJ DWIVEDI[2], VENKATNARAYAN RAMANATHAN[3] и HARISH CHANDRA UPADHYAY[1]

[1]Laboratory of Chemistry, Department of Applied Sciences, Rajkiya Engineering College (Affiliated with Dr. A.P.J. Abdul Kalam Technical University, Lucknow), Churk, Sonbhadra-231206, India, [2]Department of Microbiology, ICMR - Regional Medical Research Centre, Gorakhpur-273013, India и [3]Department of Chemistry, Indian Institute of Technology (BHU), Varanasi-221005, India

Биогене форме наночестица сребра (AgNP) су синтетисане применом алкохолног екстракта коре *Gardenia latifolia* као редукујућег агенса и лиганда за јоне сребра из воденог раствора сребро нитрата. Синтеза честица AgNP праћена је променом боје и појавом специфичних максимума у FT-IR и Raman спектрима. Методом HRTEM утврђено је да су све AgNP формулације имале кристалну, сферну структуру са глатком површином, то је даље потврђено честицама мале величине (< 50 nm), ниским индексом полидисперзије (*PDI*) и негативним цета потенцијалом. Биљни сирови екстракт и његове фракције нису испољавали значајну активност спрам *Staphylococcus aureus* MTCC-96 и метицилин резистентном клиничком изолату *S. aureus* (MRSA), али у комбинованој студији, концентрација од 10 μg/mL је преполовила *MIC* етидијум-бромида спрам MRSA, указујући на способност *G. latifolia* екстраката и фракција да резистенцију на лек промене у активност. У *in vitro* одређивању активности AgNP формулација спрам MRSA, *Staphylococcus epidermidis*, *Escherichia coli* и *Klebsiella pneumoniae*, добијене су *MIC* вредности у опсегу од 30,00 до 2,81 μg/mL. Формулација AgNP–**F3** исказује потенцијал да се користи у развоју ефикасних антибактеријских лекова широког спектра дејства.

(Примљено 6. марта, ревидирано 11. априла, прихваћено 17. априла 2025)

REFERENCES

1. H. C. Upadhyay, N. Jaiswal, A. K. Tamrakar, A. K. Srivastava, N. Gupta, S. K. Srivastava, *Nat. Prod. Commun.* **7** (2012) 115 (https://doi.org/10.1177/1934578X1200700724)
2. H. C. Upadhyay, G. R. Dwivedi, M. P. Darokar, V. Chaturvedi, S. K. Srivastava, *Planta Med.* **78** (2012) 482 (https://doi.org/10.1055/s-0031-1280256)
3. H. C. Upadhyay, *Curr. Top. Med. Chem.* **19** (2019) 555 (https://doi.org/10.2174/1568026619666190412101047)
4. G. R. Dwivedi, H. C. Upadhyay, D. K. Yadav, V. Singh, S. K. Srivastava, F. Khan, N. S. Darmwal, M. P. Darokar, *Chem. Biol. Drug Des.* **83** (2014) 482 (https://doi.org/10.1111/cbdd.12263)
5. H. C. Upadhyay, B. S. Sisodia, H. S. Cheema, J. Agrawal, A. Pal, M. P. Darokar, S. K. Srivastava, *Nat. Prod. Commun.* **8** (2013) 737 (https://doi.org/10.1177/1934578X1300801123)
6. H. C. Upadhyay, G. R. Dwivedi, S. Roy, A. Sharma, M. P. Darokar, S. K. Srivastava, *ChemMedChem* **9** (2014) 1860 (https://doi.org/10.1002/cmdc.201402027)
7. H. C. Upadhyay, J. P. Thakur, D. Saikia, S. K. Srivastava, *Medic. Chem. Res.* **22** (2013) 16 (https://doi.org/10.1007/s00044-012-9998-9)
8. H. C. Upadhyay, M. Singh, O. Prakash, F. Khan, S. K. Srivastava, D. U. Bawankule, *SN Appl. Sci.* **2** (2020) 2069 (https://doi.org/10.1007/s42452-020-03798-5)

9. H. C. Upadhyay, D. C. Saini, S. K. Srivastava, *Res. J. Phytochem.* **5** (2011) 170 (https://doi.org/10.3923/rjphyto.2011.170.176)
10. K. N. Mishra, M. Rashmi, H. C. Upadhyay, *Ind. J. Pharma. Edu. Res.* **58** (2024) 1242 (https://dx.doi.org/10.5530/ijper.58.4.137)
11. H. C. Upadhyay, *Lett. Drug Des. Discov.* **20** (2023) 373 (https://doi.org/10.2174/1570180820042301131444404)
12. H. C. Upadhyay, R. K. Verma, S. K. Srivastava, *J. Chromatogr. Sci.* **51** (2013) 21 (https://doi.org/10.1093/chromsci/bms099)
13. K. Chakraborty, A. Shivakumar, S. Ramachandran, *Int. J. Herb. Med.* **4** (2016) 61 (https://doi.org/10.22271/flora.2016.v4.i3.05)
14. K. N. Mishra, D. Mohapatra, P. Chaubey, A. N. Sahu, S. Kumar, H. C. Upadhyay, *Chem. Select* **8** (2023) e202301113 (https://doi.org/10.1002/slct.202301113)
15. H. M. Ahmed, S. Nabavi, S. Behzad, *Mini-Rev. Med. Chem.* **21** (2020) 302 (https://doi.org/10.2174/1389557520666200916143240)
16. A. Naganthran, G. Verasoundarapandian, F. E. Khalid, M. J. Masarudin, A. Zulkharnain, N. M. Nawawi, M. Karim, C. A. C. Abdullah, S. A. Ahmad, *Materials* **15** (2022) 427 (https://doi.org/10.3390/ma15020427)
17. W. C. Lu, D. W. Huang, C. C. R. Wang, C. H. Yeh, J. C. Tsai, Y. T. Huang, P. H. Li, *J. Food Drug Anal.* **26** (2018) 82 (https://doi.org/10.1016/j.jfda.2016.12.018)
18. A. F. Burlec, A. Corciova, M. Boev, D. Batir-Marin, C. Mircea, O. Cioanca, G. Danila, M. Danila, A. F. Bucur, M. Hancianu, *Pharmaceuticals* **16** (2023) 1410 (https://doi.org/10.3390/ph16101410)
19. Z. Mehboob, S. Sharif, M. S. Lodhi, A. B. Shah, M. Romman, Nayila, *Front. Pharmacol.* **15** (2024) e1389024 (https://doi.org/10.3389/fphar.2024.1389024)
20. G. C. S. Reddy, K. N. N. Ayengar, S. Rangaswami, *Phytochemistry* **14** (1975) 1195 (https://doi.org/10.1016/0031-9422(75)85072-2)
21. A. S. Ray, H. R. Chowdhury, *Res. J. Pharmacog. Phytochem.* **10** (2018) 120 (https://doi.org/10.5958/0975-4385.2018.00018.3)
22. C. P. Khare, *Indian Medicinal Plants: An Illustrated Dictionary*, Springer, New York, 2007, p. 717 (ISBN: 978-0-387-70637-5)
23. Y. M. Reddy, S. P. J. Kumar, K. V. Saritha, P. Gopal, T. M. Reddy, J. Simal-Gandara, *Plants (Basel)* **10** (2021) 545 (https://doi.org/10.3390/plants10030545)
24. N. Savithramma, P. Yugandhar, R. Hari Babu, K. Siva Prasad, *J. Pharm. Sci. Res.* **6** (2014) 382 (ISSN: 0975-1459)
25. U. Quattrocchi, *CRC World Dictionary of Medicinal and Poisonous Plants*, CRC Press, Boca Raton, FL, 2016, p. 3960 (https://doi.org/10.1201/b16504)
26. R. Gupta, M. G. Vairale, R. R. Deshmukh, P. R. Chaudhary, S. R. Wate, *Ind. J. Trad. Know.* **9** (2010) 713 (ISSN: 0975-1068)
27. K. Kotresha, M. Siddeshwari, *PENSEE* **51** (2021) 1136 (ISSN: 0031-4773)
28. M. Arif, Md. R. Kuddus, Md. T. Islam, M. Ibrahim, *GSC Biol. Pharmaceut. Sci.* **7** (2019) 85 (https://doi.org/10.30574/gscbps.2019.7.3.0097)
29. K. Vindhya, S. Leelavathi, *Int. J. Pharm. Sci. Res.* **5** (2014) 4975 (http://dx.doi.org/10.13040/IJPSR.0975-8232.5(11).4975-78)
30. H. C. Upadhyay, R. K. Verma, S. K. Srivastava, *Chrom. Res. Intern.* **2012** (2012) 62302 (https://doi.org/10.1155/2012/162302)
31. S. Dubale, D. Kebebe, A. Zeynudin, N. Abdissa, S. Suleman, *J. Exp. Pharmacol.* **15** (2023) 51 (https://doi.org/10.2147/JEP.S379805)
32. P. Wayne, *Clinical and Laboratory Standards Institute* **41** (2019) 3 (ISSN: 2162-2914)

33. Clinical and Laboratory Standards Institute, *M100. CLSI Supplement* **41** (2021) 3 (ISSN: 2162-2914)
34. F. R. Stermitz, P. Lorenz, J. N. Tawara, L. A. Zenewicz, K. Lewis, *Proc. Natl. Acad. Sci. U S A* **97** (2000) 1433 (https://doi.org/10.1073/pnas.030540597)
35. K. Vindhya, K. K. Sampath Kumar, H. S. Neelambika, S. Leelavathi, *Res. J. Pharm. Biol. Chem. Sci.* **5** (2014) 527 (https://www.rjpbcs.com/pdf/2014_5(2)/[57].pdf)
36. S. M. Mohamed, S. A. Ross, M. A. M. Ahmed, *Revista. Bras. Farmacog.* **32** (2022) 1038 (https://doi.org/10.1007/s43450-022-00335-w)
37. S. Iravani, *Green Chem.* **13** (2011) 2638 (https://doi.org/10.1039/c1gc15386b)
38. E. O. Mikhailova, *J. Funct. Biomater.* **11** (2020) 84 (https://doi.org/10.3390/jfb11040084)
39. N. Ahmad, S. Sharma, M. K. Alam, V. N. Singh, S. F. Shamsi, B. R. Mehta, A. Fatma, *Colloids Surf., B* **81** (2010) 81 (https://doi.org/10.1016/j.colsurfb.2010.06.029)
40. L. Elumalai, G. K. Anbazhagan, S. Palaniyandi, S. Nagarajan, S. Murthy, S. Anbalmani, N. Mohanam, A. P. Munusamy, B. Ramasamy, *J. Sol–Gel Sci. Technol.* **111** (2024) 293 (https://doi.org/10.1007/s10971-024-06441-6)
41. H. M. M. Ibrahim, *J. Radiat. Res. Appl. Sci.* **8** (2015) 265 (https://doi.org/10.1016/j.jrras.2015.01.007)
42. H. J. Butler, L. Ashton, B. Bird, G. Cinque, K. Curtis, J. Dorney, K. Esmonde-White, N. J. Fullwood, B. Gardner, P. L. Martin-Hirsch, M. J. Walsh, M. R. McAinsh, N. Stone, F. L. Martin, *Nat. Protoc.* **11** (2016) 664 (https://doi.org/10.1038/nprot.2016.036)
43. A. M. Ondieki, Z. Birech, K. A. Kaduki, P. W. Mwangi, N. M. Mwenze, M. Juma, C. Jeptoo, M. S. Dlamini, M. Maaza, *Spectrochim. Acta A Mol. Biomol. Spectrosc.* **296** (2023) 122694 (https://doi.org/10.1016/j.saa.2023.122694)
44. P. Mathur, S. Jha, S. Ramteke, N. K. Jain, *Artif. Cells Nanomed. Biotechnol.* **46** (2018) 57 (https://doi.org/10.1080/21691401.2017.1411932)
45. H. Zulfiqar, A. Zafar, M. N. Rasheed, Z. Ali, K. Mehmood, A. Mazher, M. Hasan, N. Mahmood, *Nanoscale Adv.* **1** (2019) 1707 (https://doi.org/10.1039/C8NA00343B)
46. O. V. Mikhailov, E. O. Mikhailova, *Materials* **12** (2019) 3177 (https://doi.org/10.3390/ma12193177)
47. A. R. Shahverdi, A. Fakhimi, H. R. Shahverdi, S. Minaian, *Nanomed. Nanotech. Biol. Med.* **3** (2007) 168 (https://doi.org/10.1016/j.nano.2007.02.001)
48. R. Ceylan, A. Demirbas, I. Ocsoy, A. Aktumsek, *Sustain. Chem. Pharm.* **21** (2021) 100426 (https://doi.org/10.1016/j.scp.2021.100426)
49. C. You, C. Han, X. Wang, Y. Zheng, Q. Li, X. Hu, H. Sun, *Mol. Biol. Rep.* **39** (2012) 9193 (https://doi.org/10.1007/s11033-012-1792-8)
50. S. Prabhu, E. K. Poulose, *Int. Nano Lett.* **2** (2012) 32 (https://doi.org/10.1186/2228-5326-2-32)
51. S. Anees Ahmad, S. Sachi Das, A. Khatoon, M. Tahir Ansari, M. Afzal, M. Saquib Hasnain, A. Kumar Nayak, *Mater. Sci. Energy Technol.* **3** (2020) 756 (https://doi.org/10.1016/j.mset.2020.09.002).

Journal of the Serbian Chemical Society
JSCS@tmf.bg.ac.rs • www.shd.org.rs/JSCS
J. Serb. Chem. Soc. 90 (6) S216–S221 (2025) *Supplementary material*

SUPPLEMENTARY MATERIAL TO

Green synthesis of silver nanoparticles utilizing *Gardenia latifolia* extract, characterization and *in vitro* antibacterial activity

SATYAM SRIVASTAVA[1], PRASHANSHA SRIVASTAVA[2], GAURAV RAJ DWIVEDI[2], VENKATNARAYAN RAMANATHAN[3] and HARISH CHANDRA UPADHYAY[1]*

[1]Laboratory of Chemistry, Department of Applied Sciences, Rajkiya Engineering College (Affiliated with Dr. A.P.J. Abdul Kalam Technical University, Lucknow), Churk, Sonbhadra-231206, India, [2]Department of Microbiology, ICMR - Regional Medical Research Centre, Gorakhpur-273013, India and [3]Department of Chemistry, Indian Institute of Technology (BHU), Varanasi-221005, India

J. Serb. Chem. Soc. 90 (6) (2025) 709–725

PHYTOCHEMICAL INVESTIGATIONS OF CRUDE EXTRACT AND FRACTIONS

Table S-I. Preliminary phytochemical investigation of the bark of Indian plant *G.latifolia*

Functional groups	Test	Impression
Alkaloids	Dragendrof's reagent: Extract + dilute Hydrochloric acid + Dragendroff's reagent (potassium bismuth iodide solution). Red ppt. obtained indicated the presence of alkaloids	-
Flavonoids	Lead acetate test: Extract + 2-3 drops of lead acetate solution. The yellow color ppt. obtained indicated the presence of flavonoids.	+
Anthraquinones	Bontrager's test: Boil the extract + dilute sulfuric acid+ filter + chloroform. The organic layer obtained + 2-3 drops of strong ammonia solution. The lower ammoniacal layer takes on a pink or red color indicating the presence of anthraquinones	+
Tannins	Gelatin test: Extract + 1% gelatin solution containing NaCl. White ppt. obtained shows the presence of Tannins.	+
Saponins	Extract + 20 mL water. The formation of stable foam indicates the presence of saponins.	+
Steroids	Libermann-Burchard test: Extract + 2 mL of chloroform + ten drops of acetic anhydride and two drops of concentrated sulfuric acid. If the solution turns red, then blue, and finally bluish-green, a steroidal nucleus is present. If the solution turns purple or red, a triterpenoid nucleus is present.	+
Glycosides/Sugars	0.5 mL of crude extract +1 mL of distilled water and NaOH. The yellow tint obtained indicates the presence of glycosides/reducing sugars.	+

* Corresponding author. E-mail: harishcu@recsonbhadra.ac.in

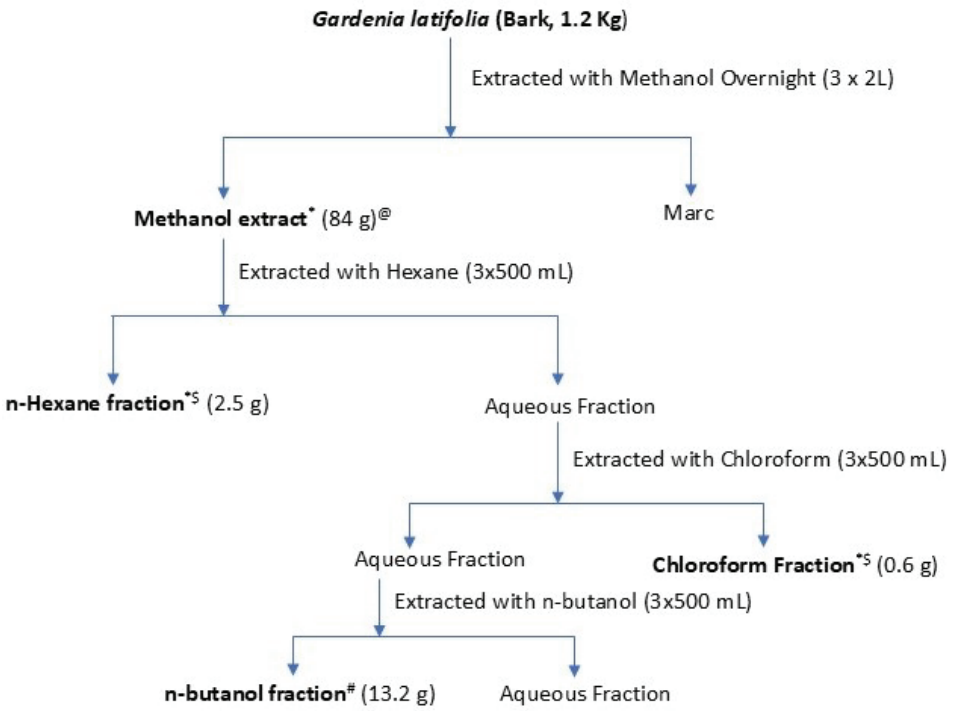

@A part (24g) was taken out.
$Washed with water and dried over Na_2SO_4
*Solvent was completely removed under vacuum at 60-70°C on Buchi Rota Vapor.
#Solvent removed under vacuum by making azeotrope with water.

Fig. S-1. Flow chart of fractionation procedure of crude extract

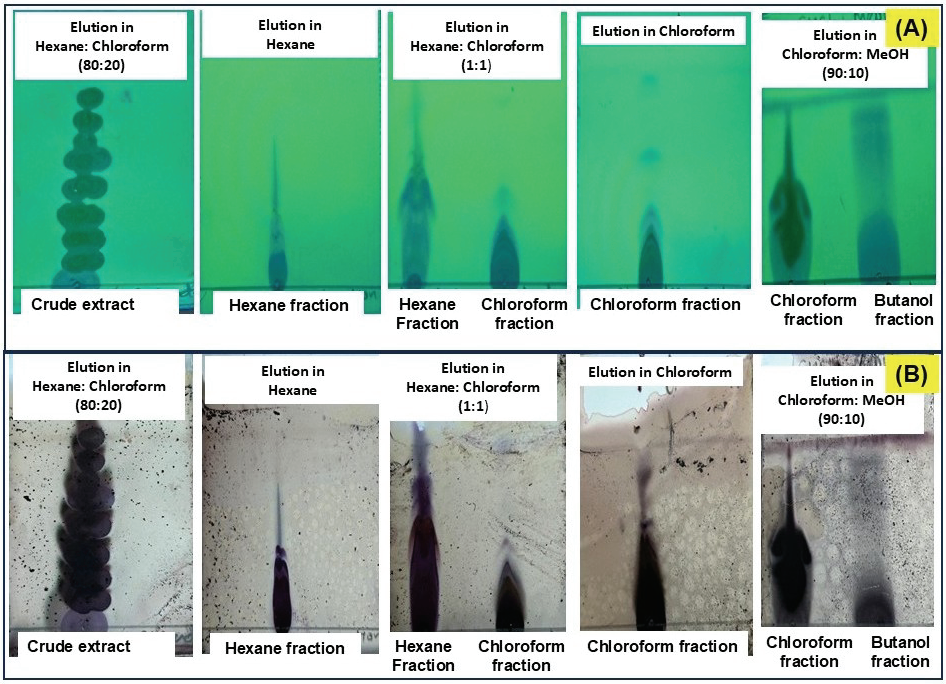

Fig. S-2. Thin layer chromatography profile of extract and fractions visualized under UV-254 nm (**A**), and on treated with a vanillin-sulphuric acid (1: 5, w/v) solution in ethanol, and subsequently heated at 95 °C for 5 minutes (**B**).

CHARACTERIZATION OF THE AGNPS FORMULATIONS

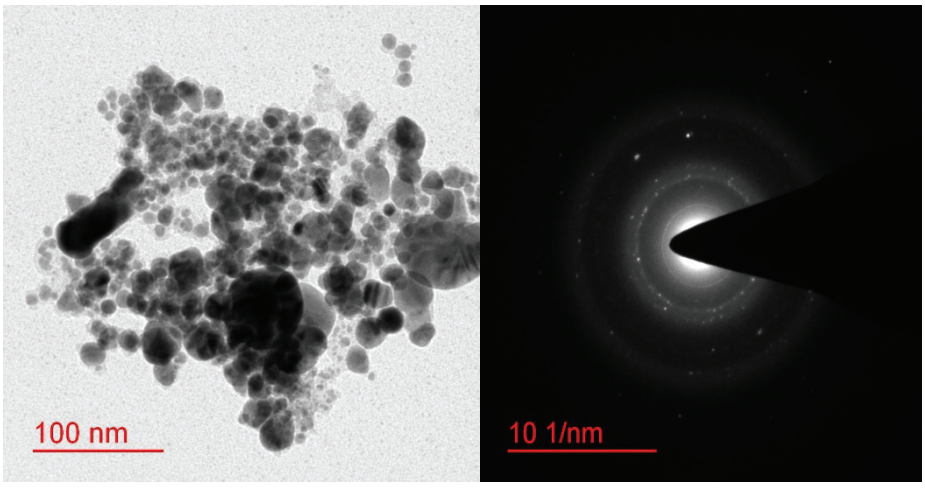

Fig. S-3. HR-TEM and SAED images of the AgNPs formulation **F2**

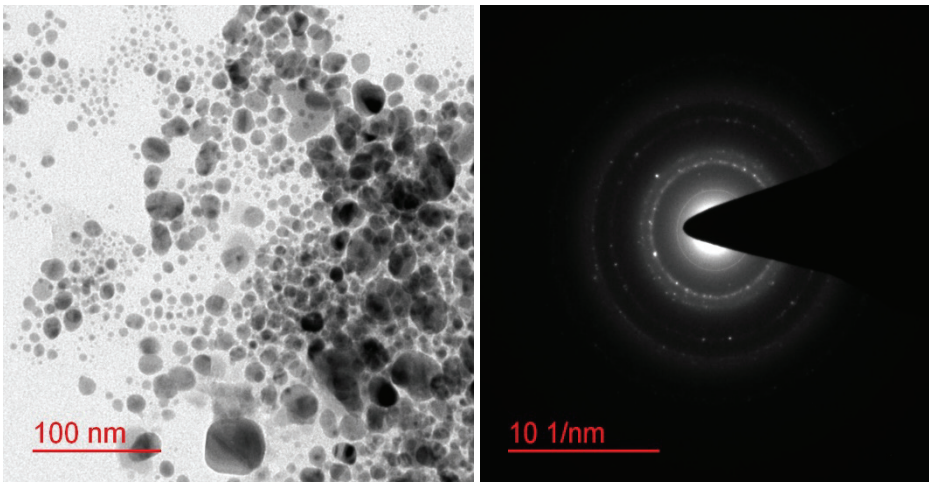

Fig. S-4. HR-TEM and SAED images of the AgNPs formulation **F4**

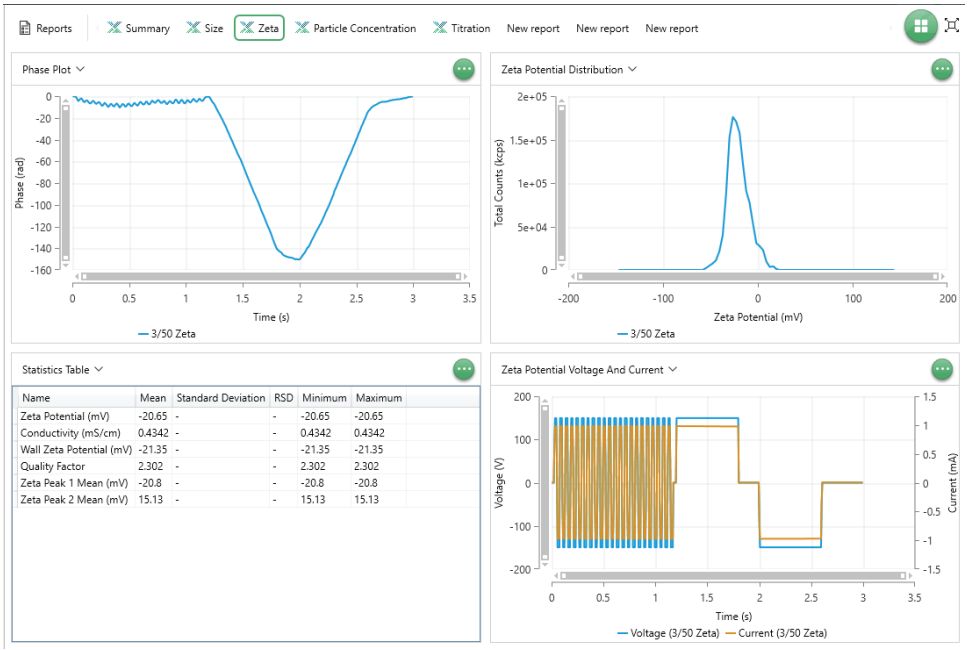

Fig. S-5. Zeta potential of the AgNPs formulation **F3**

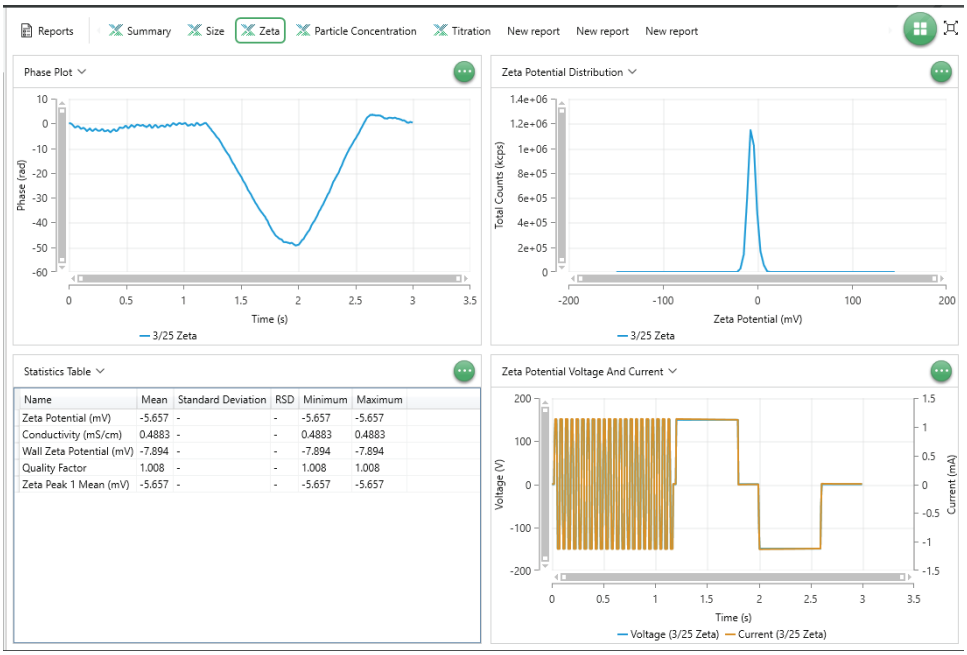

Fig. S-6. Zeta potential of the AgNPs formulation **F4**

Fig. S-7. Hydrodynamic particle size of the AgNPs formulation **F3**

Fig. S-8. The hydrodynamic particle size of the AgNPs formulation **F4**.

Journal of the Serbian Chemical Society
JSCS@tmf.bg.ac.rs • www.shd.org.rs/JSCS
J. Serb. Chem. Soc. *90* (6) 727–739 (2025)
JSCS–5416
Original scientific paper
Published 23 June, 2025

Conceptual DFT study based on the characterization of the local electrophilicity and nucleophilicity for intramolecular Diels–Alder reaction of the *trans* isomers of 4-[(4*E*)-4,6-heptadien-1-yl]-2-cyclohepten-1-one

IMANE TEMER, ASMAA MOSTEFAI* and ALI RAHMOUNI

Modelling and Calculation Methods Laboratory, University of Saida Dr Moulay Tahar, Saida, Algeria

((Received 8 August, revised 9 September 2024, accepted 29 March 2025)

Abstract: One of the most powerful methods for the rapid synthesis and formation of complex polycyclic molecules with biological interest involves the use of Diels–Alder (DA) reaction especially its intramolecular variant. The *trans* isomers of 4-substituted cycloheptenones were experimentally found to be excellent ethylenes, readily undergoing DA reactions. In this study we were interested to elucidate and predict the reactivity of the intramolecular DA (IMDA) reactions of the *trans*-A and *trans*-B isomers of 4-substituted cycloheptenone by means of the indexes of reactivity derived from DFT, at B3LYP/6-31G+(d,p) level of theory, using Gaussian09 program. In order to identify the reactional sites and to predict site selectivity of these compounds towards electrophilic and nucleophilic attack, the electrophilic P_k^+ and nucleophilic P_k^- Parr functions, the local electrophilicity ω_k and local nucleophilicity N_k were used in order to characterize the most electrophilic and nucleophilic sites. For the purpose, to make clear classification of the electrophilicity and nucleophilicity of the interacting diene and ethylene moieties within the same molecule, the local reactivity difference index R_k was used as a power full descriptor to study this IMDA cycloaddition. The fragments electrophilicity and nucleophilicity indices were calculated, according to the fragmentation model. The dual philicity index γ and the degree of transferability were determined. Here presented calculations showed, as expected, that the electronic transfer will take place from diene to ethylene moiety. The predictions thus made are in good agreement with other theoretical studies that analyse the electronic transfer through global electronic density transfer (GEDT).

Keywords: cycloalkenone; cycloaddition; fragmentation; IMDA; diene; ethylene.

* Corresponding author. E-mail: asmaa.mostefai@univ-saida.dz
https://doi.org/10.2298/JSC240808020T

INTRODUCTION

For a long time, chemists have sought to establish relationships uniting the structure and chemical reactivity of molecules. On the experimental level, the means of analysing molecular structures have become both numerous and more efficient. From a theoretical point of view, quantum chemistry methods represent increasingly useful and reliable tools in the study of the structure and reactivity of chemical compounds. The study of reactivity is based on two main aspects. The first one consists of the calculation of thermodynamic parameters and the second one is the prediction of the reaction mechanism which is done from a theoretical point of view: either by locating the transition state structure (TS), calculating the activation energies or highlighting the optimal reaction path, or by the use of reactivity indices and descriptors in order to determine the preferential sites of interaction between reagents.

The work presented in this paper is part of this latter approach, *i.e.*, the prediction of reaction sites using reactivity indices and descriptors. Indeed, predicting the reactivity and selectivity of a chemical process is crucial. Our interest was particularly focused on the theoretical study of the reactivity of two isomers of 4-[(4*E*)-4,6-heptadien-1-yl]-2-cyclohepten-1-one. These compounds were experimentally found to be excellent ethylenes, readily undergoing Diels–Alder (DA) reaction to form the corresponding *trans*-fused intramolecular DA (IMDA) reactions cycloadduct in very high yields. The DA reaction is undoubtedly one of the most powerful and widely used approaches synthetic organic chemistry.[1] This reaction, which proceeds *via* a one-step mechanism, consist on a cycloaddition between a conjugated diene and a substituted ethylene, resulting in the formation of unsaturated six-membered rings. It is regioselective, stereoselective, atom economic and highly efficient, making it a valuable tool for synthesizing cyclic structures, particularly in the construction of complex molecules and natural products.[2] Depending on the nature of the diene and ethylene, many different types of six carboxylic structures can be composed,[3] this makes it important in the pharmaceutical and biological field in particular even in modern industry.[4] For instance, the synthesis of products with biological activities such as: vitamin E which deals with the inhibition of plant growth,[5] cytotoxicity and growth promotion activity of neuritis[6] and mogolide A which is used to selectively modify biochemical structures.[7]

Due to its usefulness and efficiency in carbon-carbon bond formation, DA reactions have sparked the interest of experimental and theoretical chemists and continues to be an important subject for both computational[8] and experimental studies.[9]

The IMDA reaction is a variant of the DA reaction in which the diene and the ethylene are linked in a same molecule,[10] but it does not change its reactivity, which can only be modified by the strain associated to the intramolecular pro-

cess. Due to its flexibility and its notable stereoselectivity in the construction of fused cycles in only one synthetic step, IMDA reaction has been utilized to construct many pharmacological and biological and also as a pathway in the total synthesis of natural products.[11]

DA reaction of cycloalkenones is considered to be a simple method of backbone construction which has made it possible to obtain fused or bridged tricyclic products.[12] Stereoisomerism is controlled by the *endo*/*exo* approach and depends on the length of the chain that separates the diene from the ethylene as well as the *cis*/*trans* configuration of the latter. In a general way, the product in *endo* mode is majority or exclusive in the case of 2-cycloalkenones.[13] These results have been explained by steric effects and electronic effects.[14]

Dorr and Rawal described a powerful method using UV radiation to generate, in good yield, tricyclic compounds from relatively simple precursors. These are the first examples of IMDA reactions of 2-cycloalkenones.[15] This reaction occurs in two steps, the first being a photochemical isomerization of *cis*-cycloheptenone to *trans*-cycloheptenone. The IMDA thermal reaction at room temperature then takes place on the *trans* isomers. It is very interesting to recall and confirm that *trans*-enones are excellent ethylenes.[16] It was concluded that isomerization of the ethylene of *cis* 2-cycloheptenone yields two diastereoisomers *trans*-A and *trans*-B.

Interpreting and predicting the preferred direction of a reaction and product formation is one of the most important issues related to the problem of molecule reactivity.[17] The main purpose of this theoretical study is to predict the reactivity of cycloheptenone diastoisomers *trans*-A and *trans*-B and the selectivity of the IMDA reaction by means of the conceptual density functional theory (CDFT).[18] In the first time, the global electrophilicity and nucleophilic indices, the electrophilic and nucleophilic Parr functions and the single reactivity difference indices have been successfully used to the study of the IMDA title reaction. Indeed, on 2009 Domingo *et al.* proposed the polar DA (P-DA) mechanism,[19] which is followed by many and various of the experimental DA reactions, in which the nucleophilic and electrophilic interactions taking place at the TSs are responsible for the feasibility of the reaction. In this sense, the use of the electrophilicity and nucleophilicity indices and the Parr functions have become powerful tools to study DA reactions.

In 2012 Chattaraj *et al*. introduced a single reactivity difference index *Rx* allowing to characterize the electrophilic/nucleophilic centre of a molecule, permitting the study of polar intramolecular processes.[20] In 2013, the electrophilic and nucleophilic Parr functions were proposed to study the local reactivity in polar reactions within the CDFT.[21] In 2016, Domingo proposed a new theory of reactivity in organic chemistry baptized molecular electron density theory (MEDT), which rejects all theories, models and interpretations based on molec-

ular orbital analyses, in which the changes in electron density along a chemical reaction are responsible for the chemical reactivity of organic molecules.[22]

The partitioning of global electronic properties into fragments groups within a same molecule serves as a powerful technique when discussing the nucleophilicity and electrophilicity of diene and ethylene fragments in IMDA processes.[23,24] To this end, an appropriate fragmentation model, in which *trans*-A and *trans*-B isomers were arbitrarily partitioned into diene fragment (D), ethylene fragment (Dp) and the corresponding chain of union (Ch) as illustrated in Fig. 1, were used, in the second time, to calculate the fragment electrophilicity and nucleophilicity indices and in order to characterize the nucleophilicity and electrophilicity of the interacting fragments.

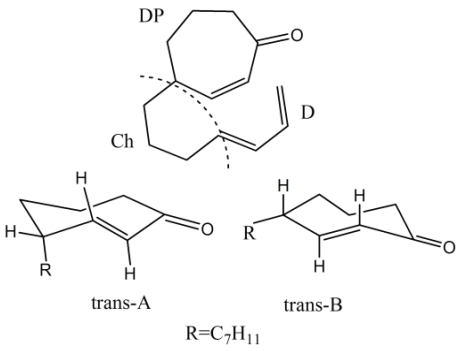

Fig. 1. Fragmentation scheme for IMDA and the *trans* isomers of 2-cycloheptenone.

The structure of this paper is as follows: after this brief introduction, the next section deals the computational details. The section which follows contains the main results and general discussion concerning the prediction of the global and local electrophilicity and nucleophilicity reactivity the title compounds. Also, we discussed the results concerning the fragment electrophilicity and nucleophilicity indices for IMDA reaction of *trans*-A and *trans*-B isomers of 4-substituted cycloheptenone. Finally, the paper is ended by recalling the main conclusions.

CALCULATION DETAILS

The Gaussian 09 package has been used to perform all calculations presented in this work.[25] To obtain fully optimized geometries for the *trans* isomers of 2-cycloheptenone derivatives, we undertook calculations at B3LYP/6-31G+(d,p) level of theory. All optimized structures were identified as minima on the potential energy surface, with no imaginary frequencies appeared in their frequency calculations results, at the same level of theory. To predict the site selectivity of the molecules under study towards electrophilic and nucleophilic attack and to elucidate their nucleophilicity and electrophilicity, various reactivity and selectivity descriptors and the appropriate local quantities have been calculated. The global and local reactivity descriptors used in the present work are described below.[26]

The global hardness η (Eq. (1)), based the energies of the frontier molecular orbital E_{HOMO} and $E_{LUMO,}$ are defined as follows:[27]

$$\eta = E_{LUMO} - E_{HOMO} \quad (1)$$

The chemical potential μ (Eq. (2)) can be expressed using the energies of the frontier molecular orbital, as:[28]

$$\mu = (E_{LUMO} + E_{HOMO})/2 \quad (2)$$

The global electrophilic index[29] ω was calculated using the following expression (Eq. (3)):

$$\omega = \mu^2/2\eta \quad (3)$$

By the Kohn–Sham method, the empirical (relative) nucleophilic index N is defined as follows (Eq. (4)):[30]

$$N = E_{HOMO(NU)} - E_{HOMO(TCE)} \quad (4)$$

Where $E_{HOMO(NU)}$ corresponds to the HOMO energy of the nucleophile and $E_{HOMO(TCE)}$ is the HOMO energy of the tetracyanoethylene (TCE) taken as reference.

The Parr function $P(r)$ are expressed by the following equations:[21]

$$P^-(r)=\rho_s^{rc}(r) \text{ for electrophilic attacks} \quad (5)$$

$$P^+(r) = \rho_s^{ra}(r) \text{ for nucleophilic attacks} \quad (6)$$

where $\rho_s^{rc}(r)$ is the Mulliken atomic spin density (*ASD*) at the r atom of the radical cation of a considered molecule $\rho_s^{ra}(r)$ is the *ASD* at the *r* atom of the radical anion. Each *ASD* condensed at the different atoms of the radical cation and radical anion of molecule provides the local nucleophilic P_k^- and local electrophilic P_k^+ Parr functions of the natural system.

Accordingly, the local electrophilicity ω_k (Eq. (7)) and the local nucleophilicity N_k (Eq. (8)) indices are defined as follows:

$$\omega_k = \omega P_k^+ \quad (7)$$

$$N_k = N P_k^- \quad (8)$$

The local reactivity difference index R_k is given by the following three conditions to identity the centers with electrophilic (R_k = +n.nn) or nucleophilic (R_k = −n.nn) behaviour as well as the ambiphilic (R_k = ±n.nn) behavior in addition to eliminate the centers with marginal reactivity:[31]

$$\text{if } (1<\omega_k/N_k<2) \text{ or } (1<N_k/\omega_k<2)$$

$$\text{then } R_k = (\omega_k+N_k)/2 \text{ ambiphilic } (R_k = \text{n.nm}) \quad (9)$$

$$\text{else } R_k = (\omega_k - N_k) \quad (10)$$

$$\text{where } R_k>0 \text{ electrophilic } (R_k = +\text{n.nm})$$

$$\text{and } R_k<0 \text{ nucleophilic } (R_k = -\text{n.nm})$$

$$\text{If } |R_k|<0.1 \text{ thene } R_k = 0$$

The local hardness (k) on an atom was expressed by Meneses and al, in terms of the Fukui indices for both nucleophilic and electrophilic attacks, as well as the energies of HOMO and LUMO.[32] This approach allowed for the determination of group hardness associated with each fragment (Eq. (10)), namely Ω = D, Dp and Ch, within the compound 2-cycloheptenone, which can be arbitrarily divided into diene (D), ethylene (Dp) and the union chain (Ch) fragments, as illustrated in Fig. 1:

$$\eta_\Omega = \Sigma n_k \text{ or } n_k = E_{LUMO} f_k^+ - E_{HOMO} f_k^- \quad (11)$$

Using Koopman's theorem, the electronic chemical potential of the D and Dp fragments can be presented in the following form:[32]

$$\mu_\Omega = \Sigma(E_{\mathrm{HOMO}} / 2f_k^-) + \Sigma(E_{\mathrm{LUMO}} / 2f_k^+) \quad (12)$$

The local electrophilic index of each fragment (Eq. 12) [32]:

$$\omega_D = \omega\Sigma_{k\in D} f_k^+ \text{ and } \omega_{Dp} = \omega\Sigma_{k\in Dp} f_k^+ \quad (13)$$

The local nucleophilic index of each fragment can be calculated by the following equation:[32]

$$N_D = N\Sigma_{k\in D} f_k^- \text{ and } N_{Dp} = N\Sigma_{k\in Dp} f_k^- \quad (14)$$

The dual philicity indexes γ is:[32]

$$\gamma_1 = \omega_{Dp} + N_D \text{ and } \gamma_2 = \omega_D + N_{Dp} \quad (15)$$

RESULTS AND DISCUSSION

The main optimized geometric parameters of the *trans*-A and *trans*-B isomers of 4-[(4*E*)-4,6-heptadien-1-yl]-2-cyclohepten-1-one are given in Table I, following the labelling of the atoms reported in Fig 2. B3LYP/6-31+G (d,p) method predicts that the *trans*-A isomer is more stable than the *trans*-B isomer. The energy gap between them is of the order of 24.22 kJ/mol.

TABLE I. The energy and the geometry parameters of 4-substituted 2-cycloheptenone isomers

Enrgy, bond length, bon angle	*trans*-A	*trans*-B
E / u.a.	–620.70148	–620.69225
C_{14}–C_{33}	7.75 Å	5.91 Å
C_{16}–C_{27}	5.00 Å	3.37 Å
C_{12}–C_{14}–C_{16}–C_3	–113.51°	115.27°
C_{27}–C_{28}–C_{30}–C_{33}	–29.53°	–31.01°
C_3–C_{17}–C_{20}–C_{23}	–179.72°	–70.07°
H_{35}–C_{16}–C_3–H_7	–177.81°	–17.97°
H_{35}–C_{16}–C_3–C_{17}	55.27°	–141.52°

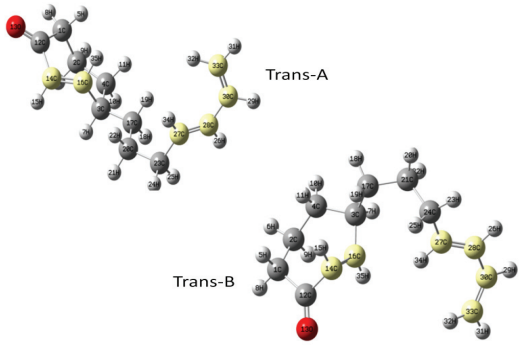

Fig. 2. Optimized geometries of 4-substituted 2-cycloheptenone isomers calculated at B3LYP/6-31+G(d,p) method.

Global reactivity

The global reactivity indices of 4-substituted 2-cycloheptenone isomers, which include the electronic chemical potential (μ), the chemical hardness (η), the global electrophilicity (ω), the global nucleophilicity (N) and the global softness (S), were calculated at B3LYP/6-31+G(d,p) level of theory and are reported in Table II.

TABLE II. Global electronic properties and reactivity indices of *trans*-A and *trans*-B isomers of 4-substituted 2-cycloheptenone calculated at B3LYP/6-31+G(d,p) level of theory

Isomer	E_{HOMO}	E_{LUMO}	η	μ	ω	N	S
	u.a.		eV	eV	eV	eV	eV
trans-A	–0.23	–0.06	4.62	–4.09	1.81	3.00	0.10
trans-B	–0.23	–0.04	4.99	–3.78	1.43	3.12	0.10

These results show that *trans*-B isomer is more nucleophilic than *trans*-A isomer. The global nucleophilicity calculated indices predict that the nucleophilic power decreases from *trans*-B (N = 3.12 eV) to *trans*-A (N = 3 eV). Moreover, *trans*-B isomer can be classified as a strong nucleophile, according to the nucleophilicity scale.[33] The nucleophilic character of these compounds is in agreement with the calculated electronic chemical potentials. Indeed, *trans*-B is characterized by the highest chemical potential (μ = –3.78 eV) followed by *trans*-A (μ = = –4.09 eV). Concerning the electophilic power, it decreases from *trans*-A (ω = = 1.81 eV) to *trans*-B (ω = 1.43). According to the electrophilicity scale,[33] *trans*--A isomer (ω > 1.50 eV) is a strong electrophile, that is able to participate easily in polar DA reactions.[19]

Local reactivity

In order is to predict the preferred electrophilic and nucleophilic sites within molecules under study, it will be necessary to focus attention on the calculated local electrophilicity and nucleophilicity reactivity indices. The corresponding values for both nucleophilic and electrophilic functions are presented in Table III.

TABLE III. electrophilic (P_k^+) and nucleophilic (P_k^-) Parr functions, local electrophilicity (ω_k) local nucleophilicity (N_k), and local reactivity difference (R_k) of *trans*-A and *trans*-B isomers

Isomer	Fragment	Site	P_k^+	P_k^-	ω_k	N_k	R_k
trans-A	Dp	C_{14}	0.02	0.26	0.03	0.79	–0.75
		C_{16}	0.86	0.04	1.56	0.13	+1.42
	D	C_{27}	–0.01	0.19	–0.01	0.58	–0.59
		C_{33}	0.00	0.29	0.00	0.87	–0.86
trans-B	Dp	C_{14}	0.22	0.30	0.32	0.96	–0.63
		C_{16}	0.57	–0.01	0.82	–0.03	+0.85
	D	C_{27}	0.08	0.17	0.12	0.55	–0.43
		C_{33}	0.13	0.35	0.19	1.09	–0.90

The local value of Parr function provides insight into the reactivity and selectivity of the specific site in the molecule. In most polar cycloaddition reactions, the regioisomeric channel most likely to form involves the interaction between the most nucleophilic centre of the nucleophile and the most electrophilic centre of electrophile. Therefore, analysis of the local electrophilicity ω_k and local nucleophilicity N_k derived from Parr functions P_k^+ and P_k^- can explain the experimentally observed regioselectivity.

In both *trans*-A and *trans*-B isomers, the electrophilic P_k^+ Parr function shows the C_{16} carbon to be the most electrophilic centre, whereas the nucleophilic P_k^- Parr function displays C_{33} atom as nucleophilic centre. The local electrophilicity ω_k predicts that C_{16} is the main electrophilic centre with 1.56 and 0.82 eV, in *trans*-A isomer and *trans*-B isomer, respectively. However, the local nucleophilicity N_k suggests that C_{33} is the main nucleophilic centre of *trans*-A and *trans*-B isomers with 0.87 and 1.09 eV, respectively. Accordingly, the IMDA reaction path of the *trans* isomers of 4-[(4*E*)-4,6-heptadien-1-yl]-2-cyclohepten--1-one that is more privileged in terms of regioisomers will be characterized by the first formation of the C_{16}–C_{33} single bound.

In order to simultaneously predict the electrophilicity and nucleophilicity sites of a given molecular system, R_k index has been calculated. The negative values of R_k correspond to nucleophilic centres. Whereas the positive values of R_k, correspond to electrophilic centres. The predicted values of R_k show, as expected, that C_{16} site with the high positive value acts as the most electrophilic centre, while the most nucleophilic centre is attributed to C_{33} site. One important point to note is that the strong local electrophilicity value is assigned to the β conjugated carbon C_{16} atom which is activated because of the withdrawing mesomeric effect of the adjacent carbonyl group, enhancing then its electrophilic character. Accordingly, the cycloaddition IMDA reaction of the *trans* isomers of 4-[(4*E*)-4,6-heptadien-1-yl]-2-cyclohepten-1-one may be regiospecific.

As shown in Fig. 3, illustrating the 3D representation of Mulliken atomic spin density (*ASD*) of the radical anions and radical cations, the electrophilic P_k^+ Parr functions of both *trans*-A and *trans*-B isomers which are mainly located at ethylene fragment, particularly at the reactives sites C_{16} and C_{14}. The highest P_k^+ value is assigned to C_{16} atom. Alternatively, the nucleophilic P_k^- Parr functions are principally centred at diene fragment, precisely, at the reactive sites C_{33} and C_{27}. *ASD* analysis allows to characterize the most nucleophilic and most electrophilic centres and to establish the chemoselectivity and regioselectivity in polar reactions.

Fragment electrophilicity and nucleophilicity indices

In this part, we were interested on the characterization of the group nucleophilicity and electrophilicity for intramolecular DA reactions of the com-

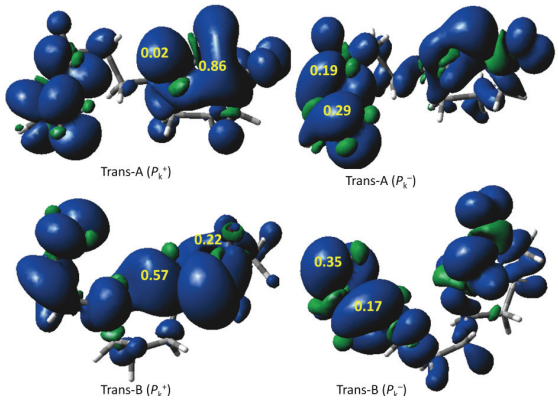

Fig. 3. 3D representation of *ASD* of the radical anion and the radical cation of *trans*-A and *trans*-B isomers of 4-[(4*E*)-4,6-heptadien-1-yl]-2-cyclohepten-1-one.

pounds under study. The fragment electrophilicity and nucleophilicity indices consisting of the global electrophilicity (ω) and nucleophilicity (N) within IMDA reagents associated with the fragmentation scheme given in Scheme 1 and the degree of transferability T_W, T_N of the diene (D), ethylene (Dp) and the chain (Ch) that connects them were calculated at B3LYP/6-31+G(d,p) and are represented in Table IV.

TABLE IV. Fragment electrophilicity and nucleophilicity indexes for IMDA reaction of *trans*-A and *trans*-B isomers of 4-substituted cycloheptenone

Parameter	*trans*-A	*trans*-B
ω_D / eV	0.42	0.37
N_D / eV	1.09	1.36
ω_{Dp} / eV	0.74	0.56
N_{Dp} / eV	0.78	0.61
ω_{ch} / eV	–0.02	–0.02
N_{ch} / eV	–0.07	–0.11
($T\omega_D = \omega_D/\omega$), %	23.4	26.4
($T\omega_{Dp} = \omega_{Dp}/\omega$), %	41.2	39.3
($TN_D = N_D/N$), %	36.4	43.5
($TN_{Dp} = N_{Dp}/N$), %	26.2	19.6

The electrophilic index of the ethylene Dp fragment for *trans*-A and *trans*-B isomers is higher than that of the diene D fragment. The nucleophilic index of diene fragments for both *trans*-A and *trans*-B isomers is much higher than that of ethylene fragments, the nucleophilicity values of D fragment are much higher when compared to electrophilic ones ($N_D/\omega_D > 1$). The contribution of the union chain to both nucleophilic and electrophilic is marginal compared to the D and Dp fragments. The degree of transferability of the fragment's electrophilicity is higher at ethylene fragment than at diene fragment ($T\omega_{Dp} > T\omega_D$). Thus, *trans*-A

and *trans*-B isomers present the electrophilicity pattern accumulated at the ethylene Dp fragment. On the other hand, the degree of transferability of the fragment's nucleophilicity show that TN_D is higher and TN_{Dp}, in both *trans*-A and *trans*-B isomers. This suggests that the nucleophilicity pattern involved in IMDA reaction is concentrated at the diene fragment. The compounds under study are expected to undergo IMDA processes of D to Dp electron flow (DDpF), with fragment D acting as the nucleophile and fragment Dp acting as an electrophile (*i.e.*, the normal electron demand process). Our predictions are in accordance with those reported by Jorge Soto-Delgado and his collaborators.[32]

The calculated dual philicity indexes γ reported in Table V, can be used to describe the direction of the electron flux in IMDA process. Specifically, if the charge transfer CT occurs from the diene to the ethylene fragments or inversely, from the ethylene to the diene fragments. It may be noted that ($\gamma_1 > \gamma_2$) in both *trans*-A and *trans*-B isomers. Consequently, in this IMDA reaction, the charge transfer took place rather from the diene fragment to the ethylene fragment. This finding is in agreement with other computational studies that characterize the charge transfer by examining the global electron density transfer GEDT.[34]

TABLE V. The dual philicity indexes γ_1 and γ_2 predicted values

Isomer	γ_1	γ_2	$\Delta\gamma_{12}$
trans-A	1.83	1.21	0.62
trans-B	1.92	0.99	0.93

The fragment's electrophilicity difference $\Delta\omega_\Omega$ indices provide the insight into the polar character of the IMDA reaction. The calculated values are displayed in Table VI. For *trans*-A and *trans*-B isomers, these values, that are not significative, are 0.27 and 0.28 eV, respectively.

TABLE VI. Electrophilic index of ω_D, ω_{Dp} and the invariance of electrophile ($\Delta\omega_\Omega$) of D and Dp fragments

Isomer	D			Dp			$\Delta\omega_\Omega = \lvert \omega_D - \omega_{Dp} \rvert$
	η / eV	μ / eV	ω / eV	η / eV	μ / eV	ω / eV	
trans-A	1.91	–1.37	0.49	0.97	–1.20	0.77	0.27
trans-B	2.31	–1.62	0.57	0.55	–0.97	0.86	0.28

CONCLUSION

In summary, in order to predict which atoms within molecules under investigation are most likely to suffer electrophilic and nucleophilic attacks, various global and local reactivity and selectivity descriptors have been shown to be very powerful to predict the most electrophilic and nucleophilic sites. These descriptors prove to be well adapted to study the reactivity of title molecules. It seems

useful to recall the main results that we obtained in this theoretical study and which can be summarized as follows:

The global nucleophilicity indices predict that the *trans*-B isomer can be classified as a strong nucleophile, according to the nucleophilicity scale. It is more nucleophilic than the *trans*-A isomer. The *trans*-A isomer (ω > 1.50 eV) is a strong electrophile, that is able to participate easily in polar DA reactions.

In order to predict the preferred electrophilic and nucleophilic sites within the molecules under study, it will be necessary to focus attention to the calculated local electrophilicity and nucleophilicity reactivity indices. In both trans-A and trans-B isomers, the electrophilic P_k^+ Parr function shows the β conjugated C_{16} carbon to be the most electrophilic centre, whereas the nucleophilic P_k^- Parr function displays C_{33} atom as nucleophilic centre.

The local electrophilicity ω_k and local nucleophilicity N_k gave the same trends of reactivity by favouring C_{16} and C_{33} as the most electrophilic and most nucleophilic sites, respectively. Accordingly, The IMDA reaction path of the *trans* isomers of 4-[(4*E*)-4,6-heptadien-1-yl]-2-cyclohepten-1-one that is more favoured as regioisomer will be characterized by the first formation of the C_{16}–C_{33} single bound.

With an aim to simultaneously predict the electrophilicity and nucleophilicity sites of the molecules under investigation, the local reactivity difference index R_k is shown to be very efficient in predicting nucleophilic and electrophilic centres at particular site through their sign. This index is also able to identify the stronger electrophilic and nucleophilic sites that are assigned, as expected, to C_{16} and C_{33}, respectively.

According to the fragmentation technique, describing the electrophilic and nucleophilic group, the diene fragment was shown to be a good nucleophile (electron donor) while the ethylene fragment behaves like an electrophile (electron acceptor) in this IMDA reaction. The dual descriptors γ_1 and γ_2 clearly show that the charge transfer occurred rather from the diene fragment, then from to the ethylene fragment.

Acknowledgments. The Algerian Ministry of Higher Education and Scientific Research (MESRS) and the Algerian Directorate General of Scientific Research and Technological Development (DGRSDT), are acknowledged and greatly thanked.

И З В О Д

КОНЦЕПТУАЛНА ТЕОРИЈА ФУНКЦИОНАЛА ГУСТИНЕ ЗАСНОВАНА НА КАРАКТЕРИЗАЦИЈИ ЛОКАЛНЕ ЕЛЕКТРОФИЛНОСТИ И НУКЛЕОФИЛНОСТИ ЗА ПРОУЧАВАЊЕ ИНТРАМОЛЕКУЛСКЕ ДИЛС–АЛДЕРОВЕ РЕАКЦИЈЕ *транс*-ИЗОМЕРА 4-[(4*E*)-4,6-ХЕПТАДИЕН-1-ИЛ]-2-ЦИКЛОХЕПТЕН-1-ОНА

IMANE TEMER, ASMAA MOSTEFAI и ALI RAHMOUNI

Modelling and Calculation Methods Laboratory, University of Saida Dr Moulay Tahar, Saida, Algeria

Једна од најзначајнијих метода за ефикасну синтезу и формирање сложених полицикличних молекула од биолошког значаја обухвата употребу Дилс–Алдерове (DA) реакције, нарочито њене интрамолекулске варијанте. Експериментално је утврђено да су транс изомери 4-супституисаних циклохептенона изванредни диенофили, који без проблема учествују у DA реакцијама. У овом раду је циљ био да се разјансни и предвиди реактивност интрамолекулских DA (IMDA) реакција *транс*-А и *транс*-Б изомера 4-супституисаних циклохептенона помоћу индекса реактивности изведених из теорије функционала густине (DFT), на B3LYP/6-31G+(d,p) нивоу теорије, користећи Gaussian09 програм. Како би се идентификовали реакционе центре и предвидели селективност ових једињења према електрофилном и нуклеофилном нападу, коришћене су електрофилне Парове функције (P_k^+) и нуклеофилне Парове функције (P_k^-), као и локална електрофилност (ω_k) и локална нуклеофилност (N_k). Ради јасније класификације електрофилности и нуклеофилности интерагујућих сегмената унутар молекула, локални индекс разлике реактивности (R_k) коришћен је као дескриптор за проучавање ове IMDA циклоадиције. Индекси електрофилности и нуклеофилности фрагмената израчунати су према моделу фрагментације. Дуални индекс филности (γ) и степен трансферабилности су такође одређени. Прорачуни су показали, како је и очекивано, да ће се електронски трансфер дешавати са диена ка диенофилном сегменту. Приказана предвиђања су у складу са другим теоријским студијама које анализирају електронски трансфер путем глобалног преноса електронске густине.

(Примљено 8. августа, ревидирано 9. септембра 2024, прихваћено 29. марта 2025)

REFERENCES

1. W. Carruthers, *Cycloaddition reactions in organic synthesis*, Elsevier, Amsterdam, 2013
2. R. B. Woodward, F. Sondheimer, D. Taub, K. Heusler, W. M. McLamore, *J. Am. Chem. Soc*. **74** (1952) 4223 (http://dx.doi.org/10.1021/ja01137a001)
3. C. P. Dell, *J. Chem. Soc. Perkin I* **22** (1998) 3873 (https://doi.org/10.1039/A803583K)
4. F. Fringuelli, A. Taticchi, E. Wenkert, *Org. Prep. Proc. Int.* **22** (1990) 131 (https://doi.org/10.1080/00304949009458194)
5. X. B. Xue, T. M. Lv, J. Y. Hou, D. Q. Li, X. X. Huang, S. J. Song, G. D. Yao, *Phytomedicine* **108** (2023) 154499 (https://doi.org/10.1016/j.phymed.2022.154499)
6. C. H. Mao, Q. M. Wang, R. Q. Huang, F. C. Bi, L. Chen, Y. X. Liu, J. Shang, *J. Agric. Food Chem.* **52** (2004) 6737 (https://doi.org/10.1021/jf048834e)
7. D. Caprioglio, S. Salamone, F. Pollastro, A. Minassi, *Plants* **10** (2021) 677 (https://doi.org/10.3390/plants10040677)
8. O. Acevedo, J. D. Evanseck*, Org. Lett*. **5** (2003) 649 (https://doi.org/10.1021/ol027408g)
9. E. J. Corey, *Angew. Chem. Int. Ed*. **41** (2002) 1650 (https://doi.org/10.1002/1521-3773(20020517)41:10%3C1650::AID-ANIE1650%3E3.0.CO;2-B)

10. S. Jin, P. Wessig, J. Liebscher, *J. Org. Chem.* **66** (2001) 3984 (https://doi.org/10.1021/jo0100897)
11. M. Juhl, D. Tanner, *Chem. Soc. Rev*. **38** (2009) 2983 (https://doi.org/10.1039/B816703F)
12. E. Ciganek, *Org. React.* **72** (2004) 1 (https://doi.org/10.1002/0471264180.or072.01)
13. H. V. Pham, R. S. Paton, A. G. Ross, S. J. Danishefsky, K. N. Houk, *J. Am. Chem. Soc.* **136** (2014) 2397 (https://doi.org/10.1021/ja410220w)
14. F. Fringuelli, M. Guo, L. Minuti, F. Pizzo, A. Taticchi, E. Wenkert, *J. Org. Chem.* **54** (1989) 710 (https://doi.org/10.1021/jo00264a039)
15. H. Dorr, V. H. Rawal, *J. Am. Chem. Soc* **121** (1999) 10229 (https://doi.org/10.1021/ja992287+)
16. T. J. Brocksom, J. Nakamura, M. L. Ferreira, U. Brocksom, *J. Braz. Chem. Soc.* **12** (2001) 597 (https://doi.org/10.1590/S0103-50532001000500004)
17. K. Yamamoto, I. Kawasaki, T. Kaneko, *Tetrahedron Lett.* **11** (1970) 4859 (https://doi.org/10.1016/S0040-4039(00)99728-4)
18. R. G. Parr, W. Yang, *Ann. Rev. Phys. Chem.* **46** (1995) 701 (https://doi.org/10.1146/annurev.pc.46.100195.003413)
19. L. R. Domingo, J. A. Sáez, *Org. Biomol. Chem.* **7** (2009) 3576 (https://doi.org/10.1039/B909611F)
20. P. K. Chattaraj, S. Duley, L. R. Domingo, *Org. Biomol. Chem*. **10** (2012) 2855 (https://doi.org/10.1039/C2OB06943A)
21. L. R. Domingo, P. Pérez, J. A. Sáez, *RSC Adv.* **3** (2013) 1486 (https://doi.org/10.1039/C2RA22886F)
22. L. R. Domingo, *Molecules* **21** (2016) 1319 (https://doi.org/10.3390/molecules21101319)
23. A. Benallou, H. E. A. El Abdallaoui, H. Garmes, *Heliyon* **4** (2018) e00504 (https://doi.org/10.1016/j.heliyon.2018.e00504)
24. A. Benallou, H. Garmes, N. Knouzi, H. E. A. El Abdallaoui*, Mor. J. Chem*. **2** (2014) 110 (https://doi.org/10.48317/IMIST.PRSM/morjchem-v2i2.1912)
25. *Gaussian 09*, Gaussian, Inc., Wallingford, CT, 2009
26. L. R. Domingo, M. Ríos-Gutiérrez, P. Pérez, *Molecules* **25** (2020) 2535. (https://doi.org/10.3390/molecules25112535)
27. W. Kohn, A. D. Becke, R. G. Parr, *J Phys. Chem.* **100** (1996) 12974 (https://doi.org/10.1021/jp960669l)
28. L. Meneses, W. Tiznado, R. Contreras, P. Fuentealba, *Chem. Phys. Lett.* **383** (2004) 181 (https://doi.org/10.1016/j.cplett.2003.11.019)
29. R. G. Parr, L. V. Szentpály, S. Liu, *J. Am. Chem. Soc.* **121** (1999) 1922 (https://doi.org/10.1021/ja983494x)
30. L. R. Domingo, P. Pérez, *Org. Biomol. Chem*. **9** (2011) 7168 (https://doi.org/10.1039/C1OB05856H)
31. P. K. Chattaraj, S. Duley, L. R. Domingo, *Org. Biomol. Chem*. **10** (2012) 2855 (https://doi.org/10.1039/C2OB06943A)
32. J. Soto-Delgado, L. R. Domingo, R. Contreras, *Org. Biomol. Chem.* **8** (2010) 3678 (https://doi.org/10.1039/C004628K)
33. L. R. Domingo, M. J. Aurell, P. Pérez, R. Contreras, *Tetrahedron* **58** (2002) 4417 (https://doi.org/10.1016/S0040-4020(02)00410-6)
34. L. R. Domingo, *RSC Adv*. **4** (2014) 32415 (https://doi.org/10.1039/C4RA04280H).

Journal of the Serbian Chemical Society
JSCS@tmf.bg.ac.rs • www.shd.org.rs/JSCS
J. Serb. Chem. Soc. *90* (6) 741–752 (2025)
JSCS–5417
Original scientific paper
Published 23 June, 2025

Quantum-chemical study of C–H···O interactions between $HTcO_4$ and aromatic amino acids

MILJAN BIGOVIĆ[1], IVANA S. VELJKOVIĆ[2], JELENA PETROVIĆ[3] and DUŠAN Ž. VELJKOVIĆ[4]*

[1]Faculty of Natural Sciences and Mathematics, University of Montenegro, Podgorica, Montenegro, [2]University of Belgrade – Institute for Chemistry, Technology and Metallurgy – National Institute of the Republic of Serbia, Belgrade, Serbia, [3]Center for Nuclear Medicine with PET, University Clinical Center of Serbia, Belgrade, Serbia; Faculty of Medicine, University of Belgrade, Belgrade, Serbia and [4]University of Belgrade – Faculty of Chemistry, Belgrade, Serbia

(Received 25 January, revised 4 February, accepted 7 February 2025)

Abstract: This study investigates C–H···O interactions between $HTcO_4$ and aromatic amino acids (phenylalanine, tyrosine and tryptophan) through quantum-chemical calculations. The interaction energies calculations were combined with the analysis of molecular electrostatic potentials (*MEP*) to understand the nature of these interactions. The strongest interaction was observed for the $HTcO_4$–tryptophan with an energy minimum of –9.53 kJ/mol at a distance of 2.1 Å. Phenylalanine showed a similarly strong interaction, with a minimum of –9.49 kJ/mol, while tyrosine exhibited the weakest interaction, with a minimum of –8.61 kJ/mol. Electrostatic potential maps confirmed the electrostatic nature of the C–H···O interactions, highlighting the role of the oxygen atoms in acting as hydrogen bond acceptors. These findings suggest that the position of the hydrogen atoms relative to the substituents on the aromatic ring influences the strength of the interactions. The results presented here could be of great importance for the recognition of new, overlooked noncovalent contacts between pertechnetic acid and amino acid fragments and a better understanding of the stability of pertechnetate-peptide complexes.

Keywords: hydrogen bond; pertechnetic acid; *ab initio* calculations.

INTRODUCTION

Technetium, particularly its radionuclide isotope technetium-99m (Tc-99m), is widely used in medicine primarily for diagnostic purposes in nuclear imaging.[1] One of the most common applications of Tc-99m and its compounds like pertechnetate anion (TcO_4^-) is in detecting and characterizing tumors through imag-

* Corresponding author. E-mail: vdusan@chem.bg.ac.rs
https://doi.org/10.2298/JSC250125013B

ing techniques such as single photon emission computed tomography.[2,3] Due to its advantageous characteristics, including a short half-life, a low radiation dose to patients, and the capability to be integrated into various compounds that target specific organs or tissues, Tc-99m serves as an excellent agent for diagnostic imaging. It provides crucial information about organ function and facilitates the early detection of diseases such as cancer, heart conditions, and bone disorders. Also, its rapid excretion from the body helps to minimize potential toxic effects. In addition to its diagnostic capabilities, Tc-99m plays a role in therapeutic applications, particularly in targeted radiotherapy. The ability to label peptides and other biomolecules with Tc-99m enhances their utility in targeting malignant tissues, thereby improving the efficacy of treatment while minimizing damage to surrounding healthy tissues.[4] Beyond its radiopharmaceutical applications, TcO_4^- exhibits intriguing noncovalent interactions in metal complexes and biological systems. As a ligand, TcO_4^- forms different noncovalent interactions in metal complexes, including Tc···O and Tc–O···H–O hydrogen bonds.[5] These contacts are essential for the formation of 1D and 2D supramolecular assemblies, highlighting the multifaceted role of TcO_4^- in both medical and structural chemistry. Quantum chemical calculations at the PBE0-D4/def2-TZVP level determined that the interaction energies for dimers involving Tc···O contacts range from –6.57 to –10.13 kJ/mol, indicating relatively modest interaction strengths.

On the other hand, noncovalent interactions of Tc-99m and its compounds within biological systems, particularly with biomolecules, remain less explored and mainly focused on Tc-binding in labeled peptides.[6–9] Understanding these interactions is crucial for elucidating potential reaction pathways and binding mechanisms. Among these, the study of C–H···O hydrogen bonding offers valuable insight, especially in systems involving aromatic amino acids. This type of interaction, often overlooked compared to stronger hydrogen bonds, plays a significant role in stabilizing molecular assemblies and influencing biological processes. Previous analysis of protein crystal structures showed that approximately 25 % of all noncovalent interactions in proteins are C–H···O interactions.[10]

C–H···O interactions involving aromatic C–H donors have been investigated in various systems.[11–13] Findings from crystal data analysis indicate that aromatic C–H···O interactions do not strongly favor linear geometries. MP2/cc-pVTZ calculations report stabilization energies for linear interactions of benzene with water, methanol and acetone as –5.36, –6.15 and –6.07 kJ/mol, respectively.[11] The study of C–H···O interactions between nucleic bases and water reveals that bifurcated interactions are significantly stronger than linear contacts.[13] This study found that the strongest linear interaction occurs with uracil (–15.02 kJ/mol), followed by other bases, all remaining above –8.37 kJ/mol except for adenine. However, in the case of aromatic amino acids in proteins, analysis of crystallographic data showed that bifurcated interactions represent only 3 % of

all C–H···O contacts.[14] Analysis of electrostatic potential maps of aromatic amino acids (phenylalanine, tyrosine and tryptophan) within the same study showed that most positive regions in the area of C–H fragments in these amino acids are positioned in the region of H atom, along the C–H direction.

The main goal of this study is to investigate the potential for hydrogen bonding between aromatic amino acids and pertechnetate compounds. Understanding the ability of pertechnetates to interact with aromatic amino acids residues through C–H···O contacts could provide valuable insights into their biochemical reactivity and implications for biological systems.

EXPERIMENTAL

Energies of C–H···O interactions were calculated for model systems containing technetium(VII) oxoacid (pertechnetic acid, $HTcO_4$) and aromatic amino acids–phenylalanine, tyrosine and tryptophan. High-level *ab initio* calculations were performed using the Gaussian 09 software.[15] Geometry optimizations of monomers employed the MP2 method[16] with the def2-TZVP basis set[17] for $HTcO_4$ and the cc-pVTZ basis set[18] for the amino acids (Tables S-1–S--IVof the Supplementary material to this paper). The basis sets for $HTcO_4$ and amino acid molecules were chosen based on recommendations from previous studies on the interaction energies of these molecules.[5,14] Vibrational frequency calculations were performed for all optimized geometries (Fig. 1) to ensure that they correspond to true minima on the potential energy surface, confirmed by the absence of imaginary frequencies.

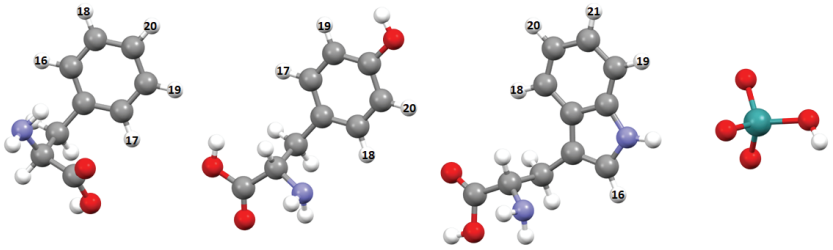

Fig. 1. Optimized geometries of phenylalanine (Phe), tyrosine (Tyr), tryptophan (Trp) and pertechnetic acid. Hydrogen atoms in the aromatic amino acids are labeled to denote potential interaction sites as C–H donors.

Interaction energies were calculated at the MP2/def2-TZVP level of theory with BSSE corrections *via* the counterpoise method[19] to ensure accuracy. An electrostatic potential (*ESP*) map was generated using the gOpenMol software[20] to visualize charge distributions and identify interaction sites. To further investigate the nature of the strongest interaction, Mulliken charges were calculated for the $HTcO_4$ species to gain insight into the electron distribution and the potential electrostatic interactions in the system.

Model systems comprising $HTcO_4$ and three different aromatic amino acid were constructed, where the Tc–O–H plane plane is positioned perpendicular to the aromatic ring plane of each amino acid (Fig. 2) to avoid simultaneous interactions with other parts of aromatic fragment.

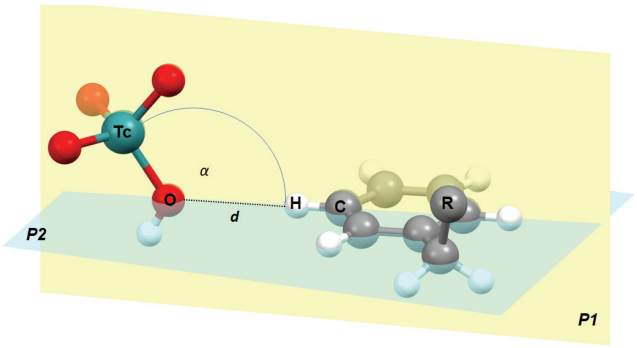

Fig. 2. General scheme of the model systems showing interactions between pertechnetic acid and the aromatic rings of phenylalanine, tyrosine and tryptophan. The plane ***P1*** contains the Tc–O–H atoms of $HTcO_4$, while plane ***P2*** is the average plane of the aromatic ring. The angle α represents the angle formed by the Tc–O···H atoms. The distance d denotes the distance between the oxygen atom of $HTcO_4$ and the hydrogen atom of the C–H donor.

The angle (α) formed between technetium, oxygen, and hydrogen atoms was set at 120°, since earlier study of C–H···O interactions showed that this geometry is most common in the case of C–H···O interactions between C–H fragment from aromatic hydrogen donor and molecules of R–O–H type.[11] The distance (d) between the oxygen atom of $HTcO_4$ and the hydrogen from the C–H donor was systematically varied from 2.0 to 2.9 Å. In the structures of phenylalanine, tyrosine, and tryptophan, multiple C–H···O interactions are possible due to the presence of different hydrogen atoms. Phenylalanine can form three distinct C–H···O interactions, tyrosine two and tryptophan five. These interactions are determined by the position of hydrogen atoms within the aromatic systems of the amino acids, each offering unique interaction sites. Different interactions were systematically analyzed to understand the role of these hydrogen donors in stabilizing complexes with pertechnetic acid. The Cambridge Structural Database (CSD)[21] was searched for all crystal structures containing X–H···O–Tc fragment containing tetracoordinate Tc atom. The H···O distance was set to be less than 2.9 Å, and the C–H···O angle values were set to be between 110 and 180°, in accordance with previously established criteria for this type of interactions.[14]

RESULTS AND DISCUSSION

Interaction energy analysis in the $HTcO_4$–phenylalanine model systems

As mentioned in the Methodology section, the model system involving $HTcO_4$ and phenylalanine includes three distinct hydrogen atoms, labeled as H16, H18 and H20, as shown in Fig. 1. The interaction energies between pertechnetic acid and these specific hydrogen atoms were analyzed in detail to investigate their contribution to the overall stability of the system. In the $HTcO_4$–Phe system, the strongest interaction was observed between the oxygen atom of $HTcO_4$ and the H16 atom of phenylalanine at a distance of 2.3 Å (Fig. 3).

This interaction exhibited an energy minimum of –9.50 kJ/mol (Fig. 4), indicating a relatively strong C–H···O hydrogen bond. In comparison, the interaction energy of linear C–H···O interaction between water and benzene molecule

was calculated to be –5.36 kJ/mol.[11] For the H18 interaction, the energy minimum was observed at slightly larger distances of 2.4 and 2.5 Å, with an interaction energy of –6.19 kJ/mol. Although weaker than the interaction with H16, it remains significant. Similarly, the interaction involving the H20 atom occurred at the same distances of 2.4 and 2.5 Å. However, the energy minimum was –5.89 kJ/mol, making it the weakest among the three model systems.

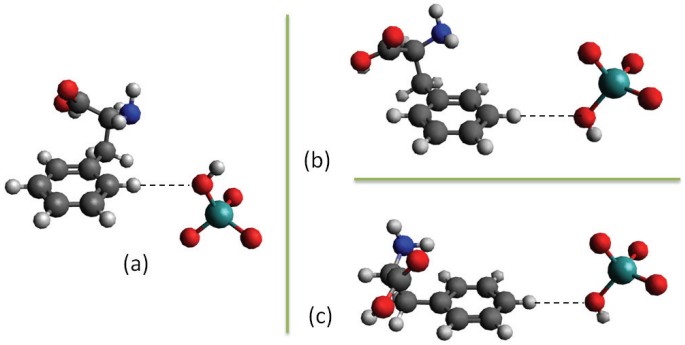

Fig. 3. Studied C–H···O interaction sites in the $HTcO_4$–Phe model system: a) interaction with the hydrogen atom labeled H16, b) interaction with the hydrogen atom H18 and c) interaction with the hydrogen atom H20.

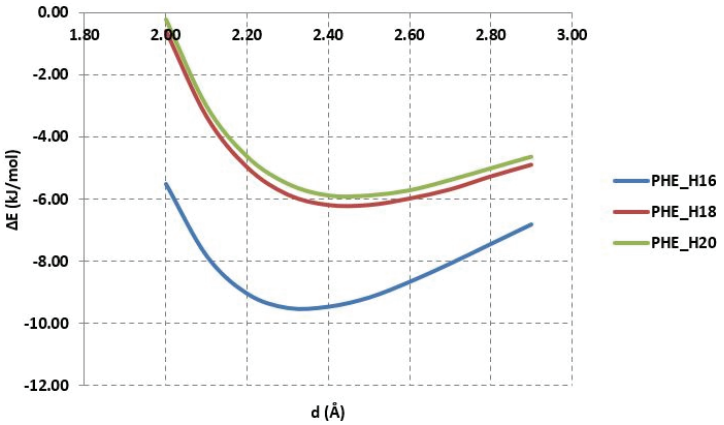

Fig. 4. Potential energy curves for the $HTcO_4$–Phe model system, showing the interactions with hydrogen atoms H16, H18 and H20 calculated at MP2/def2-TZVP level of theory.

When comparing the interaction energies, the $HTcO_4$–H16 system demonstrated the strongest interaction, followed by the interactions with H18 and H20. This suggests that the position of the hydrogen atom in the phenylalanine structure critically influences the strength of the C–H···O hydrogen bond. The interaction energies for H18 and H20 are similar, likely due to the comparable spatial positions of these hydrogen atoms relative to the aromatic ring substituent, which

does not significantly hinder or enhance their interaction with the $HTcO_4$ molecule (Fig. 3). In contrast, the stronger interaction with H16 can be attributed to the proximity of the substituent on the aromatic ring to both H16 and the interacting $HTcO_4$ molecule, which facilitates a more favorable environment for the C–H···O hydrogen bond formation.

Interaction analysis in the $HTcO_4$–tyrosine model system

The $HTcO_4$–tyrosine system was analyzed by examining the interactions involving hydrogen atoms H17 and H19 (Fig. 5).

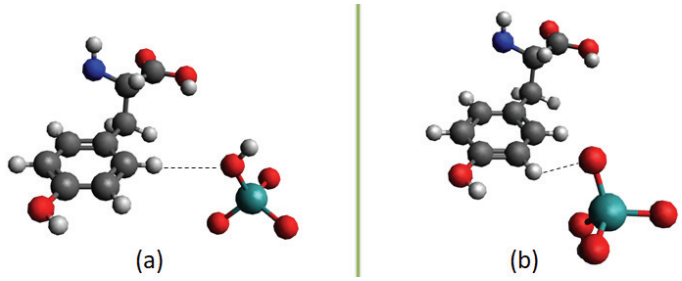

Fig. 5. Investigated C–H···O interaction sites in the model system of $HTcO_4$ and tyrosine:a) interaction with hydrogen atom denoted as H17 and b) interaction with hydrogen atom H19.

The interaction with H19 exhibited the strongest interaction energy, with a minimum of –8.61 kJ/mol at a distance of 2.4 Å (Fig. 6).

This suggests a relatively strong C–H···O hydrogen bond. In comparison, the interaction with H17 was slightly weaker, showing an energy minimum of -8.45 kJ/mol at a slightly longer distance of 2.5 Å.

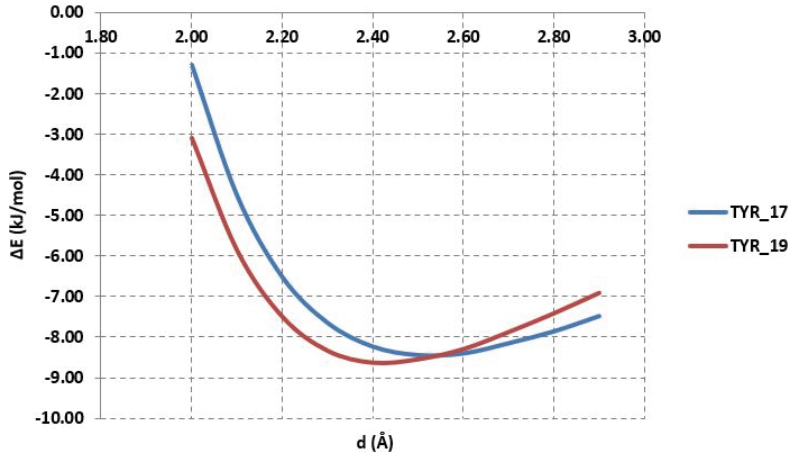

Fig. 6. Potential energy curves for the $HTcO_4$–Tyr model system, showing the interactions with hydrogen atoms H17 and H19 calculated at MP2/def2-TZVP level of theory.

Interaction analysis in the $HTcO_4$–tryptophan model system

The $HTcO_4$–tryptophan system reveals a diverse range of interaction strengths and distances, influenced by the positions of hydrogen atoms within the tryptophan structure (Fig. 7). The strongest interaction was observed between $HTcO_4$ and H18, with an interaction energy minimum of –9.54 kJ/mol occurring at the shortest distance of 2.1 Å (Fig. 8). This configuration demonstrates a highly stable hydrogen bond, attributable to the proximity of H18 to the oxygen atom of $HTcO_4$ and its favorable spatial arrangement.

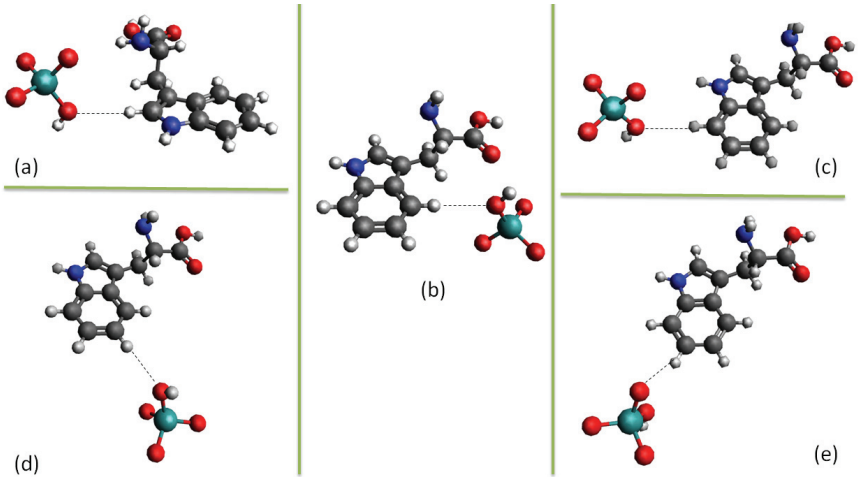

Fig. 7. C–H···O interaction sites identified in the model system of $HTcO_4$ and tryptophan: a) interaction with the hydrogen atom H16, b) interaction with H18, c) interaction with H19, d) interaction with H20 and e) interaction with H21.

The interaction with H16, though slightly weaker than H18, also represents a significant stabilization with an energy minimum of –9.41 kJ/mol. The distance for this interaction ranged between 2.3 and 2.4 Å, slightly longer than for H18. This suggests that while H16 is capable of forming a strong C–H···O bond, its geometric positioning relative to $HTcO_4$ is marginally less optimal than H18.

Moving to interactions with H19, H20 and H21, a progressive weakening of the interaction energy was noted. For H19, the energy minimum was measured at –6.60 kJ/mol at distances of 2.4 and 2.5 Å. Although the distance is comparable to that observed for H16, the interaction strength is notably lower, indicating that the electronic environment and substituent effects around H19 influence its bonding capacity negatively. The interactions with H20 and H21 were the weakest, with energy minima of –5.56 and –5.48 kJ/mol, respectively, occurring at a distance of 2.5 Å. These interactions, while still indicative of C–H···O hydrogen bonding, are substantially weaker, likely because the substituent on the aromatic structure of tryptophan is positioned further away from the interacting $HTcO_4$

molecule, reducing its capacity to enhance the interaction through proximity effects. The observed hierarchy in interaction strengths (H18 > H16 > H19 > H20 > H21) underscores the critical role of hydrogen atom positioning and the surrounding molecular environment in determining the strength of the hydrogen bond. The exceptionally strong interaction with H18 and its shorter distance suggests a synergistic interplay of steric and electronic factors. On the other hand, the interactions with H20 and H21 reflect weaker hydrogen bonding, potentially constrained by the aromatic system's substituent effects and the spatial orientation of $HTcO_4$.

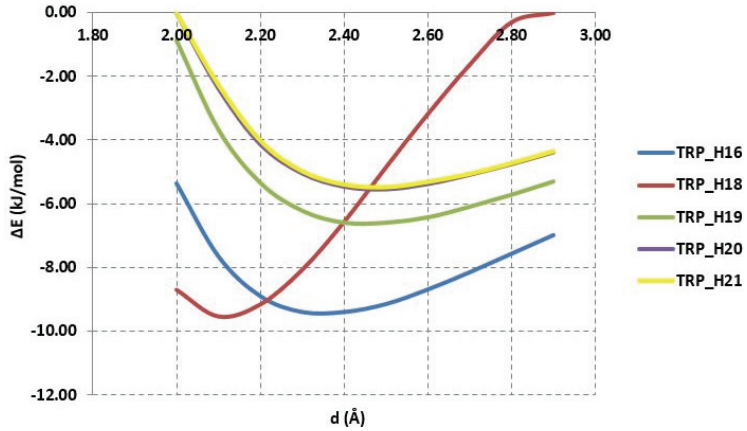

Fig. 8. Potential energy curves for the $HTcO_4$–Trp model system, showing the interactions with hydrogen atoms H16, H18, H19, H20 and H21 calculated at MP2/def2-TZVP level of theory.

In comparing the strongest interactions across the three model systems ($HTcO_4$–phenylalanine, $HTcO_4$–tryptophan and $HTcO_4$–tyrosine), the interaction energies varied, reflecting the differences in atomic positions and the nature of the interactions. Among all systems, the strongest interaction was observed in the $HTcO_4$–tryptophan system, with an energy minimum of –9.53 kJ/mol at a distance of 2.1 Å. This was followed by the $HTcO_4$–phenylalanine system, which displayed an energy minimum of –9.49 kJ/mol at 2.3 Å. The weakest interaction was found in the $HTcO_4$–tyrosine system, with a minimum energy of –8.61 kJ/mol at 2.4 Å. These results demonstrate that the position, of the hydrogen atom and the spatial arrangement of the substituents in each amino acid, significantly influence the strength of the C–H···O hydrogen bonding interactions.

Molecular Electrostatic Potential Surfaces (MEPS)

To further understand the strengths of the interactions, we calculated the electrostatic potential map (Fig. 9) for pertechnetic acid. Since C–H···O interact-

ions are largely governed by electrostatic forces, the map was analyzed to reveal key regions of negative and positive potentials.

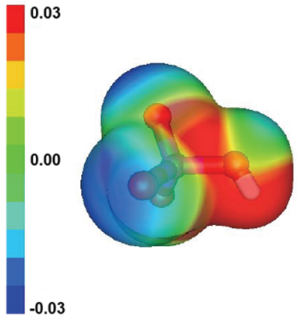

Fig. 9. Electrostatic potential (*ESP*) map of pertechnetic acid with the contour map.

Blue color represents regions of negative potential, which are located around the oxygen atoms, indicating their role as hydrogen bond acceptors. In contrast, red represents positive potential, which is observed around the hydrogen and metal atoms. This distribution supports the concept that the oxygen atoms are potential hydrogen bond acceptors in these interactions.

To quantitatively describe the distribution of charges, Mulliken population analysis was performed and calculated Mulliken charges are given in Fig. 10.

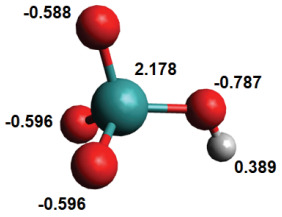

Fig. 10. Mulliken atomic charges calculated for $HTcO_4$ molecule. The oxygen atom bonded to both Tc and H exhibits a significantly more negative charge (–0.787), making it the primary site for strong C–H···O interactions with aromatic C–H donors.

Distribution of Mulliken charges shows that oxygen atoms connected only to the Tc atom have similar values of Mulliken charges (from –0.596 to –0.588), while oxygen atom connected to both Tc and H atom has significantly more negative value of Mulliken charge (–0.787), due to the polarization effects resulting from its dual bonding to Tc and H. These results confirm that the interacting oxygen atom is indeed the most likely to form the strongest C–H···O interaction with aromatic C–H donors from studied amino acids.

Analysis of crystal structures

The Cambridge Structural Database was searched for all crystal structures containing X–H···O–Tc interactions involving tetracoordinated Tc species. Four crystal structures met the criteria used in the CSD search (KACWAO, KACWES, WAHQIG, YAKZUF). A fragment of the KACWAO crystal structure is shown in Fig. 11.

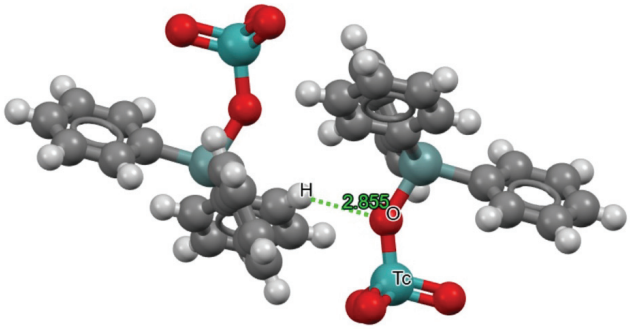

Fig. 11. C–H···O–Tc interaction identified in a fragment of the KACWAO crystal structure.

In this crystal structure, a C–H···O interaction involving an aromatic C–H donor and an oxygen atom bonded to Tc was detected. The distance between the interacting O and H atoms is less than 2.9 Å, which is consistent with expected values for C–H···O contacts.[10] The C–H···O angle is 145.24°, falling within the typical range for such interactions (110–180°).[10] A similar interaction was observed in the other extracted crystal structures. The analysis of geometric parameters in these structures confirms that C–H···O interactions between aromatic C–H donors and the O–Tc fragment indeed occur in experimentally determined crystal structures.

CONCLUSION

The goal of this study was to investigate and characterize C–H···O interactions between pertechnetic acid molecule and aromatic amino acids: phenylalanine, tyrosine and tryptophan. Interaction energies, calculated at the MP2/def2--TZVP level, confirmed strong linear C–H···O interactions, with the strongest observed for the $HTcO_4$–tryptophan system (–9.53 kJ/mol at 2.1 Å). Very strong interactions were also observed in $HTcO_4$– phenylalanine (–9.49 kJ/mol at 2.3 Å) and $HTcO_4$–tyrosine (–8.61 kJ/mol at 2.4 Å) systems. Compared to similar systems involving nucleobases and aromatic molecules, the interactions between $HTcO_4$ and aromatic amino acids as C–H donors are among the strongest known. The molecular electrostatic potential analysis revealed that there are areas of strong negative potential around all oxygen atoms in the $HTcO_4$ molecule. Mulliken population analysis showed that the most negative oxygen atom is the one in the O–H fragment of $HTcO_4$, making it the most likely candidate for hydrogen bond acceptors in C–H···O interactions. The analysis of geometric parameters confirms that C–H···O interactions between aromatic C–H donors and the O–Tc fragment are present in experimentally determined crystal structures. These findings highlight the role of C–H···O contacts in systems containing pertechnetate species and aromatic amino acids. Also, presented results can be significant for the recognition of often-overlooked weak hydrogen bonds in protein–$HTcO_4$ adducts.

SUPPLEMENTARY MATERIAL

Additional data and information are available electronically at the pages of journal website: https://www.shd-pub.org.rs/index.php/JSCS/article/view/13222, or from the corresponding author on request.

Acknowledgements. This research has been supported by the Ministry of Science, Technological Development and Innovation of Republic of Serbia (Contract numbers: 451-03-66/2024-03/200026 and 451-03-66/2024-03/200168). The authors would like to thank Zorana Zeković for her assistance with interaction energy calculations

ИЗВОД

КВАНТНОХЕМИЈСКО ПРОУЧАВАЊЕ C–H···O ИНТЕРАКЦИЈА ИЗМЕЂУ $HTcO_4$ И АРОМАТИЧНИХ АМИНОКИСЕЛИНА

МИЉАН БИГОВИЋ[1], ИВАНА С. ВЕЉКОВИЋ[2], ЈЕЛЕНА ПЕТРОВИЋ[3] и ДУШАН Ж. ВЕЉКОВИЋ[4]

[1]Природно математички факултет Универзитета Црне Горе, Подгорица, Црна Гора, [2]Универзитет у Београду – Институт за хемију, технологију и металургију – Институт од националног значаја за Републику Србију, Београд, [3]Центар за нуклеарну медицину са позитронском емисионом томографијом, Универзитетски клинички центар Србије; Универзитет у Београду, Медицински факултет, Београд и [4]Универзитет у Београду – Хемијски факултет, Београд

У овом раду су проучаване C–H···O интеракције између $HTcO_4$ и ароматичних аминокиселина (фенилаланин, тирозин и триптофан) коришћењем квантнохемијских прорачуна. Резултати прорачуна енергије интеракција су комбиновани са анализом молекулских електростатичких потенцијала (*MEP*) ради бољег разумевања природе ових интеракција. Најјача интеракција је израчуната у систему $HTcO_4$–триптофан са минимумом од –9,53 kJ/mol на растојању од 2,1 Å. Фенилаланин је показао сличну јачину интеракције (–9,49 kJ/mol), док тирозин има најслабију интеракцију (–8,61 kJ/mol). Анализа мапе електростатичког потенцијал је потврдила електростатичку природу C–H···O интеракција, наглашавајући улогу атома кисеоника као акцептора водоника у водоничним везама. Ови резултати пружају значајан увид у улогу C–H···O интеракција у молекулском препознавању и дизајну функционалних материјала са пертехнетатским јединицама. Добијени резултати указују да положај атома водоника у односу на супституенте на ароматичном прстену утиче на енергију ових интеракција. Ови резултати могу бити од великог значаја за препознавање нових нековалентних контаката између пертехницијумове киселине и фрагмената амино киселина, као и за боље разумевање стабилности комплекса пертехнетата и пептида.

(Примљено 25. јануара, ревидирано 4. фебруара, прихваћено 7. фебруара 2025)

REFERENCES

1. D. Papagiannopoulou, *J. Label. Compd. Radiopharm*. **60** (2017) 502 (https://doi.org/10.1002/jlcr.3531).
2. J. G. O'Connell-Danes, B. T. Ngwenya, C. A. Morrison, J. B. Love, *Angew. Chem. Int. Ed.* **63** (2024) e202409834 (https://doi.org/10.1002/anie.202409834)
3. S. M. Rathmann, Z. Ahmad, S. Slikboer, H. A. Bilton, D. P. Snider, J. F. Valliant, in *Radiopharmaceutical Chemistry,* J. Lewis, A. Windhorst, B. Zeglis, Eds., Springer, Cham., 2019, p. 311 (https://doi.org/10.1007/978-3-319-98947-1_18)
4. J. Chen, Z. Cheng, Y. Miao, S. S. Jurisson, T. P. Quinn, *Cancer* **94** (2002) 1196 (https://doi.org/10.1002/cncr.10284)

5. D. Grödler, S. Burguera, A. Frontera, E. Strub, *Chem. Eur. J.* **30** (2024) e202400100 (https://doi.org/10.1002/chem.202400100)
6. R. Waibel, R. Alberto, J. Willuda, R. Finnern, R. Schibli, A. Stichelberger, A. Egli, U. Abram, J.-P. Mach, A. Plückthun, P. A. Schubiger, *Nat. Biotechnol.* **17** (1999) 897 (https://doi.org/10.1038/12890)
7. M. Bartholomä, J. Valliant, K. P. Maresca, J. Babich, J. Zubieta, *Chem. Commun.* **5** (2009) 493 (https://doi.org/10.1039/B814903H)
8. M. B.-U. Surfraz, R. King, S. J. Mather, S. Biagini, P. J. Blower, *J. Inorg. Biochem.* **103** (2009) 971 (https://doi.org/10.1016/j.jinorgbio.2009.04.007)
9. D. Hernández-Valdés, R. Alberto, U. Jáuregui-Haza, *RSC Adv.* **6** (2016) 107127 (https://doi.org/10.1039/C6RA23142J)
10. K. Manikandan, S. Ramakumar, *Proteins* **56** (2004) 768 (https://doi.org/10.1002/prot.20152)
11. D. Ž. Veljković, G. V. Janjić, S. D. Zarić, *CrystEngComm* **13** (2011) 5005 (https://doi.org/10.1039/C1CE05065F)
12. D. Ž. Veljković, *J. Mol. Graph. Model.* **80** (2018) 121 (https://doi.org/10.1016/j.jmgm.2017.12.014)
13. D. Ž. Veljković, V. B. Medaković, J. M. Andrić, S. D. Zarić, *CrystEngComm* **16** (2014) 10089 (https://doi.org/10.1039/C4CE00595C)
14. J. Lj. Dragelj, I. M. Stanković, D. M. Božinovski, T. Meyer, D. Ž. Veljković, V. B. Medaković, E.-W. Knapp, Snežana D. Zarić, *Cryst. Growth Des.* **16** (2016) 1948 (https://doi.org/10.1021/acs.cgd.5b01543)
15. *Gaussian 09, Revision D.01*, Gaussian, Inc., Wallingford, CT, 2013
16. C. Moller, M. S. Plesset, *Phys. Rev.* **46** (1934) 618 (https://doi.org/10.1103/PhysRev.46.618)
17. F. Weigend, *Phys. Chem. Chem. Phys.* **8** (2006) 1057 (https://doi.org/10.1039/B515623H)
18. T. H. Dunning Jr., *J. Chem. Phys.* **90** (1989) 1007 (https://doi.org/10.1063/1.456153)
19. S. F. Boys, F. Bernardi, *Mol. Phys.* **19** (1970) 553 (https://doi.org/10.1080/00268977000101561)
20. L. Laaksonen, *J. Mol. Graphics* **10** (1992) 33 (https://doi.org/10.1016/0263-7855(92)80007-Z)
21. C. R. Groom, I. J. Bruno, M. P. Lightfoot, S. C. Ward, *Acta Cryst., B* **72** (2016) 171 (https://doi.org/10.1107/S2052520616003954).

Journal of the Serbian Chemical Society
JSCS@tmf.bg.ac.rs • www.shd.org.rs/JSCS
J. Serb. Chem. Soc. 90 (6) S222–S226 (2025) *Supplementary material*

SUPPLEMENTARY MATERIAL TO

Quantum-chemical study of C–H···O interactions between $HTcO_4$ and aromatic amino acids

MILJAN BIGOVIĆ[1], IVANA S. VELJKOVIĆ[2], JELENA PETROVIĆ[3] and DUŠAN Ž. VELJKOVIĆ[4]*

[1]Faculty of Natural Sciences and Mathematics, University of Montenegro, Podgorica, Montenegro, [2]University of Belgrade – Institute for Chemistry, Technology and Metallurgy – National Institute of the Republic of Serbia, Belgrade, Serbia, [3]Center for Nuclear Medicine with PET, University Clinical Center of Serbia, Belgrade, Serbia; Faculty of Medicine, University of Belgrade, Belgrade, Serbia and [4]University of Belgrade - Faculty of Chemistry, Belgrade, Serbia

J. Serb. Chem. Soc. 90 (6) (2025) 741–752

OPTIMIZED GEOMETRIES

This section provides the Cartesian coordinates (XYZ format) of the optimized geometries for phenylalanine (Phe), tyrosine (Tyr), tryptophan (Trp), and pertechnetic acid ($HTcO_4$). Geometry optimizations were carried out using the MP2 method. The def2-TZVP basis set was employed for $HTcO_4$, while the cc-pVTZ basis set was used for the amino acids. The optimized structures serve as the starting point for further computational analyses presented in the main text.

* Corresponding author. E-mail: vdusan@chem.bg.ac.rs

Table S-I. Cartesian coordinates (XYZ) of optimized **Phe** at the MP2/cc-pVTZ level.

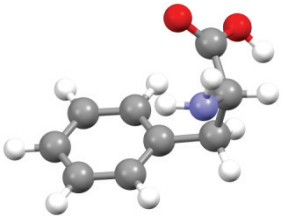

N	1.16448	1.44041	2.24973
C	1.96538	1.36108	1.04665
C	1.68598	2.48823	0.05467
O	0.77677	3.26951	0.15219
C	1.74035	-0.00674	0.37019
C	0.30752	-0.19870	-0.03773
C	-0.59606	-0.82768	0.82429
C	-0.15815	0.29003	-1.26295
C	-1.93690	-0.96484	0.47097
C	-1.49732	0.15407	-1.61815
C	-2.39035	-0.47284	-0.75106
O	2.54592	2.56550	-1.00036
H	3.02018	1.42493	1.33085
H	2.03211	-0.76905	1.09159
H	2.39050	-0.10836	-0.50105
H	-0.24229	-1.20709	1.77453
H	0.53023	0.77873	-1.94161
H	-2.62371	-1.45600	1.14678
H	-1.84220	0.53675	-2.56887
H	-3.43023	-0.57969	-1.02727
H	0.18669	1.44066	1.97527
H	1.31202	2.34361	2.68583
H	3.22153	1.88402	-0.90283

Table S-II. Cartesian coordinates (XYZ) of optimized **Tyr** at the MP2/cc-pVTZ level.

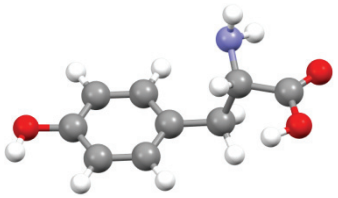

N	1.69351	1.91821	-1.04695
C	2.14635	0.56433	-0.79248
C	3.44810	0.22924	-1.51150
O	3.83835	0.81089	-2.49154
C	1.07272	-0.43929	-1.26216
C	-0.13629	-0.43178	-0.37457
C	-0.27745	-1.39328	0.62794
C	-1.12722	0.54800	-0.49399
C	-1.37047	-1.38262	1.49136
C	-2.22321	0.56729	0.35986
C	-2.34714	-0.39808	1.35782
O	-3.44718	-0.32981	2.16677
O	4.14390	-0.82796	-1.01673
H	2.28386	0.43792	0.28466
H	0.80969	-0.17274	-2.28822
H	1.49593	-1.44554	-1.29190
H	0.46821	-2.17283	0.73284
H	-1.02949	1.30918	-1.25463
H	-1.46617	-2.14157	2.25877
H	-2.99110	1.32230	0.26654
H	-3.40237	-1.05705	2.79612
H	2.27574	2.57315	-0.53848
H	1.86716	2.11559	-2.02851
H	3.70018	-1.14567	-0.22141

Table S-III. Cartesian coordinates (XYZ) of optimized **Trp** at the MP2/cc-pVTZ level.

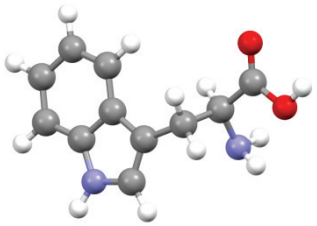

N	-0.50791	3.10300	-1.76549
C	0.61173	2.45668	-1.10309
C	1.97044	3.09398	-1.30539
O	2.87254	3.08085	-0.49936
C	0.71264	0.99188	-1.57380
C	-0.41996	0.17802	-1.05934
C	-1.56780	-0.18913	-1.72448
C	-0.55171	-0.31478	0.27567
N	-2.39295	-0.88836	-0.87520
C	-1.80232	-0.98350	0.35981
C	0.26950	-0.25531	1.41404
C	-2.24345	-1.59347	1.53583
C	-0.16886	-0.85723	2.58291
C	-1.41111	-1.51950	2.64331
O	2.10152	3.64324	-2.54037
H	-1.86208	0.00846	-2.74183
H	-3.28754	-1.27133	-1.12336
H	1.22648	0.25094	1.37995
H	-3.19679	-2.10336	1.58712
H	0.45100	-0.82023	3.46837
H	-1.72229	-1.97924	3.57139
H	0.43436	2.45402	-0.02839
H	0.73544	0.98552	-2.66610
H	1.66003	0.57457	-1.22524
H	-0.66100	4.02361	-1.37259
H	-0.27735	3.24834	-2.74161
H	3.01566	3.96288	-2.58086

Table S-IV. Cartesian coordinates (XYZ) of optimized **$HTcO_4$** at the MP2/def2-TZVP level.

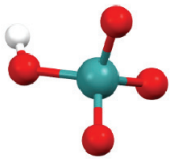

Tc	-0.03238	0.00466	0.00007
O	-0.63619	-0.84287	-1.39854
O	-0.63702	-0.84664	1.39592
O	-0.71239	1.60410	0.00181
O	1.86083	0.14394	0.00057
H	2.39044	-0.66878	-0.00089

Journal of the Serbian Chemical Society
JSCS@tmf.bg.ac.rs • www.shd.org.rs/JSCS
J. Serb. Chem. Soc. *90* (6) 753–766 (2025)
JSCS–5418
Original scientific paper
Published 23 June, 2025

Synthesis and characterization of zeolite obtained from Toraja natural montmorillonite

PAULINA TABA[1]*, ST. FAUZIAH[1], HASNAH NATZIR[1], NUNUK H. SOEKAMTO[1], ROSALIA S. SARUNGALLO[2], NUR W. NAHRU[1], YULI ASTUTI[1] and IDA I. AMIN[3]

[1]Department of Chemistry, Faculty of Science, Hasanuddin University, Indonesia, [2]Chemical Engineering, Kristen Indonesia Paulus Makassar University, Indonesia and [3]Department of Technological of Metallurgy Extraction, Faculty of Vocational, Hasanuddin University, Indonesia

(Received 12 October, revised 8 November 2024, accepted 5 February 2025)

Abstract: Zeolites are an alternative material for treating heavy metal-containing waste. Synthetic zeolites exhibit excellent purity and particle size uniformity, which has led many researchers to explore their synthesis, including the use of natural minerals. This work aims to synthesize zeolites using the hydrothermal method with aluminosilicate sources from Toraja natural minerals. Toraja natural minerals, primarily composed of montmorillonite, hydrothermally react with NaOH at varying concentrations to form analcime (ANA) and cancrinite (CAN) zeolites. In the research we also examined the reaction time for zeolite formation. X-ray diffraction (XRD) analysis revealed that ANA and CAN exhibit tetragonal and hexagonal crystal structures, respectively. The Si/Al mole ratios were determined to be 2.40 for ANA and 1.27 for CAN, based on EDX analysis. The Fourier transform infrared (FTIR) spectra exhibit typical absorption bands within the spectral region of 700–400 cm^{-1}, with increasing intensity observed at higher NaOH concentrations. ANA zeolite displays distinctive spectral features below 650 cm^{-1}, attributed to double-ring vibrations in its structure. In contrast, triplet bands at 676, 622 and 565 cm^{-1} in the synthesized materials confirm the characteristic structure of cancrinite. SEM analysis revealed trapezium-shaped analcime crystals with an average size of 24 μm and rod-shaped cancrinite crystals with a length of 1.66 μm. Toraja minerals, particularly montmorillonite, contain secondary building units that form different zeolites depending on reaction conditions.

Keywords: analcime; cancrinite; fabriesite; hydrothermal method.

* Corresponding author. E-mail: paulinataba@unhas.ac.id
https://doi.org/10.2298/JSC241012015T

INTRODUCTION

Zeolites are alternative materials for treating heavy metal-containing waste due to their high adsorption and cation exchange capacities, which make them effective in removing contaminants from the environment.[1,2] Their structure is characterized by a microporous crystalline framework composed of tetrahedral units of SiO_4 and AlO_4^-, with Si or Al atoms at the center and O atoms at the corners. This framework forms pores and channels that facilitate the migration of species into the interstitial spaces.[3] The negative charge generated by Al^{3+} bonded to oxygen is balanced by cations such as Na^+, K^+, Ca^{2+} and Mg^{2+} within the cavities.[4]

Zeolites can occur naturally or be synthesized using various methods, with starting materials derived from either natural resources or chemical reagents. Natural zeolites often exhibit a high ratio of Si/Al, but they also include numerous impurities in the form of metal oxides, which leads to a comparatively small surface area.[5] On the other hand, synthetic zeolites offer better purity and uniform particle size, though their production is relatively costly.[6] Hence, the production of zeolites from cost-effective raw materials, such as natural minerals, has attracted considerable interest among scientists. For example, volcanic belt regions have abundant natural mineral resources containing several low-quality zeolite frameworks or zeolitic building blocks.[7] Previous research has examined the production of zeolites from natural minerals, including pumice,[8] waste basalt powder,[9] Mesawa feldspar,[10] kaolin[11,12] and aluminum waste.[13] These researchers highlight the advantages of using natural minerals, which can reduce costs and utilize unused natural materials.

Due to its frequent formation and ease of identification, analcime (ANA) is one of the most commonly synthesized forms of zeolite. The ANA zeolite is a low-silica zeolite characterised by a Si/Al ratio ranging from 1.8 to 2.8. Its molecular formula is $NaAlSi_2O_6{\cdot}H_2O$, which has cavities occupied by Na^+ that can be exchanged with other cations. Zeolite ANA can be used as an adsorbent,[14] catalyst[15] and in waste treatment.[16] ANA is often formed alongside cancrinite (CAN). CAN is a zeolite with a low silica content, characterized by a Si/Al ratio of around 1. Its molecular formula is $Na_6[Al_6Si_6O_{24}]{\cdot}2NaX{\cdot}6H_2O$, where X may be OH^-, NO_3^-, $½CO_3^{2-}$ or $½SO_4^{2-}$. Given its significant cation exchange capacity, CAN has the potential to serve for the removal of metal ions[17] and nitrate ions in groundwater samples.[18]

Based on the above description, this research aims to synthesize zeolites using natural minerals from Toraja (South Sulawesi). Toraja natural minerals have been extensively utilized both directly and through preliminary activation. Efendy *et al.*[19] employed Toraja natural zeolites to reduce Ca^{2+} concentrations in water sources. Kartawa and Kusumah[7] also reported that Toraja natural minerals are used in aquaculture (shrimp farming), agriculture, waste absorption and other

industrial fields. However, the synthesis of these minerals into other types of zeolites through principles of transformation and recrystallization has not yet been conducted. Toraja natural minerals contain montmorillonite, as well as quartz and feldspar. These three components contain silica and alumina, which can serve as alternative raw materials for zeolite synthesis.

In this work we have synthesized zeolites using a hydrothermal method and direct synthesis, without pre-activation and without organic templates in the zeolite precursors. This method is considered simple, rapid and environmentally friendly due to the absence of organic templates that must be removed after synthesis. The synthesis of zeolites follows the principle of recrystallization,[10] where the mechanism involves dissolving silica and alumina from natural minerals under alkaline conditions, followed by the zeolite crystal formation process. Synthesis was carried out with varying NaOH concentrations (1.2, 2.5, 5 M) and reaction times (12, 24, 72 h). X-Ray fluorescence (XRF), X-ray diffraction (XRD) and scanning electron microscope energy dispersive X-ray (SEM-EDX) can be employed to analyze the properties of the synthesized zeolites. Furthermore, the zeolite framework can be examined for its functional groups by Fourier transform infrared spectroscopy (FTIR). The specific surface area and the distribution of pore sizes can be calculated using a surface area analyzer (SAA) with the Brunauer–Emmett–Teller (BET) and the Barrett–Joyner–Halenda (BJH) methods, respectively.

EXPERIMENTAL

Chemicals and reagents

The materials used in this study were natural minerals containing montmirillonite sourced from Toraja, South Sulawesi, Indonesia (which were processed to pass through a 200 mesh sieve), sodium hydroxide pro-analysis (in pellets, 99 % concentration, Merck) was purchased from Intraco (Makassar, Indonesia) and distilled water.

Hydrothermal synthesis of zeolite from Toraja natural minerals

Zeolite synthesis was performed using a hydrothermal method. An 1.2 M NaOH solution was prepared by dissolving 0.8585 g of NaOH in 18 g of water. Subsequently, 0.7543 g of the natural mineral sample, constituting 4 mass % of the mixture, was added to the NaOH solution. The mixture was stirred until it was fully combined and then moved to a tightly sealed autoclave. It was then heated in an oven at 170 °C for 72 h. The resulting solid was efficiently filtered using vacuum filtration and thoroughly washed until the pH reached a neutral level. The final product was dehydrated in a 100 °C oven for 24 h. Different concentrations of NaOH were used, specifically 2.5 and 5 M. Additionally, the reaction time was varied by repeating the process at a NaOH concentration of 5 M for 12 and 24 h. The solid products were further analyzed by XRD, FTIR, SEM-EDX and SAA.

XRF, XRD, FTIR, SEM-EDX and SAA analysis

The samples chemical composition was determined using XRF analysis performed with an EDX-720 XRF instrument. The elements focused on included Si, K, Ca, Ti, V, Mn, Fe, Zn, Al and Rh. XRD patterns were analyzed using a Shimadzu X-ray diffractometer with CuKα

radiation. Phase identification was performed by comparing the diffraction patterns with the powder diffraction database of the International Council for Phase Identification (ICDD), the zeolite database file of the International Zeolite Association (IZA), the files of the Joint Committee on Powder Diffraction Standards (JCPDS), and related publications. FTIR spectra were obtained using a Shimadzu IRSPIRIT-T instrument equipped with QATR-S in the 4000–500 cm^{-1} range. Potassium bromide was employed as both a diluent and binder. Characterisation of morphology was conducted using a scanning electron microscope (SEM-EDX-SU-3500). In addition, nitrogen adsorption–desorption isotherms were measured at a temperature of 77.35 K using an Altamira Micro 200 equipment. The specific surface area was determined by measuring linear isotherms following the BET method. Porosity size distribution was evaluated simultaneously using the BJH technique.

RESULTS AND DISCUSSION

Chemical and mineralogical properties of Toraja natural minerals

The chemical composition of Toraja natural minerals is crucial in identifying the specific end product produced throughout the synthesis procedure. Table I provides the chemical composition of the Toraja natural minerals. The mineral powder primarily contains SiO_2 and Al_2O_3, with an SiO_2/Al_2O_3 ratio of 1.51, making it suitable for use as a raw material for synthesizing zeolites with a low Si/Al ratio.[20]

The XRD pattern indicates that Toraja natural minerals are crystalline, as shown in Fig. 1a. It can be confirmed by the existence of prominent peaks for 2θ values of 19.49, 20.97, 26.53, 29.46, 35.04, 47.35, 50.00, 59.97, 62.31, 68.47 and 74.93°. Peaks of the highest intensity are associated with montmorillonite (ICDD 13-0315), 41.4 %, and quartz (ICDD 46-1045), 30.3 %, whereas peaks of lower strength indicate the presence of feldspar (ICDD 01-0083), 15.4 %, and magnetite (ICDD 00-0551), 13.0 %. Additionally, the FTIR spectrum results indicate Toraja natural minerals as aluminosilicate-containing materials (Fig. 1b). Spectral peaks at 3621 and 1633 cm^{-1} correspond to the stretching and bending vibrations of O–H groups caused by water molecules that are confined within the crystal lattice.[21] The absorption band at around 993 cm^{-1} is characteristic of the asymmetric stretching vibration of Si–O–Si. The band corresponding with the

TABLE I. Composition of Toraja natural minerals

Analyte	Content, %
SiO_2	56.55
Al_2O_3	37.39
K_2O	2.50
Fe_2O_3	1.97
CaO	1.20
TiO_2	0.30
MnO	0.05
V_2O_5	0.02
ZnO	0.01

Al–Al–OH bending vibrations was observed at 917 cm^{-1}. The Al–O and Si–O out-of-plane vibrations were assigned to the band at position 691 cm^{-1}. In addition, the peaks at 516 and 464 cm^{-1} correspond to the bending vibrations of Al–O–Si and Si–O–Si.[22]

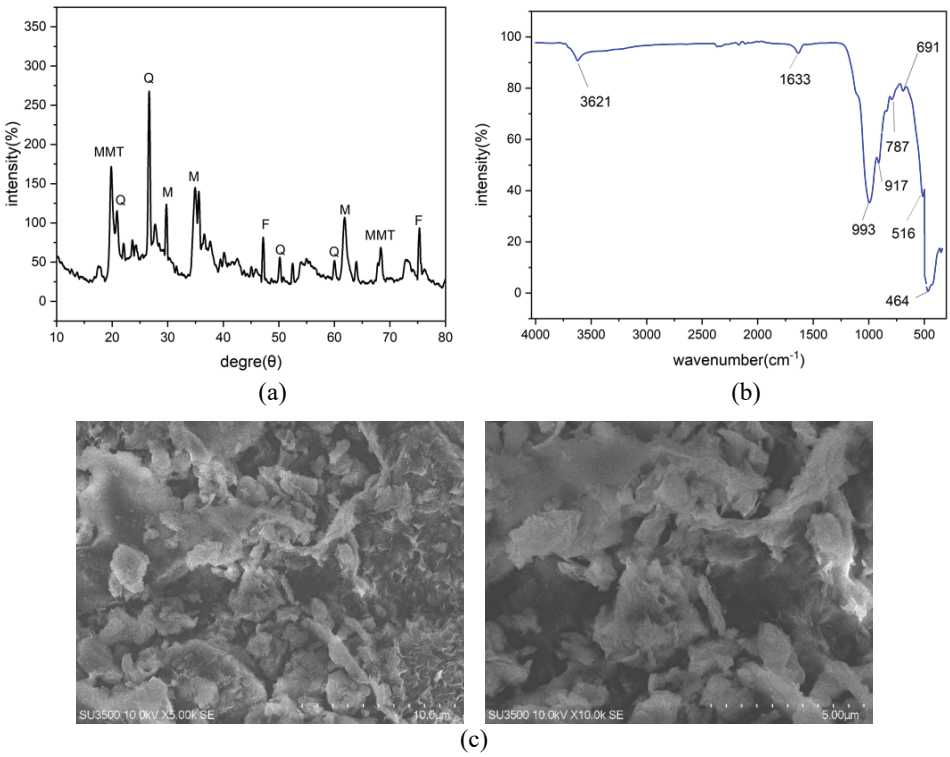

Fig. 1. a) XRD pattern; b) FTIR spectrum; c)SEM image of Toraja natural mineral.

Fig. 1c illustrates the morphology of Toraja natural mineral particles, which are sheet-like – a characteristic of montmorillonite, which consists of silica tetrahedral and octahedral sheets.[23] Overall characterization results show that Toraja natural minerals consist of montmorillonite with multiple phases, thus enhancing their potential utilization through further processing.

Zeolite ANA and CAN synthesis

This method entails the concurrent addition and stirring of the precursor agent and alkali (NaOH). The hydrothermal synthesis is conducted at a temperature of 170 °C, with varying concentrations and reaction times. The hydrothermal conversion of Toraja natural minerals into zeolites involves the dissolution of montmorillonite, quartz and feldspar, followed by zeolite crystallization.

Table II presents the experimental parameters for synthesizing zeolites from Toraja natural minerals.

TABLE II. Experimental parameters for synthesizing zeolites from Toraja natural minerals

Sample	NaOH mol/L	Hydrothermal conditions		Mineral type of sample	Rendemen %	Crystallinity %
		t / °C	τ / h			
P1	1.2	170	72	ANA	42.25	58.66
P2	2.5	170	72	CAN, FAB	22.78	51.49
P3a	5.0	170	72	CAN	45.60	74.98
P3b	5.0	170	24	CAN	42.27	70.94
P3c	5.0	170	12	CAN	38.94	68.87

XRD patterns of the synthesized samples exhibit distinct zeolite types, as shown in Fig. 2. At a concentration of 1.2 M, zeolite ANA is formed. ANA tends

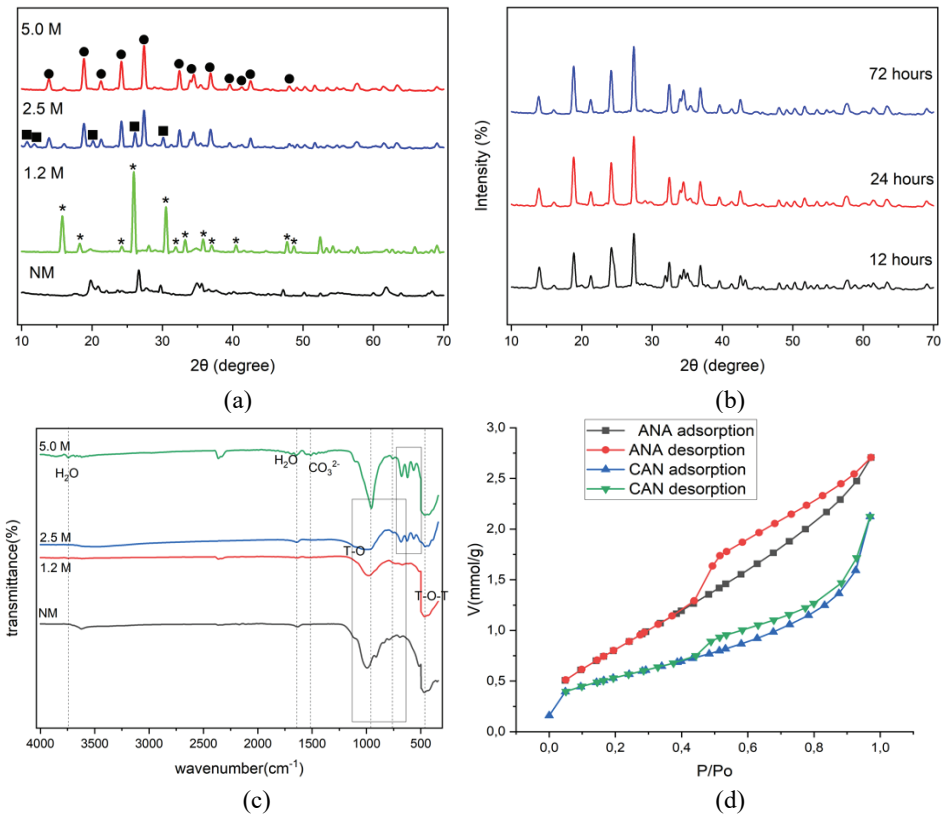

Fig. 2. XRD patterns of: a) Toraja natural minerals and samples synthesized at 1.2, 2.5, 5.0 M of NaOH (*ANA, ■NHI, ●CAN); b) the sample that was synthesized with 5M NaOH with variated of reaction time; c) FTIR spectra within the wavelength range of 4000–400 cm^{-1} of Toraja natural minerals and samples synthesized at 1.2, 2.5, 5.0 M of NaOH; d) N_2 isotherm adsorption–desorption of ANA and CAN zeolite.

to form at low base concentrations.[24] Under these conditions, the increased Si content promotes the growth of the metastable analcime phase. As the concentration of NaOH is raised to 2.5 M, zeolite CAN is produced, which is mixed with fabriesite, more commonly known as nepheline hydrate (NHI). This result comes from NHI being made if the NaOH concentration is suboptimal for CAN formation, specifically at concentrations of 2–4 M. At even higher concentrations, specifically 5 M NaOH, the product obtained is CAN. The study shows that the concentration of NaOH plays a crucial role in the disintegration of minerals in raw materials and the consequent creation of zeolites. Increasing NaOH concentration changes the crystal phases from ANA to NHI to CAN.

The crystal structure of ANA comprises a silica–alumina framework, cavities, cations and irregular channels.[25] The silica–alumina lattice is formed by 4-, 6- and 8-membered rings that create cage-like structures. These cages contain smaller cavities where Na^+ is located in octahedral coordination. Water molecules occupy continuous channels along a triple screw axis, formed by the coordination of $[AlO_4]^-$ and $[SiO_4]$ tetrahedra. Silicon and aluminum atoms are unevenly distributed within the lattice.[26]

In contrast, the crystal structure of CAN zeolite is characterized by a hexagonal framework formed by several five-membered rings of tetrahedra organized in an ABAB sequence. The adjacent layers of six-membered rings are connected by four-membered rings to form *ε*-cages (a characteristic composite building unit (CBU) of cancrinite). This arrangement creates continuous channels composed of 12-membered rings with free dimensions and effective pore diameter. These channels are filled with CO_3^{2-} groups aligned along the *c*-axis. Additionally, the cages can also accommodate Na^+, Ca^{2+}, Cl^- and H_2O molecules.

As previously mentioned, between the formation transformations of ANA and CAN, there is NHI, which is known to have a framework similar to CAN but with different ion channels. In the *bc* plane, NHI exhibits a two-dimensional pore system characterized by channels that extend in both the *b* and *c* directions. The alumininosilicate structure of NHI is formed by connecting SiO_4 and AlO_4 tetrahedra to the framework using 4-, 6- and 8-membered rings in the *ab* plane, and 6-membered rings in the *ac* plane.[27] The bigger channels along the *c* direction allow tiny ions or molecules to readily pass through 8-membered rings, whereas the smaller channels along the *b* direction have narrow openings consisting of 6-membered rings. All water molecules are organized into wider channels, facilitating their straightforward entry or exit from the open structure.

ANA and CAN zeolite characterization

XRD patterns of the successfully produced zeolites are depicted in Fig. 2a. XRD pattern of ANA displays distinct peaks at 2θ 15.98, 25.94 and 30.72°, which are typical for ANA zeolite, as reported by Azizi *et al.*[28] The highest dif-

fraction peak intensity for CAN is observed at 2θ 27.44°. Additionally, at a concentration of 2.5 M, characteristic peaks for NHI are present at 2θ 10.72, 11.62, 20.17, 26.13 and 30.13°. The observed XRD patterns for ANA, CAN and NHI closely resemble the patterns reported for these zeolite frameworks in the IZA database. Moreover, Table III presents the computed lattice parameters for ANA and CAN.

TABLE III. Calculation result of lattice parameters of synthetic zeolites at 1.2 and 5 M of NaOH (ANA and CAN)

Lattice constant	ANA (P1)	CAN (P3a)
a / Å	13.7280	12.7558
b / Å	13.7280	12.7558
c / Å	13.7220	5.1985
α / °	90	90
β / °	90	90
γ / °	90	120
Cell volume, Å^3	2586.02	749.423
Cell density, g/cm^3	2.267	2.440
Crystal system	Tetragonal	Hexagonal

The XRD results of zeolite synthesis with varying the duration of reaction are shown in Fig. 2b. The results suggest that variations in the duration of reaction, specifically 12, 24 and 72 h, have a negligible effect on the characteristics of the zeolites produced. Synthesis at the same concentration (5 M of NaOH) with different reaction times yields the same type of zeolite, CAN. The primary difference observed is in the percentage of zeolite crystallinity. For example, the XRD pattern at 12 h of reaction time shows a magnetite peak at 2θ 35°, indicating incomplete dissolution during the reaction. In contrast, comparing the overall peak intensities for the three reaction times reveals that longer reaction times result in higher and sharper peaks, which indicates that the crystallinity of the resulting zeolite is better (see Table II).

Fig. 2c displays the FTIR spectra of the successfully produced zeolites (ANA and CAN). The results show spectral bands consistent with aluminosilicate materials. Both ANA and CAN exhibit spectra typical of zeolites. O–H groups from water in the zeolite framework are responsible for the absorption bands observed at 3600 and 1630 cm^{-1}. The asymmetric stretching vibrations of T–O tetrahedra (T = Al, Si) are represented by the band around 950 cm^{-1}, whereas the symmetric stretching vibrations of T–O are represented by the region between 720 and 650 cm^{-1}. The spectral around 460 cm^{-1} corresponds to the bending vibration of T–O–T.[11,24]

ANA zeolite has distinctive spectral characteristics below 650 cm^{-1}, corresponding to double-ring vibrations within its structure.[29] In the case of CAN, the area between 700 and 500 cm^{-1} is made up of a triplet band (676, 622 and 565

cm^{-1}), which shows the vibrations of the 4-, 6- and 12-membered rings and is related to the unit cell parameters.[13] The features of zeolite CAN are also shown by the presence of weak intensity peaks at 1393, 1425 and 1462 cm^{-1}, which show the presence of CO_3 groups.[30] These elements can be found in CAN pores that are obtained from high-concentration solutions. Furthermore, the characteristic features of NHI are evidenced by the presence of spectra in the mid-range of 3200 and 3500 cm^{-1}, signaling the presence of water.[31] Nepheline is an intermediate phase in the synthesis of cancrinite, which is present as an impurity.[30]

Fig. 2d shows the isotherms for adsorption and desorption of ANA and CAN. Both categories of zeolites present a type IV adsorption isotherm. This property is typical of mesoporous materials. The ANA and CAN samples exhibit H1 hysteresis loops, which suggest the presence of uniform pore dimensions. However, ANA also slightly approaches type H4, which has a combination of mesoporous and microporous structures with open ends. Table IV shows the BET surface areas and total pore volumes obtained from the synthesis of zeolites using Toraja natural minerals, specifically ANA and CAN.

TABLE IV. Surface area and porosity of ANA and CAN

Material	BET surface area, m^2/g	Total pore volume, cm^3/g	Average pore size, nm
ANA (P1)	75.49	0.19	4.97
CAN (P3a)	43.03	0.07	6.84

The SEM images of the synthesized samples at various NaOH concentrations (formation duration of 72 h, temperature of 170 °C) are shown in Fig. 3. Fig. 3a shows zeolite ANA synthesized at a NaOH concentration of 1.2 M, exhibiting an isometric trapezoidal crystal morphology. The observed crystals have an average maximum length of 24 μm. A similar trapezohedral morphology was reported by Novembre and Gimeno[11] with crystal sizes of 25 μm. Furthermore, Amin *et al.*[10] achieved a comparable result by synthesizing ANA from Mesawa feldspar with crystal dimensions ranging from 13 to 24 μm. Despite the presence of impurities, most likely from residual montmorillonite or insoluble silica gel, the crystals have well-defined facets. The low concentration of NaOH means that not all raw materials can be dissolved, so the crystallinity of the ANA obtained is also low.

Fig. 3b presents a zeolite CAN combination with an NHI phase mixture produced using a 2.5 M NaOH concentration. The result reveals needle-like rod-shaped CAN crystals, characteristic of the hexagonal cancrinite crystal structure.[32] The CAN crystals are interspersed with shorter and larger rod-shaped NHI crystals.[33] Synthesis at this concentration achieved good crystallinity, with the starting material fully dissolved in NaOH, although two crystal phases are present. Fig. 3c depicts CAN with a single mineral phase synthesized at a NaOH

concentration of 5 M. The resulting crystals are rod-shaped with an average length of 1.66 μm. At this concentration, the crystal morphology is uniform, but agglomeration occurs, causing the crystals to adhere to each other, making some crystal parts difficult to observe.

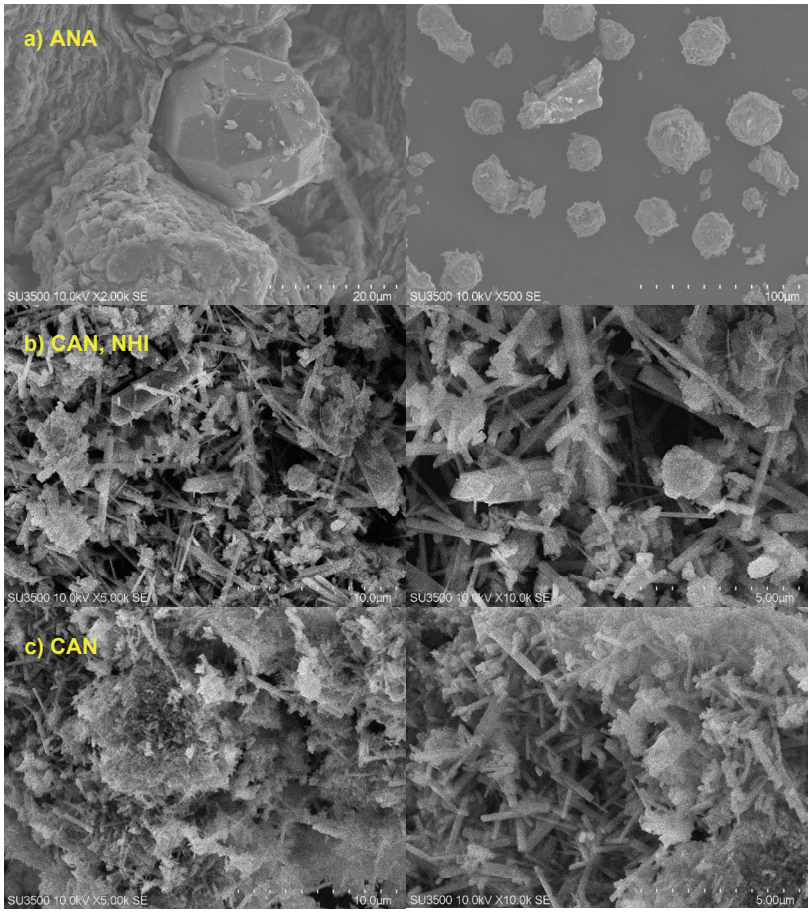

Fig. 3. SEM Illustration of a zeolite samples obtained from the Toraja natural mineral, shown at various levels of magnifications.

The conversion of natural Toraja minerals into zeolites involves the dissolution of montmorillonite, quartz, and feldspar, followed by zeolite crystallization, as described in chemical reaction Eqs. (1)–(5). Amaya *et al.*[34] reported that montmorillonite undergoes significant silicon dissolution under basic conditions. Similarly, quartz readily dissolves in alkaline solutions. However, feldspar dissolution occurs in three distinct steps: 1) ion exchange between alkali metal cat-

ions (M^+ = K, Na, or Ca) and H^+; 2) breaking of Al–O bonds; 3) hydrolysis of Si–O–Si bonds, resulting in the release of M^+, $Al(OH)_4^-$ and $H_2SiO_4^{2-}$:[24]

Mineral dissolution:

$$Al_2H_2O_{12}Si_4 + 10OH^- + 2H_2O \rightarrow 2[Al(OH)_4]^- + 4[H_2SiO_4]^{2-} \quad (1)$$

$$SiO_2 + 2OH^- \rightarrow [H_2SiO_4]^{2-} \quad (2)$$

$$NaAlSi_3O_8 + 6OH^- + 2H_2O \rightarrow [Al(OH)_4]^- + 3[H_2SiO_4]^{2-} + Na^+ \quad (3)$$

Zeolite crystallization:

$$Na^+ + Al(OH)_4^- + 2H_2SiO_4^{2-} \rightarrow NaAlSi_2O_6{\cdot}H_2O + 4OH^- + H_2O \quad (4)$$

$$8Na^+ + 6Al(OH)_4^- + 6H_2SiO_4^{2-} \rightarrow$$

$$Na_8Al_6Si_6O_{24}(OH)_2{\cdot}2H_2O + 2SiO_8^{2-} + 12H_2O + 10OH^- \quad (5)$$

At lower alkali concentrations, the availability of dissolved silica ($H_2SiO_4^{2-}$) and alumina ($Al(OH)_4^-$) is limited, favoring the formation of stable analcime (ANA) zeolite. Conversely, at higher alkali concentrations, the increased dissolution rate of minerals results in higher concentrations of $Al(OH)_4^-$ and $H_2SiO_4^{2-}$ in solution.[35] Additionally, the elevated concentration of OH^- can react with atmospheric CO_2, forming CO_3^{2-}.[36] Under these conditions, the zeolite framework is more likely to incorporate larger anions such as CO_3^{2-} or OH^-, facilitating the crystallization of CAN, which accommodates these anions within its channels.[37]

The quantitative investigation of ANA and CAN using the EDX technique indicates that the ratio of Na to Al is below 1. On the other hand, the ratio of Si/Al tends towards the theoretical optimal value, as shown in Fig. 4. The concentration of Al^{3+} rises in correlation with the increase in NaOH concentration, indicating that the production of CAN needs a more significant amount of Al^{3+} than the production of ANA. At a concentration of 1.2 M, the Al^{3+} concentration is too low to form a hydroxyl structure in CAN. As a result, the tetragonal trisoctahedral ANA is formed.

CONCLUSION

Toraja natural minerals were successfully used in an alkaline solution to synthesise ANA and CAN zeolites. These minerals contain montmorillonite, feldspar and quartz, which are recognized as aluminosilicate minerals, making them suitable as raw materials for zeolite synthesis. The provided SiO_2/Al_2O_3 ratio was appropriate, negating the need for additional aluminosilicate sources. The yields of the synthesized zeolites ANA and CAN were 42.25 and 45.60 %, respectively. Zeolite formation design can be regulated by choosing the suitable alkali content and reaction duration. The trapezohedral morphology of ANA-type zeolites is characterised by uniform crystals and a surface area of 75.49 m^2/g. By comparison, CAN-type zeolites exhibit a cylindrical shape with a surface area of

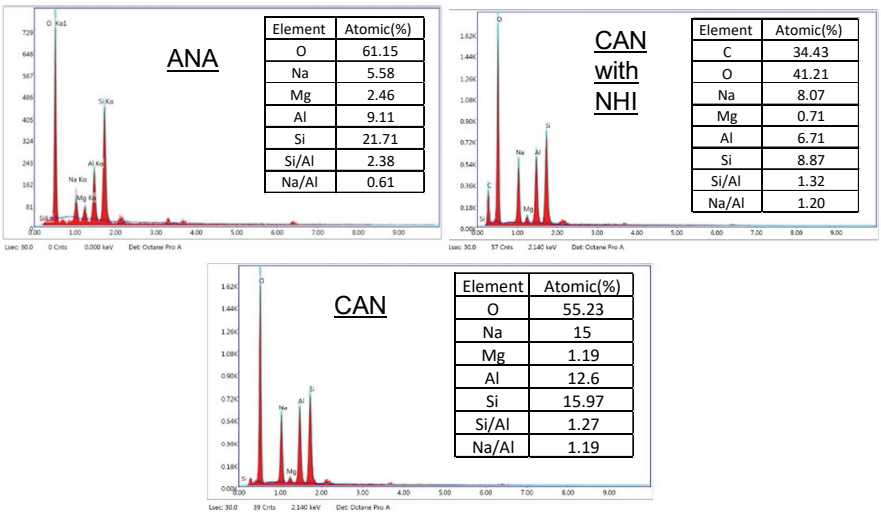

Fig. 4. EDX Spectra and chemical composition analysis of zeolites obtained from synthesis using Toraja natural minerals.

43.03 m^2/g. The mechanism for converting Toraja natural mineral powder into zeolites is driven by dissolution and precipitation processes, commonly referred to as recrystallization. The study proposes that Toraja natural minerals include secondary functional units of zeolites, namely 4-, 6- and 8- membered rings.

Acknowledgements. The author is grateful to Hasanuddin University grant for the 2024 fiscal based on Rector's Decree No./01181UN4.1/KEP/2024 January 29, 2024 and contract agreement number: 00309/UN4.22/PT.01.03/2024 January 30, 2024.

И З В О Д

СИНТЕЗА И КАРАКТЕРИЗАЦИЈА ЗЕОЛИТА ДОБИЈЕНОГ ОД ТОРАЈА ПРИРОДНОГ МОНТМОРИОНИТА

PAULINA TABA[1], ST. FAUZIAH[1], HASNAH NATZIR[1], NUNUK H. SOEKAMTO[1], ROSALIA S. SARUNGALLO[2], NUR W. NAHRU[1], YULI ASTUTI[1] и IDA I. AMIN[3]

[1]Department of Chemistry, Faculty of Science, Hasanuddin University, Indonesia, [2]Chemical Engineering, Kristen Indonesia Paulus Makassar University, Indonesia u [3]Department of Technological of Metallurgy Extraction, Faculty of Vocational, Hasanuddin University, Indonesia

Зеолити су алтернативни материјали за третман отпада који садржи тешке метале. Синтетичке зеолите карактерише изузетна чистоћа и униформност честица, па је великом броју истраживача од интереса унапређење њихове синтезе, укључујући и коришћење природних минерала. Циљ овог рада је хидротермална синтеза зеолита при којој се као извор алумосиликата користе Тораја природни минерали. Хидротермална реакција Тораја природних минерала, који се доминантно састоје од монтморионита, са различитим концентрацијама NaOH резултовала је формирањем аналцим (ANA) и канкринит (CAN) зеолита. Испитивано је и реакционо време формирања зеолита. Резултати дифракције X-зрачења су показали да ANA и CAN имају тетрагоналну и хексагоналну кристалну структуру, редом. EDX анализом је одређен моларни однос Si/Al за ANA 2,40 и за

CAN 1,27. У инфрацрвеним спектрима су детектоване апсорпционе траке у спектралној области од 700–400 cm^{-1}, чији интензитет расте са порастом NaOH концентрације. ANA зеолит показује карактеристичне траке испод 650 cm^{-1}, које потичу од вибрација двоструких прстенова у његовој структури. Додатно, триплетне траке на 676, 622 и 565 cm^{-1} у синтетисаном материјалима потврђују карактеристичну структуру канкринита. СЕМ анализа је показала кристале аналицима трапезоидног облика чија је средња величина 24 μm и кристале канкринита у облику шипки дужине 1,66 μm. Тораја минерали, посебно монтморионит, садрже секундарне изграђивачке јединице које фомриају различите зеолите у зависности од реакционих услова.

(Примљено 12. октобра, ревидирано 8. новембра 2024, прихваћено 5. фебруара 2025)

REFERENCES

1. E. Kuldeyev, M. Seitzhanova, S. Tanirbergenova, K. Tazhu, E. Doszhanov, Z. Mansurov, S. Azat, R. Nurlybaev, R. Berndtsson, *Water* **15** (2023) 2215 (https://doi.org/10.3390/w15122215)
2. M. Hong, L. Yu, Y. Wang, J. Zhang, Z. Chen, L. Dong, Q. Zan, R. Li, *Chem. Eng. J.* **359** (2019) 363 (https://doi.org/10.1016/j.cej.2018.11.087)
3. N. Dhani, A. Gasruddin, H. Hartini, L. Baride, *Civ. Eng. J.* **7** (2021) 40 (https://doi.org/10.28991/cej-2021-03091635)
4. B. Jha, D. N. Singh, *ChemInform* **43** (2012) (http://dx.doi.org/10.1002/chin.201225227)
5. Y. D. Ngapa, S. Sugiarti, Z. Abidin, *Indones. J. Chem.* **16** (2018) 138 (https://doi.org/10.22146/ijc.21156)
6. S. Gu, J. Kang, T. Lee, J. Shim, J.-W. Choi, D. J. Suh, H. Lee, C. Yoo, H. Baik, J. Choi, J.-M. Ha, *Chem. Eng. J.* **457** (2023) 141057 (https://doi.org/10.1016/j.cej.2022.141057)
7. W. Kartawa, K. D. Kusumah, *J. Geol. dan Sumberd. Miner.* **16** (2006) 371 (https://jgsm.geologi.esdm.go.id/index.php/JGSM/article/view/377/330) (in Indonesian)
8. D. W. Kurniawidi, S. Alaa, S. Mulyani, S. Rahayu, *ORBITA J. Pendidik. dan Ilmu Fis.* **7** (2021) 313 (https://doi.org/10.31764/orbita.v7i2.6010) (in Indonesian)
9. G. Ke, H. Shen, P. Yang, *Materials (Basel)* **12** (2019) 3895 (https://doi.org/10.3390/ma12233895)
10. I. I. Amin, A. W. Wahab, R. R. Mukti, P. Taba, *Appl. Nanosci.* **13** (2023) 5389 (https://doi.org/10.1007/s13204-022-02756-4)
11. D. Novembre, D. Gimeno, *Sci. Rep.* **11** (2021) 13373 (https://doi.org/10.1038/s41598-021-92862-0)
12. I. V. Joseph, L. Tosheva, G. Miller, A. M. Doyle, *Materials (Basel)* **14** (2021) 3738 (https://doi.org/10.3390/ma14133738)
13. L. Teng, X. Jin, Y. Bu, J. Ma, Q. Liu, J. Yang, W. Liu, L. Yao, *J. Environ. Chem. Eng.* **10** (2022) 108369 (https://doi.org/10.1016/j.jece.2022.108369)
14. H. Wu, X. Wang, W. Su, *Vibroeng. Proc.* **51** (2023) 114 (https://doi.org/10.21595/vp.2023.23545)
15. N. Sobuś, I. Czekaj, V. Diichuk, I. M. Kobasa, *Tech. Trans.* **117** (2020) 1 (https://doi.org/10.37705/TechTrans/e2020043)
16. R. Vigil de la Villa Mencía, E. Goiti, M. Ocejo, R. G. Giménez, *Microporous Mesoporous Mater.* **293** (2020) 109817 (https://doi.org/10.1016/j.micromeso.2019.109817)
17. M. Esaifan, L. N. Warr, G. Grathoff, T. Meyer, M.-T. Schafmeister, A. Kruth, H. Testrich, *Minerals* **9** (2019) 484 (https://doi.org/10.3390/min9080484)

18. M. Abdul-Moneim, A. A. Abdelmoneim, A. A. Geies, S. O. Farghaly, *Assiut Univ. Bull. Environ. Res.* **21.1** (2018) 23 (https://doi.org/10.21608/auber.2018.133200)
19. A. Z. Efendy, N. Herawati, A. Alimin, *Chemica: Jurnal Ilmiah Kimia dan Pendidikan Kimia* **17** (2016) (https://ojs.unm.ac.id/chemica/article/view/4568) (in Indonesian)
20. H. Liu, T. Shen, W. Wang, T. Li, Y. Yue, X. Bao, *Appl. Clay Sci.* **115** (2015) 201 (https://doi.org/10.1016/j.clay.2015.07.040)
21. M. Al Kausor, S. Sen Gupta, K. G. Bhattacharyya, D. Chakrabortty, *Inorg. Chem. Commun.* **143** (2022) 109686 (https://doi.org/10.1016/j.inoche.2022.109686)
22. Z. Danková, A. Mockovčiaková, S. Dolinská, *Desalin. Water Treat.* **52** (2014) 5462 (https://doi.org/10.1080/19443994.2013.814006)
23. T. Chellapandi, G. Madhumitha, *Mol. Divers.* **26** (2022) 2311 (https://doi.org/10.1007/s11030-021-10322-3)
24. X. Ma, J. Yang, H. Ma, C. Liu, P. Zhang, *Microporous Mesoporous Mater.* **201** (2015) 134 (https://doi.org/10.1016/j.micromeso.2014.09.019)
25. Y. Shen, P. Zhao, Q. Shao, *Microporous Mesoporous Mater.* **188** (2014) 46 (https://doi.org/10.1016/j.micromeso.2014.01.005)
26. E. Słaby, *Acta Geol. Pol.* **49** (1999) 25 (https://geojournals.pgi.gov.pl/agp/article/view/10126/8654)
27. S. Hansen, L. Fälth, *Zeolites* **2** (1982) 162 (https://doi.org/10.1016/S0144-2449(82)80046-8)
28. S. N. Azizi, S. Ghasemi, N. S. Gilani, *Chin. J. Catal.* **35** (2014) 383 https://doi.org/10.1016/S1872-2067(14)60002-4
29. P. G. G. Saha, *Trans. Indian Ceram. Soc.* **36** (1977) 99 (https://doi.org/10.1080/0371750X.1977.10840649)
30. S. M. Seo, D. Kim, D. Kim, J.-H. Kim, Y. J. Lee, K.-M. Roh, I.-M. Kang, *J. Porous Mater.* **25** (2018) 1561 (https://doi.org/10.1007/s10934-018-0569-4)
31. A. G. Simakin, T. P. Salova, V. O. Zavel'skii, *Geochemistry Int.* **46** (2008) 622
32. F. A. C. M. Passos, D. C. Castro, K. K. Ferreira, K. M. A. Simões, L. C. Bertolino, C. N. Barbato, F. M. S. Garrido, A. A. S. Felix, F. A. N. G. Silva, in *Characterization of Minerals, Metals, and Materials 2017*, Conference proceedings, Springer, Cham, 2017, pp. 279–288 (https://doi.org/10.1007/978-3-319-51382-9_31)
33. K. Rouchalová, D. Rouchalová, V. Čablík, D. Matýsek, *Materials (Basel)* **17** (2024) 269 (https://doi.org/10.3390/ma17010269)
34. T. Amaya, M. Shimojo, H. Fujihara, K. Yokoyama, *MRS Online Proc. Lib.* **556** (1999) 655 (https://doi.org/10.1557/PROC-556-655)
35. M. Osacký, H. Pálková, P. Hudec, A. Czímerová, D. Galusková, M. Vítková, *Microporous Mesoporous Mater.* **294** (2020) 20 (https://doi.org/10.1016/j.micromeso.2019.109852)
36. Q. Liu, A. Navrotsky, C. F. Jove-Colon, F. Bonhomme, *Microporous Mesoporous Mater.* **98** (2007) 227 (https://doi.org/10.1016/j.micromeso.2006.09.008)
37. V. Wernert, O. Schaef, L. Aloui, C. Chassigneux, F. Ayari, D. Ben Hassen Chehimi, R. Denoyel, *Microporous Mesoporous Mater.* **301** (2020) 110209 (https://doi.org/10.1016/j.micromeso.2020.110209).

Journal of the Serbian Chemical Society
JSCS@tmf.bg.ac.rs • www.shd.org.rs/JSCS
J. Serb. Chem. Soc. *90* (6) 767–780 (2025)
JSCS–5419
Original scientific paper
Published 24 June, 2025

Catalytic performance of palladium/degraded chitosan for acetylene selective hydrogenation

SI-YE TANG[1]*, XIN-XIANG CAO[1]**, TONG-TONG DI[2] and XIN-YU LI[3]

[1]College of Chemistry and Chemical Engineering, Luoyang Normal University, Luoyang 471934, China, [2]School of Chemical Engineering, Northwest University, Xian 710069, China and [3]School of Chemical Engineering, Zhengzhou University, Zhengzhou 450001, China

(Received 19 December 2024, revised 31 January, accepted 27 April 2025)

Abstract: The aim of this paper was to investigate the catalytic properties of palladium supported on chitosan catalysts. The effect of primitive chitosan and degraded chitosan on catalytic performance was compared. The structure, morphology, metal content and properties of the catalysts were characterized by Fourier transform infrared spectroscopy (FTIR), scanning electron microscopy (SEM), inductively coupled plasma spectrometry (ICP), X-ray diffraction (XRD), Brunauer–Emmett–Teller (BET) method and X-ray photoelectron spectroscopy (XPS). The results showed that the catalytic performance of Pd/degraded chitosan was better than that of Pd/chitosan at a certain Pd load. Pd/degraded chitosan (degradation 4 h) catalyst exhibited excellent catalytic performance and stability. The acetylene conversion and ethylene selectivity, respectively, achieved 100 and 91 %. During 13.5 h, the acetylene conversion maintained 100 % and the ethylene selectivity decreased slightly from 88 to 71 %. Based on this study, it was demonstrated that Pd was successfully coordinated with chitosan; after degradation, the chitosan particles became smaller and had larger surface areas; these were conducive to improve the catalytic performance of Pd/degraded chitosan. Pd/degraded chitosan also had high selectivity at high conversion, greatly improving the characteristics of low selectivity at high conversion of traditional Pd-based catalysts.

Keywords: chitosan; conversion; degradation; selectivity.

INTRODUCTION

A significant proportion of ethylene is produced from naphtha cracking.[1] This process makes ethylene to be contaminated with 0.5–2 % of acetylene, which can poison the Ziegler–Natta catalyst used for downstream ethylene polymerization.[1] Selective hydrogenation of small amounts of acetylene in ethylene

* Corresponding authors. E-mail: (*)tsy6611@163.com; (**)xiangzi827@163.com
https://doi.org/10.2298/JSC241219031T

rich feedstocks is an important industrial target. Namely, acetylene is effectively removed from ethylene via hydrogenation to ethylene. At the same time, substantial hydrogenation of ethylene and over-hydrogenation of acetylene to undesirable ethane are avoided. In order to avoid poisoning of the catalyst in the ethylene polymerization, acetylene concentration must be reduced to a level less than 5 ppm.[1] So it is necessary to seek the catalysts with both high activity for acetylene conversion and high selectivity for ethylene. The traditional industrial catalysts are Pd-based systems, which usually show a poor selectivity at high conversion of acetylene.[1,2] How to improve the selectivity of Pd-based catalysts has always been the focus of researchers.

It is well known that catalyst support strongly influences the catalytic performance of Pd.[3–6] Changing support is one of the effective methods to improve the catalytic performance of a catalyst. In industry, Al_2O_3, SiO_2 and carbon are commonly used as supports of Pd-based catalysts for acetylene selective hydrogenation.[7–9] As a biodegradable materials, polysaccharides have gained lot of attention in the synthesis of catalysts.[10] These biodegradable resources can decrease the utilization of non-renewable materials and minimize the environmental pollution. Chitosan (CS) is classified as polysaccharides, obtained from chitin which is the second most abundant natural polymer present on the earth.[11] Duo to the hydroxyl and amino groups, CS has strong affinity for metal ions and high sorption capacities for catalytic metals such as palladium, copper, platinum. It has been shown to be a very promising support.[12,13] Researchers used Pd supported on CS (or CS derivatives) as catalysts for oxidation reactions, hydrogenation reactions, allylic substitution reactions, carbonylation reactions, Suzuki and Heck reactions.[12] For the hydrogenation reaction, Jin used silica-supported CS––Pd catalysts for the hydrogenation of nitrobenzene, 1-hexene, acrylic acid, chloronitrobenzene and phenol to aniline, hexane, propionic acid, chloroaniline and cyclohexanone, respectively.[12] However, Pd/CS composites have not yet been used as catalysts for acetylene selective hydrogenation in the available literature so far.

In this work, we utilized CS to prepare Pd-based catalysts. The catalytic properties of the obtained catalysts were tested by selective hydrogenation of acetylene. In addition, the stability of the resultant catalyst was also studied. Simultaneously, the obtained catalysts were characterized by X-ray diffraction (XRD), scanning electron microscopy (SEM), inductively coupled plasma spectrometry (ICP), Brunauer–Emmett–Teller (BET) method, Fourier transform infrared spectroscopy (FTIR) and X-ray photoelectron spectroscopy (XPS).

EXPERIMENTAL

Materials

CS (pharmaceutical grade, deacetylation degree: 80–95 %) was purchased from Sinopharm Chemical Reagent Co., Ltd. (Shanghai, China). All the other reagents were purchased

from Damao Chemical Reagent Factory (Tianjin, China). They were of analytical grade and were used without further purification.

Preparation of the degraded CS

2 g of CS was put into a 250 mL round bottom flask. 100 mL of 2 % acetic acid aqueous solution was added to the flask. The suspension was then magnetically stirred at 30 ℃ for 4 h to ensure CS complete dissolution. 8 mL of 30 % H_2O_2 aqueous solution was added to the CS acetic acid solution. The above mixed solution reacted at 50 ℃ for 6 h under stirring.

Then the pH of reaction mixture was adjusted to be neutral using 1 M NaOH aqueous solution. The product was separated by centrifugation (10000 rpm for 5 min) and washed three times with distilled water and anhydrous ethanol, respectively. Then the product was dried in an oven at 40 ℃ for 12 h. The degraded CS sample was obtained. The degradation time was set to 0.5, 1, 2, 4 and 6 h. The corresponding CS samples were labeled as degraded CS (0.5 h), degraded CS (1 h), degraded CS (2 h), degraded CS (4 h) and degraded CS (6 h), respectively.

Measurement of intrinsic viscosity ([η]) of CS

The value of [η] can reflect the molecular weight of a polymer. The smaller the [η], the smaller the molecular weight. A certain amount of CS sample was dissolved into 20 mL of formic acid. The [η] of CS sample was determined using Obblehode viscometry. The values of [η] were calculated according to the literature method.[14]

Preparation of Pd/CS and Pd/degraded CS

0.6 g of CS (or degraded CS) was put into a 250 mL round bottom flask. 100 mL of 2 % acetic acid aqueous solution was added to the flask. The suspension was then magnetically stirred at 50 ℃ until the CS (or degraded CS) was completely dissolved. A certain volume of $PdCl_2$ hydrochloric acid solution was added dropwise to the CS (or degraded CS) solution under stirring. The mixture reacted at 60 ℃ for 2 h.

Then the reaction mixture was cooled and adjusted to be neutral using 1 M NaOH aqueous solution. The product was separated by centrifugation (10000 rpm for 5 min) and washed three times with distilled water. Then the product was dried at 40 ℃ to constant weight. The dried sample was Pd/CS (or Pd/degraded CS) catalyst.

Catalytic performance experiment

Pretreatment before reaction. 30–31 mg of catalyst was put into a quartz tube reactor (4 mm inner diameter). The quartz tube reactor was fixed in an oven with a programmed temperature controller. The catalyst was reduced in situ for 2 h under a flow of H_2/Ar mixture at 130 ℃ by heating from room temperature using a heating rate of 5 ℃ min^{-1}. The volume ratio of H_2 to Ar was 1 to 3. Then the reactor was cooled down to the reaction temperature under the protection of Ar gas.

Selective hydrogenation of acetylene. Ar, H_2 and feed gas mixture of 94.95 % C_2H_4, 5.05 % C_2H_2 were continuously introduced into the quartz tube reactor. The total flow rate of Ar, H_2, C_2H_4 and C_2H_2 mixture was 30 mL min^{-1} and the volume ratio of H_2 to C_2H_2 was 20 to 1. The total gas hourly space velocity (*GHSV*) was 60000 mL h^{-1} g^{-1}. All gas flows in the reaction were controlled with mass flow controllers. The gas products from the reactor outlet were analyzed three times at each reaction temperature by an online gas chromatography (GC--2020, Tengzhou Zhongke spectrum analysis instrument Co. Ltd, Shandong, China) equipped with a flame ionization detector and a 30 m×0.32 mm (i.d.)×1.50 μm XP-Plot capillary column (column box temperature:100 ℃; detector temperature: 200 ℃). The analysis data of

the gas chromatography was collected using a PC work-station. These analysis data that included the amount of C_2H_2, C_2H_4 and C_2H_6 in the gas products from the reactor outlet were used to calculate the conversion and selectivity of the catalyst. Acetylene conversion and selectivity to ethylene were calculated as follows:[1,15]

$$C_2H_2 \text{ conversion} = 100\frac{C_2H_2(\text{in feed}) - C_2H_2(\text{in products})}{C_2H_2(\text{in feed})} \quad (1)$$

$$C_2H_4 \text{ selectivity} = 100(1 - \frac{C_2H_6(\text{in products}) - C_2H_6(\text{in feed})}{C_2H_2(\text{in feed}) - C_2H_2(\text{in products})}) \quad (2)$$

Characterization

The actual metal load of the different catalysts was measured using ICP (Aglient 7800, USA). The structures of samples were investigated by FTIR (Invenio S, Germany) using KBr disk technique. Each spectrum of the samples was acquired by accumulation of 27 scans with a resolution of 4 cm^{-1}. Morphology of samples was characterized by SEM (Carl Zeiss Sigma 500, Germany). The compositions' phases of the as-prepared materials were identified by a XRD (Bruker D8 Advances, Germany) equipped with CuKα radiation (λ = 1.5418 Å) and operated at 40 kV and 40 mA with a 5° min^{-1} scan rate. The scanning angular range of 2θ was performed from 5 to 90°. The surface area measurements of catalysts were conducted according to the BET method at –196 °C (Asap 2020 Plus HD88, USA). The samples were pretreated at 120 °C for 4 h. The total pore volume was evaluated by single point pore volume at a relative pressure of 0.99. The binding energy (*BE*) and the chemical state of elements were determined by XPS (K-Alpha, UK). Binding energies were calibrated using the C_{1s} peak (*BE* = 284.8 eV) as standard.

Before XRD and XPS analyses, the catalysts were reduced in situ for 2 h under a flow of H_2/Ar mixture at 130 ℃.

RESULTS AND DISCUSSION

The [η] of CS sample

The values of [η] are listed in Table I. As can be seen from Table I, the values of [η] decreased with degradation time. This indicates that the molecular chain of CS was broken and the molecular weight of CS was decreased.

TABLE I. The [η] of CS samples at different degradation time

Degradation time, h	0.0	0.5	1.0	2.0	4.0	6.0
[η] / mL g^{-1}	513.4	202.0	132.5	50.5	14.0	2.7

XRD analysis

XRD patterns of CS, degraded CS (4 h), 0.2 % Pd/CS and 0.2 % Pd/degraded CS (4 h) are shown in Fig. 1. 0.2 % indicates that the nominal load of the Pd is 0.2 mass %.

As shown in Fig. 1, the pattern of CS shows a broader and weaker characteristic peak at 2θ 24.0°. It indicates that the degree of crystallinity of CS was very low. A strong new characteristic peak appeared at 2θ 20.1° after degrading for 4 h. This suggests that the crystallinity of CS increased after degradation.

Crystallinity increase supports the theory that H_2O_2 solution penetrates and degrades the amorphous zone first.[16]

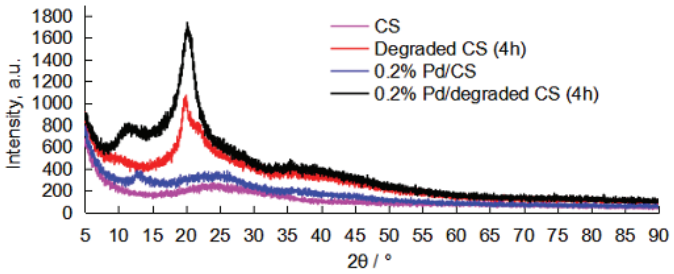

Fig. 1. XRD of CS, degraded CS (4 h), 0.2 % Pd/CS and 0.2 % Pd/degraded CS (4 h).

For 0.2 % Pd/CS and 0.2 % Pd/degraded CS (4 h) catalysts, due to the coordination of CS and degraded CS with Pd, both catalysts showed new absorption peaks at 2θ 12.8 and 11.7°, respectively.

Furthermore, no characteristic peak of Pd is observed in the XRD patterns of 0.2 % Pd/CS and 0.2 % Pd/degraded CS (4 h). This indicates that Pd species were amorphous and were uniformly dispersed. Perhaps the content of Pd was too low to be measured.

SEM analysis

Fig. 2 shows the SEM images of CS (Fig. 2a) and degraded CS (4 h) (Fig. 2b).

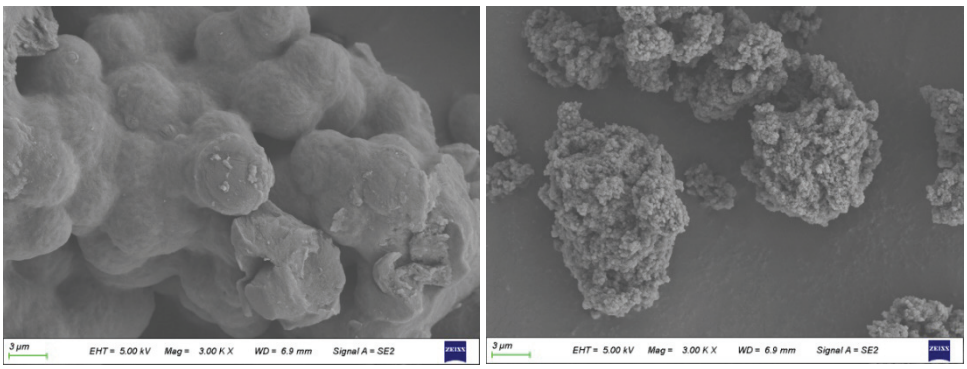

(a) (b)

Fig. 2. SEM image of: a) CS; b) degraded CS (4 h).

It can be seen that CS and degraded CS all presented uniform spherical particle and all had rough surface. However, the particle size of degraded CS was much smaller than CS. This was due to degradation of CS. Degradation made the molecular chain of CS break into small segments. The small particle size had

larger surface area. This was conducive to the dispersion of Pd and coordination of Pd with CS as well as improving catalytic performance.

ICP analysis

Actual load and the nominal load of Pd in Pd/CS and Pd/degraded CS (4 h) analyzed by ICP are summarized in Table II. It can be seen that the actual Pd load of Pd/degraded CS (4 h) was higher than that of Pd/CS. The reason was that the size of degraded CS was smaller than that of CS. Degraded CS with small size bound more readily with Pd. These results were in good agreement with the SEM results.

TABLE II. The Pd load, BET and total pore volume of catalysts

Catalyst	Nominal load of Pd, %	Actual load of Pd, %	Actual load of Pd after 13.5 h, %	BET surface area, m^2/g	Total pore volume, m^3/g
Pd/CS	0.20	0.13	0.13	2.14	0.017
Pd/degraded CS (4 h)	0.20	0.20	0.20	145.89	0.78

From Table II, the content of Pd was unchanged after reacting for 13.5 h. This demonstrates that the mass loss of catalyst was zero in the gas-solid phase catalytic reaction.

BET analysis

The BET surface areas of the samples are listed in Table II. The BET surface area of Pd/CS and Pd/degraded CS (4 h) are 2.14 and 145.89 m^2/g, respectively. The total pore volume of Pd/CS and Pd/degraded CS (4 h) are 0.017 and 0.78 cm^3/g, respectively. It can be seen that the surface area and pore volume of Pd/degraded CS (4 h) are higher than that of Pd/CS. The values of BET surface area confirmed that small particle had large surface area. This was consistent with SEM results. The large surface area was conducive to the dispersion and adsorption of the active metal as well as improving the catalytic performance of catalysts.

FTIR analysis

FTIR spectra of different samples are shown in Fig. 3.

In the FTIR spectrum of CS, the characteristic broad peak at 3374 cm^{-1} was considered as the stretching vibrations of O–H and N–H in CS.[17–19] The peak observed at 2876 cm^{-1} was ascribed to C–H stretching vibration.[19–21] The weak peak appeared at 1656 cm^{-1} was assigned to the amide C=O stretching.[18,22,23] The weak peak appeared at 1598 cm^{-1} was assigned to the bending band of N–H.[18,23] As shown in the FTIR spectrum of CS, the absorption peak near 1381 cm^{-1} was assigned to deformational vibrations of the –OH group.[19,20] The CS

characteristic band at 1078 cm^{-1} was ascribed to asymmetric stretching vibration of –C–O.[18,23]

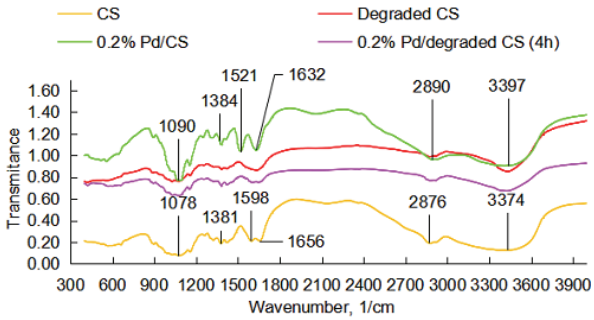

Fig. 3. FTIR spectra of CS, degraded CS (4 h), 0.2 % Pd/CS and 0.2 % Pd/degraded CS (4 h).

Compared with the CS, degraded CS just had some changes in the FTIR spectra, that is, the absorption of O – H and N–H shifted to 3435 cm^{-1} and the absorption of C=O slightly shifted to 1634 cm^{-1}. The absorption peaks at 2876, 1381, 1078 cm^{-1} were almost unchanged. The absorption of of N–H at 1598 cm^{-1} disappeared. These observations proved CS molecule was degraded. The breakage of the CS molecular chains resulted in its structural change. These results indicate that some CS molecular chains were broken from C–NH and C–OH.

Comparison of CS FTIR spectrum with 0.2 % Pd/CS shows that introduction of Pd caused significant changes. The characteristic bands at 3374, 2876 and 1381 cm^{-1} from CS spectrum were also present after Pd loading, but increased slightly in intensity and shifted to 3397, 2890 and 1384 cm^{-1}. Simultaneously, the characteristic bands at 1656, 1598 and 1078 cm^{-1} from CS spectrum were also present after Pd species loading, but varied obviously in intensity and shifted to 1632, 1521 and 1090 cm^{-1}. Coordination of CS with Pd species results in substantial changes of the vibration frequencies.

However, the presence of Pd in degraded CS causes slightly changes in the shape of the FTIR spectra of degraded CS and 0.2 % Pd/degraded CS (4 h). In the FTIR spectrum of degraded CS, the absorb bands at 3435, 2874, 1635, 1387 and 1076 cm^{-1} were shifted to 3425, 2880, 1653, 1385 and 1079 cm^{-1}, respectively. These changes indicate that coordination of the degraded CS with Pd species occurred.

XPS analysis

As listed in Table III, the atomic concentrations of C_{1s}, N_{1s} and O_{1s} of CS are close to that of Pd/CS. However, the contents of C_{1s}, N_{1s} and O_{1s} of CS are different from that of Pd/degraded CS (4 h). The atomic concentration of C_{1s} increased from 65.57 to 79.38 %, while the atomic concentrations of N_{1s} and O_{1s}

decreased from 5.93 and 28.50 % to 1.18 and 19.42 %, respectively. This indicates that part of the CS molecular chains were broken from –OH and –NH during degradation, thus increasing the surface C atom content.

TABLE III. XPS data for Pd/CS, Pd/degraded CS (4 h)

Element	C_{1s}	N_{1s}	O_{1s}	Pd_{3d5}
Compound		CS		
Binding energy[a], eV	285.26	399.04	532.21	–
Atomic concentration, %	65.57	5.93	28.50	–
Compound		Pd/CS		
Binding energy, eV	284.80	399.57	532.87	337.19
Atomic concentration, %	65.11	6.18	28.66	0.05
Chemical state	C–C/C–H	C–N(H)	C–O(H)	Pd–O
Compound		Pd/degraded CS (4 h)		
Binding energy, eV	284.80	399.33	533.29	337.88
Atomic concentration, %	79.38	1.18	19.42	0.02
Chemical state	C–C/C–H	C–N(H)	C–O(H)	PdO*x*

[a]The binding energies were referenced to C_{1s} (284.8eV)

Comparing the XPS data of CS with Pd/CS and Pd/degraded CS (4 h), the binding energy of N_{1s} increased from 399.04 to 399.57 and 399.33 eV, respectively, which indicates that the coordination bonds have formed between Pd and amino group of CS. While the binding energy of O_{1s} rose from 532.21 to 532.87 and 533.29 eV, respectively, indicating that Pd was also coordinated to hydroxyl group of CS. These results were in good agreement with the FTIR results.

As displayed in Table III, the chemical states of Pd in Pd/CS and Pd/degraded CS were PdO and PdO*x*, respectively.

Catalyst performance test

Effect of the Pd load. Taking the degraded CS (6 h) as an example, the effect of Pd load on catalyst performance was studied. The conversion and the selectivity data over Pd/degraded CS (6 h) are shown in Fig. 4.

From Fig. 4a, the conversion enhanced as the temperature increased. The conversion of 0.3 and 0.2 % Pd can achieve 100 % at 150 and 170 °C, respectively. For 0.1 % Pd, acetylene was still not fully converted at 190 °C and the conversion was only 87 %.

In Fig. 4b, the selectivity of 0.1 and 0.2 % Pd varied little with the temperature. However, the selectivity of 0.3 % Pd decreased rapidly with the temperature.

In Fig. 4c, although the selectivity of 0.1 and 0.2 % Pd are as high as 100 % when conversion is less than 22 %, there is no practical significance since the low conversion. When conversion is more than 80 %, the selectivity of 0.3 % Pd

decreases faster. Therefore, the catalyst with 0.2 % Pd has the best compositive property.

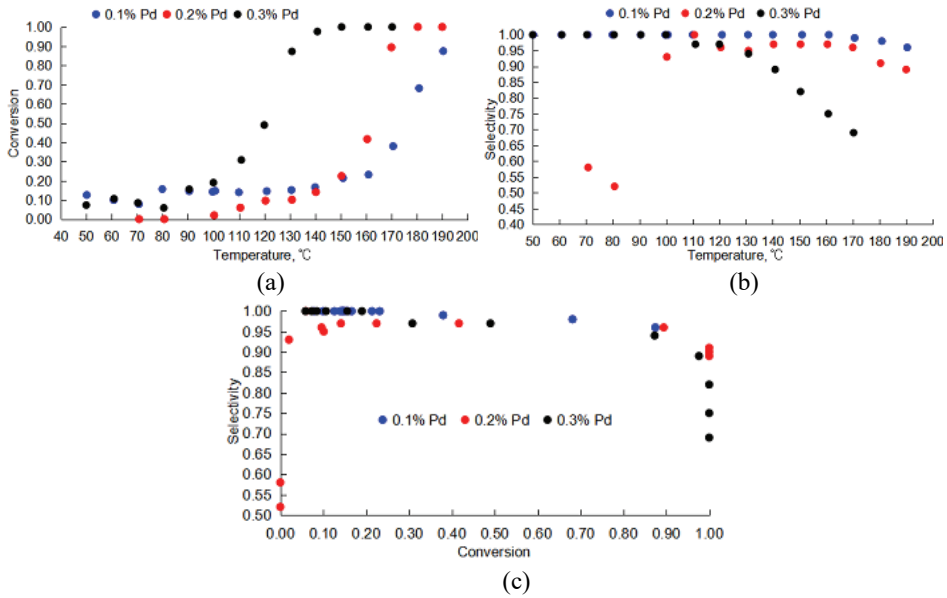

Fig. 4. Effect of the Pd load on catalyst performance: a) the relationship between conversion and temperature; b) the relationship between selectivity and temperature; c) the relationship between selectivity and conversion.

Effect of degradation time. Fig. 5 shows the effect of degradation time on the catalytic performance at 0.2% Pd load.

Fig. 5a shows the change of the conversion with temperature at different degradation times. From Fig. 5a, degradation time had little effect on the conversion below 110 ℃. Above 120 ℃, the conversion of the Pd/degraded CS (4 h) catalyst was significantly higher than that of other catalysts. When the reaction temperature reached 160 ℃, acetylene was completely converted, that is, the conversion of the Pd/degraded CS (4 h) catalyst was 100 %. For the Pd/degraded CS (2 h and 6 h) catalysts, acetylene was completely converted at 190 and 170 ℃, respectively. For the other Pd/degraded CS (0 h, 0.5 h and 1 h) catalysts, the conversions were still below 100 % at 190 °C.

From Fig. 5b, except the selectivity of Pd/degraded CS (0 h, 2 h and 6 h) catalysts was low, there were little differences in the selectivity of the other Pd/degraded CS catalysts. Fig. 5c shows the similar results.

Combining with Fig. 5a and b, it can be concluded that the Pd/degraded CS (4 h) catalyst has the best catalytic effect.

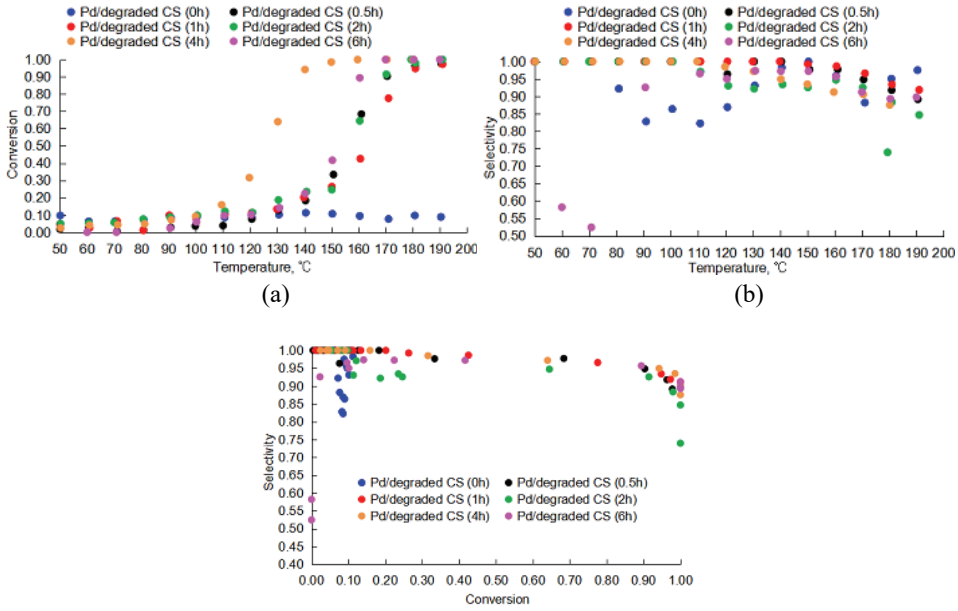

Fig. 5. Effect of degradation time on catalyst performance: a) the relationship between conversion and temperature; b) the relationship between selectivity and temperature; c) the relationship between selectivity and conversion.

Effect of support. Fig. 6 shows the effect of support on the catalytic performance of Pd/CS and Pd/degraded CS (4 h) at 0.2 % Pd load.

As can be seen from Fig. 6a, the conversion of Pd/CS catalyst was lower, the highest conversion was only 11 % in the experimental temperature range. The conversion of Pd/degraded CS (4 h) catalyst was higher than that of Pd/CS. The conversion had reached 94 % at 140 °C and was as high as 100 % at 160 °C.

From Fig. 6b, the selectivity of Pd/CS catalyst was unstable. However, the selectivity of Pd/degraded CS (4 h) showed a regular trend, varying between 100 and 88 %.

From Fig. 6c, the conversion of Pd/CS catalyst was only about 10 %. Such poor conversion has no practical significance.

Therefore, degraded CS (4 h) is more suitable for using as the support of Pd than CS.

Stability of Pd/degraded CS (4 h) catalyst

The stability of a catalyst is very important for industrial application. Hence, the stability of the Pd/degraded CS (4 h) catalyst was tested under the conditions of T = 120 °C, 0.2 % Pd load. Fig. 7 shows the stability results.

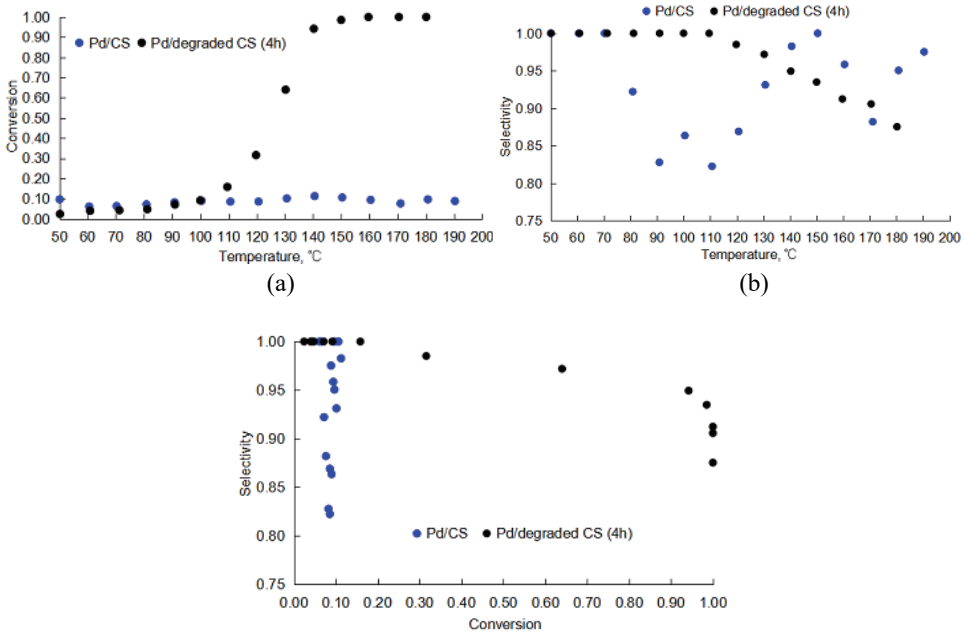

Fig. 6. Effect of support on catalyst performance: a) the relationship between conversion and temperature; b) the relationship between selectivity and temperature; c) the relationship between selectivity and conversion.

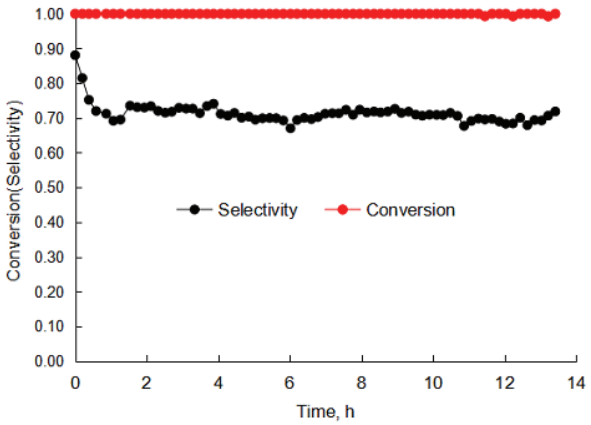

Fig. 7. Acetylene conversion and ethylene selectivity versus time over Pd/degraded CS (4 h) catalyst (T = 120 ℃, 0.2 % Pd load).

As shown in Fig. 7, it is worthy to note that the acetylene conversion over Pd/degraded CS (4 h) remained almost as high as 100 % after 13.5 h. The ethylene selectivity over Pd/degraded CS (4 h) was basically stable at 71 % after 2 h.

During 13.5 h, the ethylene selectivity decreased slightly from 88 to 71 %. These indicate that Pd/degraded CS (4 h) catalyst exhibited good catalytic performance and stability.

CONCLUSIONS

1) CS was successfully degraded in H_2O_2 solution. Degradation of CS made the molecular chain of CS break into small segments. The particle size of degraded CS was much smaller. Pd/degraded CS (4 h) prepared with degraded CS had a larger surface area than Pd/CS prepared with raw CS. Large surface area was more propitious to the dispersion and adsorption of the active metal as well as improving catalytic performance.

2) The results of XRD, FTIR and XPS showed that Pd was successfully coordinated with CS. The chemical states of Pd in Pd/CS and Pd/degraded CS were PdO and PdO*x*, respectively.

3) Among 0.1, 0.2 and 0.3 % Pd load, the Pd/degraded CS (4 h) catalyst with 0.2 % Pd had the best catalytic performance. The conversion and selectivity of Pd/degraded CS (4 h) catalyst could achieve 100 and 91 % at 160 °C, respectively. The low selectivity of conventional Pd-based catalysts was significantly improved.

4) The Pd/degraded CS (4 h) catalyst showed good stability. At lower 120 °C, the acetylene conversion over Pd/degraded CS (4 h) remained almost as high as 100 % and the ethylene selectivity decreased slightly from 88 to 71 % after 13.5 h.

Acknowledgment. This work was supported by National Natural Science Foundation of China (grant number 21476102).

И З В О Д

КАТАЛИТИЧКЕ ПЕРФОРМАНСЕ ПАЛАДИЈУМА/ДЕГРАДИРАНОГ ХИТОЗАНА ЗА СЕЛЕКТИВНУ ХИДРОГЕНАЦИЈУ АЦЕТИЛЕНА

SI-YE TANG[1], XIN-XIANG CAO[1], TONG-TONG DI[2] и XIN-YU LI[3]

[1]College of Chemistry and Chemical Engineering, Luoyang Normal University, Luoyang 471934, China, [2]School of Chemical Engineering, Northwest University, Xian 710069, China и [3]School of Chemical Engineering, Zhengzhou University, Zhengzhou 450001, China

У овом раду испитиване су каталитичке особине катализатора добијених наношењем паладијума на хитозан. Упоређиван је ефекат хитозана и деградираног хитозана на каталитичке перформансе. Структура, морфологија, садржај метала и особине катализатора су испитиване инфрацрвеном спектроскопијом са Фуријеовом трансформацијом, индуктивно спрегнутом плазмом, дифракцијом X-зрачења, нискотемпературском адсорпцијом–десорпцијом N_2 и фотоелектронском спектроскопијом. Резултати су показали да су каталитичке перформансе Pd/деградирани хитозан катализатора боље од Pd/хитозана при одређеним концентрацијама Pd. Катализатор Pd/деградирани хитозан (деградација 4 h) показује одличне каталитичке перформансе и стабилност. Конверзија ацетилена и селективност етилена је достигла 100 и 91 %, редом. У току 13,5 h, конверзија ацетилена је остала 100 %, а селективност етилена је мало опала од 88 до 71 %.

Показано је да је Pd успешно координиран хитозаном; након деградације, честице хитозана постају мање и имају већу специфичну површину; управо су ове честице допринеле побољшању каталитичких перформанси Pd/деградирани хитозан катализатора. Такође, катализатор Pd/деградирани хитозан има високу селективност при високој конверзији, значајно унапређујући карактеристику ниске селективности при високим конверзијама традиционалних катализатора заснованих на Pd.

(Примљено 19. децембра 2024, ревидирано 31. јануара, прихваћено 27. априла 2025)

REFERENCES

1. S. Y. Tang, L. Y. Li, X. X. Cao, Q. Q. Yang, *Heliyon* **9** (2023) e13523 (https://doi.org/10.1016/j.heliyon.2023.e13523)
2. H. Liu, M. Q. Chai, G. X. Pei, X.Y. Liu, L. Li, L. L. Kang, A. Q. Wang, T. Zhang, *Chin. J. Catal.* **41** (2020) 1099 (https://doi.org/10.1016/S1872-2067(20)63568-9)
3. H. Y. Ma, G. C. Wang, *ACS Catal*. **10** (2020) 4922 (https://doi.org/10.1021/acscatal.0c00190)
4. D. Makhmutov, E. Fedorova, A. Zanina, C. Kubis, D. Zhao, D. Doronkin, N. Rockstroh, S. Bartling, U. Armbruster, S. Wohlrab, E. V. Kondratenko, *ACS Catal.* **15** (2025) 2328 (https://doi.org/10.1021/acscatal.4c07462)
5. N. Terzić-Jovanović, V. Ajdačić, *J. Serb. Chem. Soc.* **87** (2022) 669 (https://doi.org/10.2298/JSC220128024T)
6. T. X. Yang, M. Zhao, X. Wang, R. Ma, Y. N. Liu, Y. F. He, D. Q. Li, *Catal. Lett.* **152** (2022) 227 (https://doi.org/10.1007/s10562-021-03620-w)
7. Z. Yang, Y. Li, Y. Cao, X. Zhao, W. Chen, J. Zhang, G. Qian, C. Peng, X. Gong, X. Duan, *Chem. Eng. J.* **445** (2022) 136681 (https://doi.org/10.1016/j.cej.2022.136681)
8. H. Xu, Y. Q. Xu, Y. S. Jiang, Q. F. Zhang, X. N. Li, *Chem. Ind. Eng. Prog*. **38** (2019) 1353 (https://doi.org/10.16085/j.issn.1000-6613.2018-0428) (Chinese)
9. X. Luo, S. B. Guo, D. D. Yu, M. X. Song, F. Zhang, W. P. Fang, W. J. Song, P. F. Ma, W. K. Lai, *Ind. Eng. Chem. Res.* **64** (2025) 2665 (https://doi.org/10.1021/acs.iecr.4c04156)
10. M. Nasrollahzadeh, N. Shafiei, Z. Nezafat, N. S. S. Bidgoli, F. Soleimani, *Carbohydr. Polym.* **241** (2020) 116353 (https://doi.org/10.1016/j.carbpol.2020.116353)
11. H. Y. Luo, D. Y. Liang, Q. Liu, L. Niu, K. Temirlan, W. H. Li, *Carbohydr. Polym.* **354** (2025) 123308 (https://doi.org/10.1016/j.carbpol.2025.123308)
12. E. Guibal, *Prog. Polym. Sci.* **30** (2005) 71 (https://doi.org/10.1016/j.progpolymsci.2004.12.001)
13. S. Zhong, *Kin. Catal.* **61** (2020) 480 (https://doi.org/10.1134/S0023158420030210)
14. K. X. Li, X. F. Song, D. Zhang, *J. Appl. Polym. Sci.* **109** (2008) 1294 (https://doi.org/10.1002/app.28186)
15. X. X. Cao, T. T. Lu, W. T. Xie, M. Arash, B. Adelaide, H. Ricky, W. L. J. Ben, K. K. Jong, M. Karren, C. J. Liu, X. L. Yan, *Front. Chem. Sci. Eng.* **14** (2020) 522 (https://doi.org/10.1007/s11705-019-1822-3)
16. S. Shawe, F. Buchanan, E. Harkin-Jones, D. Farrar, *J. Mater. Sci.* **41** (2006) 4832 (https://doi.org/10.1007/s10853-006-0064-1)
17. J. Li, C. P. Wei, F. M. Wang, L. D. Dong, S. Sun, Q. Y. Liu, *Mater. Sci. Forum* **852** (2016) 1319 (https://doi.org/10.4028/www.scientific.net/MSF.852.1319)
18. T. Baran, A. Menteş, H. Arslan, *Int. J. Biol. Macromol.* **72** (2015) 94 (https://doi.org/10.1016/j.ijbiomac.2014.07.029)

19. N. V. Kramareva, A. E. Koklin, E. D. Finashina, N. S. Telegina, A. Yu. Stakheev, L. M. Kustov, *Kinet. Catal.* **45** (2004) 743 (https://doi.org/10.1023/B:KICA.0000044989.54767.b4)
20. X. Li, K. Cui, Z. Guo, T. Yang, Y. Cao, Y. Xiang, H. Chen, M. Xi, *Chem. Eng. J.* **379** (2020) 122324 (https://doi.org/10.1016/j.cej.2019.122324)
21. N. Anbu, R. Maheswari, V. Elamathi, P. Varalakshmi, A. Dhakshinamoorthy, *Catal. Commun.* **138** (2020) 105954 (https://doi.org/10.1016/j.catcom.2020.105954)
22. I. M. El-Sherbiny, *Eur. Polym. J.* **45** (2009) 199 (https://doi.org/10.1016/j.eurpolymj.2008.10.042)
23. T. Baran, A. *Mentes¸*, *Int. J. Biol. Macromol.* **79** (2015) 542 (http://dx.doi.org/10.1016/j.ijbiomac.2015.05.021).

Journal of the Serbian Chemical Society
JSCS@tmf.bg.ac.rs • www.shd.org.rs/JSCS
J. Serb. Chem. Soc. *90* (6) 781–787 (2025)
JSCS–5420
Short communication
Published 24 June, 2025

SHORT COMMUNICATION

Analyzing food supplements to enhance erectile system function for the presence of undeclared sildenafil and tadalafil using HPLC-DAD

ZORICA BOZHINOSKA[1]*, ZORAN ZHIVIKJ[2], STEFANIJA UBAVKOVA[1], MARIJA BUJAROSKA PERKOVIKJ[1], VERICA POPOSKA[1], ALEKSANDAR STANKOV[1] and TANJA PETRESKA IVANOVSKA[2]

[1]*Institute of Forensic Medicine, Criminology and Medical Deontology, Medical Faculty, Ss. Cyril and Methodius University in Skopje, Mother Theresa 19, 1000, Skopje, Republic of North Macedonia and* [2]*Faculty of Pharmacy, Ss. Cyril and Methodius University in Skopje, Mother Theresa 47, 1000, Skopje, Republic of North Macedonia*

(Received 4 October 2024, revised 8 January, accepted 29 April 2025)

Abstract: Phosphodiesterase-5 (PDE-5) inhibitors, such as sildenafil and tadalafil, are drugs commonly used to improve erectile function. However, some erectile function-enhancing supplements with claims of being entirely natural may be adulterated with these drugs, posing health risks. This study screened supplements for erectile dysfunction from the Republic of North Macedonia using a fast, specific and sensitive HPLC-DAD method (runtime: 15 min). No interference was observed at the retention times of sildenafil and tadalafil, allowing for their unambiguous identification and quantification. Tadalafil was absent, but sildenafil was found in two of eight samples (32.78 and 13.47 mg per dosage). The results demonstrated the applicability of the method to determine whether food supplements marked for the erectile function enhancement are free of sildenafil and tadalafil.

Keywords: adulteration; 5 phosphodiesterase inhibitors; sexual dysfunction; HPLC analysis.

INTRODUCTION

The therapeutic management of erectile dysfunction as a widespread condition affecting male sexual function, involves the use of several classes of drugs, with phosphodiesterase type-5 inhibitors (PDE-5 inhibitors) being the first-line treatment. Sildenafil, the first FDA-approved PDE-5 inhibitor for erectile dysfunction (1998), was later followed by vardenafil, tadalafil and avanafil.[1] How-

* Corresponding author. E-mail: zorica.stojcheska@medf.ukim.edu.mk
https://doi.org/10.2298/JSC241004032B

ever, many men use alternative treatment approaches, including food supplements that contain natural aphrodisiacs extracted from *Panax ginseng*, *Lepidium meyenii* (maca), *Tribulus terrestris* (puncture vine), *Epimedium*, *Ginkgo biloba* and *Withania somnifera* (ashwagandha).[2] To achieve effects comparable to sildenafil in improving erectile function, some manufacturers illegally add pharmaceutical active substances and their analogs to these products.[3] This unethical practice, known as adulteration, allows manufacturers to profit from satisfied consumers, but poses health risks[4] due to weak supplement regulations.[5,6] FDA data shows many erectile dysfunction supplements contain undeclared sildenafil or its analogs,[7] which are dangerous for patients on nitrates, alpha blockers or CYP3A4 inhibitors.[8] Hence, the regulatory bodies have to increase regular inspections to ensure safety. To realize this, adequate spectroscopic and/or chromatographic methods[9–14] is required to enable simple and easy identification, detection and quantitative determination of adulterants in food supplements. Although there is growing interest in rapid and non-destructive spectroscopic methods,[14] the use of chromatography as confirmatory technique is unavoidable.[15,16] HPLC is widely recognized as a versatile and relevant technique for analyzing diverse samples, including multi-component dosage forms, due to its high sensitivity, speed and precision.[17] Thus, this study is aimed to propose a sensitive, specific and accurate HPLC-DAD approach that can be routinely applied for the simultaneous determination of sildenafil and tadalafil as adulterants in commercially available food supplements marketed for the improvement of erectile function.

EXPERIMENTAL

Materials and reagents

Tadalafil and sildenafil citrate reference standards (Ph. Eur) were obtained from Sigma–Aldrich. Eight erectile dysfunction supplements, marketed as natural products, were randomly selected from shops in North Macedonia. Besides herbal compounds, some supplements also included amino acids, vitamins and honey. Three supplements originated from Poland, two from Bulgaria, and one each from the UK, Hungary and India. The supplements were available in different forms: one as a tablet, one as a sachet and the rest as capsules. HPLC-grade acetonitrile (Thermo Fisher), sodium phosphate dibasic dehydrate (Sigma–Aldrich), and 85 % orthophosphoric acid (Park, UK) was used for the phosphate buffer. Ultrapure water from the Heal Force NW system was used throughout.

Instrumental and analytical conditions

A Waters Alliance e-2695 HPLC with a 2998 PDA detector was used. Separation was performed on a Symmetry C8 column (5 μm, 4.6 mm×250 mm) with a C18 guard column. The isocratic mobile phase consisted of acetonitrile and 50 mM phosphate buffer with pH 6.6 (45:55 volume ratio) flowed at 1 mL/min. A 20 μL injection was analyzed at 225 nm using Empower software, version 3.

Preparation of standard stock solutions and samples

Tadalafil and sildenafil citrate stock solutions (20 mg each) were prepared in 50 mL volumetric flasks using the mobile phase and sonication. Working solutions (0.2 mg/mL) and a combined standard solution (0.2 mg/mL each) were also prepared. A quantity of solid samples, corresponding to the homogenized average weight of a tablet or capsule (*Ph. Eur.* **10**, 2021), and the entire content of a sachet sample (9 g) were dissolved in 50 mL of the mobile phase, vortexed and sonicated for 15 min. Each sample was prepared in triplicate, filtered (0.2 μm nylon), and transferred to vials for analysis.

Method validation

The method was validated according to ICH guidelines, encompassing the validation parameters such as specificity, linearity, accuracy, precision, sensitivity and robustness.[21] Method specificity was assessed by analyzing the mobile phase (diluent), blank, tadalafil, and sildenafil citrate solutions at a concentration of 0.2 mg/mL, as well as mixed standard solution at the same concentration (0.2 mg/mL). The linearity was tested using mixed standard solutions at seven concentrations (0.0002–0.3 mg/mL corresponding to 0.1 to 150 % of the target concentration), with three injections per level. *LOD* and *LOQ* for tadalafil and sildenafil citrate were determined using the standard deviation (σ) and slope (S), calculated as $LOD = 3.3\sigma/S$ and $LOQ = 10\sigma/S$. The accuracy was evaluated at 50, 100 and 150 % of the target concentration (0.1, 0.2 and 0.3 mg/mL) with triplicate samples prepared by mixing of sildenafil citrate and tadalafil with a blank matrix and diluting in the mobile phase. The recovery of the added tadalafil and sildenafil citrate, as well as the relative standard deviation (*RSD*), was calculated for each set of replicates. Precision was confirmed through six same-day injections of a mixed standard solution at 100 % concentration. Robustness was assessed by varying flow rate, column temperature and concentration and pH of the phosphate buffer. Analytical solution stability was tested by analysing the standard solutions at 0, 2, 4, 6, 12 and 24 h in a single run and after 24, 36, 48 and 72 h under refrigeration. Six injections per solution were analysed, calculating the average recovery and *RSD*.

RESULTS AND DISCUSSION

HPLC-DAD method

The HPLC method for the determination of undeclared sildenafil and tadalafil in food supplements for erectile dysfunction was based on the method reported by Fidan and Bakirdere (2016)[19] with certain modification according to green chemistry principles.[21,22] To reduce acetonitrile content from 65 vol. % in the original method,[19] variations from 60 to 40 % were tested, with 45 vol. % providing optimal separation. Lowering the use of acetonitrile is crucial, as it was recognized as an environmental hazard,[24] aligning with modern efforts to minimize chemical pollution of the environment.[20,21]

The specificity of the method was confirmed by chromatograms showing no co-elution of tadalafil (7.79 min) and sildenafil citrate (9.08 min), Fig. 1. A strong linear correlation was observed ($R^2 = 0.9986$ for tadalafil, $R^2 = 1.0000$ for sildenafil citrate) across the concentration range of 0.0002 to 0.3 mg/mL. Sensitivity was high, with *LOD*s of 0.0022 mg/mL for tadalafil and 0.0005 mg/mL for sildenafil citrate and *LOQ*s of 0.0067 and 0.0014 mg/mL, respectively. The

accuracy ranged from 99.45–101.36 % for tadalafil and 99.06–100.34 % for sildenafil citrate, with RSDs below 2.0 % (Table I). The method proved robust under minor HPLC condition variations, including flow rate (0.8, 1 and 1.2 mL/min), column temperature (20, 25 and 30 °C), phosphate buffer concentration (40 50 and 60 mM), and pH of the phosphate buffer (6.3, 6.6 and 6.9). and stable over 72 h (*RSD*s of 0.16 for tadalafil and 0.10 for sildenafil citrate).

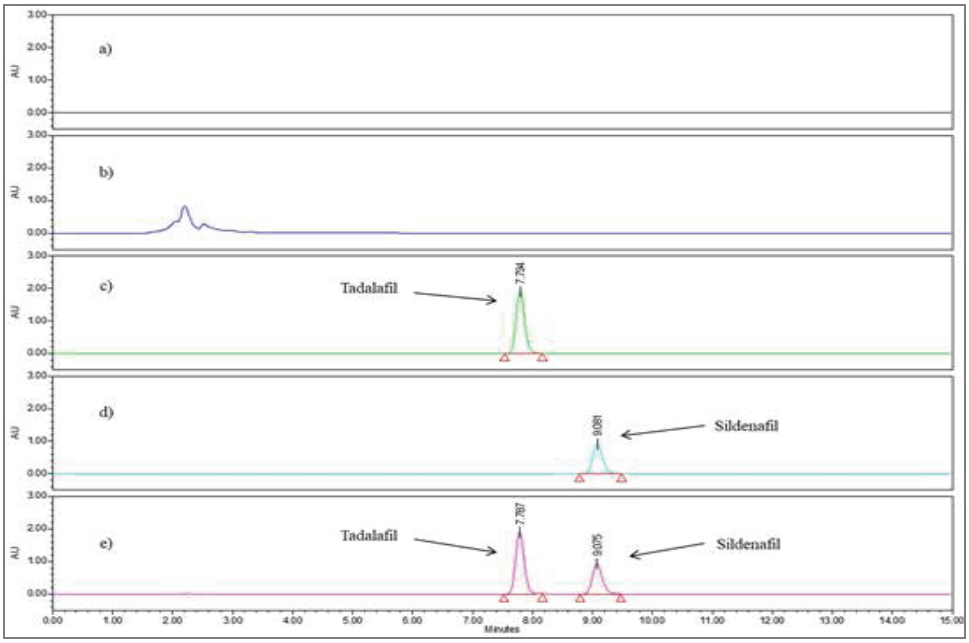

Fig.1. HPLC chromatograms: a) mobile phase (diluent); b) blank; c) standard solution of tadalafil (0.2 mg/mL); d) standard solution of sildenafil citrate (0.2 mg/mL); e) standard solution of both tadalafil and sildenafil citrate (0.2 mg/mL).

TABLE I. Accuracy and precision of HPLC-DAD method for determination of sildenafil citrate and tadalafil as adulterants in food supplements for improving erectile function

Parameter	Accuracy, recovery + *RSD*, %			Precision *RSD* / %
Concentration unit (concentration level)	mg/mL (50 %)	mg/mL (100 %)	mg/mL (150 %)	
Tadalafil	100.27 + 0.89	101.02 + 0.43	100.22 + 0.13	0.13
Sildenafil citrate	99.65 + 0.27	99.45 + 0.37	99.80 + 0.37	0.16

Determination of sildenafil and tadalafil in real samples

Two of the eight analysed food supplements for erectile dysfunction contained undeclared sildenafil, representing 25 % of samples. The sachet sample, manufactured in Bulgaria, and the capsule sample, manufactured in India, matched the UV spectra and retention time of the standard (Fig. 2). The sachet

contained 18.92 mg of sildenafil citrate (equivalent to 13.47 mg of sildenafil), while the capsule contained 46.02 mg of sildenafil citrate (equivalent to 32.78 mg of sildenafil). Both samples did not comply with the claim of being natural. These products were found to be adulterated with a medium-low and moderate doses of sildenafil, considering that prescription drugs contain sildenafil as the active component at a dose of 5, 20, 25, 50 and 100 mg. The undisclosed sildenafil adulteration poses health risks, especially for consumers avoiding PDE-5 inhibitors or taking other medications increasing the potential for severe complications.

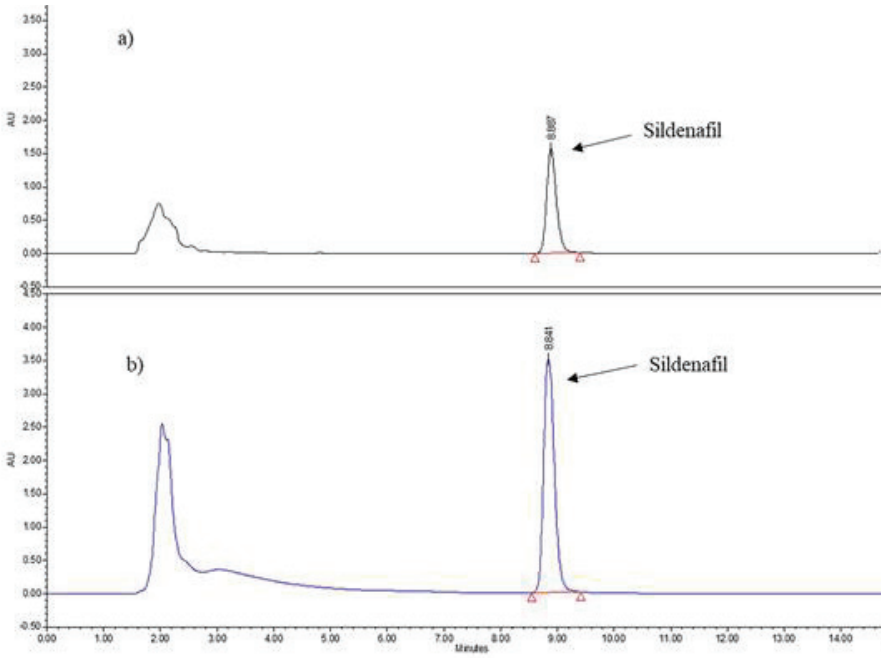

Fig. 2. HPLC chromatograms: a) supplement containing sildenafil 13.47 mg/sachet; b) supplement containing sildenafil 32.78 mg/capsule.

Certain studies confirm the global issue of PDE-5 inhibitor adulteration in "natural" supplements for erectile dysfunction,[22–24] aligning with our findings. In Nairobi, 32.5 % of 80 tested herbal products contained undeclared sildenafil.[22] Similar adulteration rates were found in Malaysia, Romania and Bangladesh, with supplements originating from China, the USA, Europe, India and other regions.[10,12,22–24] These studies highlight the global trend of using sildenafil to adulterate supplements marketed as natural products for improving erectile function. Efficient screening methods are crucial for regulatory enforcement. Our proposed HPLC method offers a simple sample preparation, a 15-min runtime, and moderate use of organic solvents, making it efficient for the routine sildenafil and tadalafil detection.

CONCLUSION

This study investigated eight erectile dysfunction supplements in the Republic of North Macedonia for undeclared sildenafil and tadalafil using HPLC--DAD. The method ensured good separation within 15 min with minimal sample preparation. Two supplements from Bulgaria and India contained sildenafil at medium-low and moderate doses. The authorities must address adulteration and warn the public that "natural" supplements are not always safe. Given the potential health risks, thorough screening is essential, and our cost-effective, sensitive HPLC method offers a practical solution.

Acknowledgement. The authors would like to acknowledge the financial support of the Faculty of Pharmacy, University Ss. Cyril and Methodius in Skopje, Project No. 03-766/1-10.10.2022.

И З В О Д

АНАЛИЗА СУПЛЕМЕНАТА ЗА ПОБОЉШАЊЕ ФУНКЦИЈЕ ЕРЕКТИЛНОГ СИСТЕМА НА ПРИСУСТВО НЕПРИЈАВЉЕНОГ СИЛДЕНАФИЛА И ТАДАЛАФИЛА КОРИШЋЕЊЕМ HPLC-DAD

ZORICA BOZHINOSKA[1], ZORAN ZHIVIKJ[2], STEFANIJA UBAVKOVA[1], MARIJA BUJAROSKA PERKOVIKJ[1], VERICA POPOSKA[1], ALEKSANDAR STANKOV[1] и TANJA PETRESKA IVANOVSKA[2]

[1]Institute of Forensic Medicine, Criminology and Medical Deontology, Medical Faculty, Ss. Cyril and Methodius University in Skopje, Mother Theresa 19, 1000, Skopje, Republic of North Macedonia, [2]Faculty of Pharmacy, Ss. Cyril and Methodius University in Skopje, Mother Theresa 47, 1000, Skopje, Republic of North Macedonia

Инхибитори фосфодиестеразе-5 (PDE-5), као што су силденафил и тадалафил, су често коришћени лекови за побољшање еректилне функције. Поједини суплементи за побољшање еректилне функције, који су декларисани као потпуно природни могу садржавати ове лекове, што представља ризик по здравље. У овом раду су испитани суплементи за еректилну дисфункцију из Републике Северне Македоније применом брзе, специфичне и осетљиве HPLC-DAD методе (трајање анализе је 15 min). Утврђено је да нема интерференција на ретенционим временима сиденафила и тадалафила што омогућава њихову идентификацију и квантификацију. У испитиваним узорцима није утврђено присуство тадалафила, док је силденафил идентификован и квантификован у два од осам узорака (32,78 и 13,47 mg по дози). Добијени резултати указују на применљивост ове методе за утврђивање да ли су природни суплементи за побољшање еректилне функције, доступни на тржишту, без додатака сиденафила и тадалафила.

(Примљено 4. октобра 2024, ревидирано 8. јануара, прихваћено 29. априла 2025)

REFERENCES

1. S. A. Huang, J. D. Lie, *Pharm. Ther.* **38** (2013) 407 (https://www.ncbi.nlm.nih.gov/pmc/articles/PMC3776492/)
2. O. R. C. Gheorghiu, A. M. Ciobanu, C. M. Guțu, C. L. Chițescu, G. V. Costea, D. M. Anghel, A. M. Vlasceanu, D. L. Baconi, *Molecules* **28** (2023) 4116 (https://doi.org/10.3390/molecules28104116)
3. L. Muschietti, F. Redko, J. Ulloa, *Drug Test. Anal.* **12** (2020) 861 (https://doi.org/10.1002/dta.2806)

4. M. Momtaz, S. Y. Bubli, M. S. Khan, *Foods* **12** (2023) 199 (https://doi.org/10.3390/foods12010199)
5. J. T. Dwyer, P.M. Coates, M. J. Smith. *Nutrients* **10** (2018) 41 (https://doi.org/10.3390/nu10010041)
6. S. Thakkar, E. Anklam, A. Xu, F. Ulberth, J. Li, B. Li, M. Hugas, N. Sarma, S. Crerar, S. Swift, T. Hakamatsuka, V. Curtui, W. Yan, X. Geng, W. Slikker, W. Tong, *Regul. Toxicol. Pharmacol.* **114** (2020) 104647 (https://doi.org/10.1016/j.yrtph.2020.104647)
7. J. Tucker, T. Fischer, L. Upjohn, D. Mazzera, M. Kumar, *JAMA Netw. Open* **1** (2018) e183337 (https://doi.org/10.1001/jamanetworkopen.2018.3337)
8. I. A. Ayta, J. B. McKinlay, R. J. Krane, *B.J.U.I.* **84** (1999) 50 (https://doi.org/10.1046/j.1464-410x.1999.00142.x)
9. E. Dural, *Turk J. Pharm Sci.* **17** (2020) 56 (https://doi.org/10.4274/tjps.galenos.2018.91249)
10. A. K. Podder, J. K. Chakrobarty, A. B. M. Faroque, *Asian J. Pharm. Clin. Res.***7** (2014) 25 (https://journals.innovareacademics.in/index.php/ajpcr/article/view/987/760)
11. F. Akuamoa, T. F. H. Bovee, R. van Dam, L. Maro, S. Wesseling, J. Vervoort, I. M. C. M. Rietjens, R. L.A. P. Hoogenboom, *Food Addit. Contam., A* **39** (2022) 1021 (https://doi.org/10.1080/19440049.2022.2052972)
12. A. M. Popescu, G. L. Radu, T. Onisei, A. E. Raducacu, C. G. Niculae, *Rom. Biotechnol. Lett*. **19** (2014) 9493 (https://rombio.unibuc.ro/wp-content/uploads/2022/05/19-4-4.pdf)
13. D. T. C. Minh, L. A.Thi, N. T. T. Huyen, L.V. Vu, N. T. K. Anh, P. T. Thanh Ha, *J. Pharm. Biomed. Anal.***174** (2019) 340 (https://doi.org/10.1016/j.jpba.2019.05.043)
14. C. Mateescu, A. M. Popescu, G. L. Radu, T. Onisei, A. E. Raducanu*, Adv. Pharm. Bull.* **7** (2017) 251 (https://doi.org/10.15171/apb.2017.030)
15. C. J. Mwankuna, G. A. Uwamaliya, E. E. Mariki, F. Mabiki, H. M. Malebo, R. Mdegela, B. Styrishave, *Anal. Methods* **14** (2022) 1060 (http://doi.org/10.1039/d1ay01966j)
16. R. F. Alotaibi, H. H. Al Tilasi, A. M. Al-Mutairi, H. S. Alharbi, *Heliyon* **10** (2024) e31467 (http://doi.org/10.1016/j.heliyon.2024.e31467)
17. J. S. N'cho, I. Fofana, Y. Hadjadj, A. Beroual, *Energies* **9** (2016) 367 (https://doi.org/10.3390/en9050367)
18. European Medicines Agency, *ICH Q2(R2) Validation of analytical procedures – Scientific guideline*, 2022 (https://www.ema.europa.eu/en/ich-q2r2-validation-analytical-procedures-scientific-guideline)
19. S. A. K. FIdan, S. Bakirdere, *J. AOAC Int.* **99** (2016) 923 (https://doi.org/10.5740/jaoacint.15-0320)
20. M. Tobiszewski, J. Namieśnik, F. Pena-Pereira, *Green Chem.* **19** (2017)1034 (http://doi.org/10.1039/C6GC03424A)
21. S. I. Kaya, A. Cetinkaya, S. A. Ozakan, *Tr. Env. Anal. Chem*. **33** (2022) e00157 (https://doi.org/10.1016/j.teac.2022.e00157)
22. S. W. A. Sifuma, J. W. Mwangi, P. C. Mutai, D. B. Ongarora, N. M. Njuguna, *Int. J. Pharm. Sci. Res.* **13** (2022) 2095 (https://doi.org/10.13040/IJPSR.0975-8232.13(5).2095-00)
23. H. H. Fard, M Akhgari, *J. Pharm. Pharmacogn. Res.* **6** (2018) 45 (https://doi.org/10.56499/jppres17.265_6.1.45)
24. C. N. Man, N. M. Nor, R. Lajis, G. L. Harn, *J Chromatogr., A* **1216** (2009) 8426 (https://doi.org/10.1016/j.chroma.2009.10.016).

Journal of the Serbian Chemical Society
JSCS@tmf.bg.ac.rs • www.shd.org.rs/JSCS
J. Serb. Chem. Soc. 90 (6) 789–802 (2025)
JSCS–5421
Original scientific paper
Published 24 June, 2025

Effect of different compatibilizers and aluminium hydroxide amount on the thermophysical and thermomechanical properties of polypropylene random copolymer/aluminium hydroxide composites

FATIMA MUSTAFAYEVA[1]*, NAJAF KAKHRAMANOV[1], GALINA MARTYNOVA[2] and NELI KOSEVA[3]

[1]Institute of Polymer Materials of Ministry of Science and Education Republic of Azerbaijan, S. Vurgun Str. 124, Sumgait, Republic of Azerbaijan, [2]Institute of Geology and Geophysics of Ministry of Science and Education Republic of Azerbaijan, H. Javid av. 119, Baku, Republic of Azerbaijan and [3]Institute of Polymers, Bulgarian Academy of Sciences, ul. "Akad. Georgi Bonchev" 103, 1113 Geo Milev, Sofia, Bulgaria

(Received 12 December 2024, revised 3 February, accepted 19 March 2025)

Abstract: This study investigates the effects of three different types of commercial available compatibilizers (DuPont™ Fusabond® P353 polymer modifier, Exxelor™ PO 1020, LIBAID T-2) on the thermal properties of composites based on polypropylene random copolymer/aluminium hydroxide (PP-R/ATH). The influence of the above-mentioned compatibilizers and the ATH amount on the thermophysical and thermomechanical properties of composites based on PP-R/ATH is considered. Thermal properties of the obtained composites were analyzed using differential scanning calorimetry, thermogravimetric analysis, derivative thermogravimetry and thermomechanical curves. The results of the study show that the content of ATH in the PP-R matrix in the presence of a compatibilizer and without it has a noticeable effect on the regularities of changes in thermophysical and thermomechanical characteristics. With increasing filler content, the following were observed: an increase in the amount of residue corresponding to 700 °C, temperature at the maximum mass loss rate, 50 % decomposition temperature and a decrease in temperature at onset degradation. The effect of the used compatibilizer was not significant to the melting temperature at low amount (5 wt. %) of ATH; however, different results were obtained for high amounts (50 wt. %) of filler. Composites with compatibilizer had lower melting enthalpies than those without compatibilizer.

Keywords: polypropylene random copolymer; aluminium hydroxide; compatibilizer; maleic anhydride functionalized polypropylene copolymer; maleic

* Corresponding author. E-mail: mustafayevafatima@mail.ru, F.A.Mustafayeva@gmail.com
https://doi.org/10.2298/JSC241112021K

anhydride functionalized homopolypropylene; blend of fatty acid metal soap and amide; melting temperature; decomposition temperature.

INTRODUCTION

As it is known, one of the main disadvantages of polymeric materials is their high flammability. Being organic in nature, polymeric materials used in various fields of engineering and technology are materials that are prone to combustion and fire spread, leading to loss of life and material damage. In this regard, to obtain fire resistant polymer composite materials with improved physical and mechanical properties is a priority task in the field of materials science. As a matrix material, polypropylene (PP) is the most promising material due to its relatively high melting point, low cost, good physical and mechanical properties, and ease of processing by injection molding, extrusion, vacuum-pneumatic molding, *etc*. PP based composites are widely used in many areas of industry: aircraft manufacturing, automotive manufacturing, shipbuilding, electronics, military and space technology, *etc*. PP, the production volume of which is continuously increasing, is one of the most produced and consumed polymers in the world.[1] At the same time, the main disadvantage of using PP for special purposes is their flammability. In addition, PP forms molten droplets when burned and releases a large amount of heat and toxic gases. Therefore, improving the flame-retardant properties of the polyolefin under consideration (polypropylene random copolymer) is an important research task.[2,3]

The use of flame retardants is a simple and effective way to reduce the fire hazard of polymers. In this case, aluminium hydroxide (ATH) has many advantages over halogen-based flame retardants, including environmental friendliness, low cost, smoke suppression, low toxicity, minimization of melt droplet formation and low corrosion.[4–6] Therefore, considering the environmental benefits, ATH is widely used as a flame retardant and is one of the main reasons for its increasing practical use every year. ATH is one of the most commonly used retardants, making up approximately 34–40 % of the total flame retardants used worldwide.[7] It is generally believed that ATH in polymeric materials performs a triple function: filler, flame retardant and smoke extinguisher.[8] Endothermic decomposition of ATH general occurs within the temperature range of 220–300 °C and the enthalpy of water release is 1.17 kJ g^{-1} for it:[9] $2Al(OH)_3 \rightarrow Al_2O_3 + 3H_2O$.

This endothermicity is certainly part of the mode of action of ATH. Water produced during decomposition both cools the substrate surface and dilutes flammable gases that are expelled from the thermally decomposing substrate. The Al_2O_3 that remains in the substrate acts as a heat sink and also reduces the further release of low molecular weight volatiles.[7] The effectiveness of ATH on flame retardant properties is directly proportional to its content in the polymer compo-

site. So, for example, to achieve sufficient flame-retardant properties of a material, it is necessary to use it in the composition of a polymer matrix in an amount of approximately 50–60 wt. %. However, such a high degree of filling has a negative impact on the change in the physical and mechanical characteristics of the composites.

The dispersion of fillers and their compatibility with the polymer matrix are the main factors that determine the high quality characteristics of composite materials. Therefore, in the world, a lot of attention has been paid to problems related to the development and study of the properties of composites based on PP/ATH.[10–12] The PP/ATH composite was found to be more fire resistant as compared to pure PP.[13] Parida and co-authors used MAPP to improve the compatibility between PP and ATH and found that with increasing amounts of ATH of different sizes (nano or micro), the flame retardant properties of the composite increased, while the tensile strength and elongation at break decreased. Noorasikin *et al*.[14] studied the effect of two different types of coupling agent (3-aminopropyltriethoxysilane and maleic anhdridegraftted polyproplene) on the flame retardant properties of PP/ATH-based nanocomposites and showed that the type of coupling agents affects fire retardancy.[15] Many studies have also shown that the addition of a compatibilizer can improves the thermal properties of composites,[16,17] increases their thermal stability,[18] onset decomposition temperature,[19] final decomposition temperature[20] and reduces mass loss.[20]

Based on the above, the main objective of this work was to study the influence of the type of commercial grade compatibilizer and amount of ATH on the thermophysical and thermomechanical properties of composite materials, including the determination of their softening temperature, melting temperature and decomposition temperature.

EXPERIMENTAL

Materials

The polypropylene used was polypropylene random copolymer (PP-R) Topilene® R200P (Hyosung Chemical Corporation), with a melt index of 0.2 g/10 min (temperature = 230 °C, load = 2.16 kg) and 0.90 g/cm^3 density. The ATH was used (repackaged by ZAO Vekton, OKP 931887, GOST 11841-76), finely ground in A-11 basic (IKA, Germany) brand analytical mill. ATH with average particle size of 56 nm (Dv(10) = 0.0197 μm; Dv(50) = 0.0559 μm; Dv(90) = 0.159 μm) was used. Size determination of filler particles was carried out on a Mastersizer 3000 (Malvern Instruments, England) laser analyzer with a measurement range of 10 nm to 3500 μm.

Three kinds of compatibilizer were used to compatibilize PP-R/ATH blend. The first compatibilizer used was DuPont™ Fusabond® P353 polymer modifier (DuPont Company) – polypropylene copolymer grafted with maleic anhydride (PPC-g-MAH), MAH grafting degree 1.3–1.9 %. Physical properties: 0.904 g/cm^3, 22.4 g/10 min melt flow index (160 °C/325 g). Thermal properties: 135 °C melting point, 112 °C Vicat softening point.

The second compatibilizer used was maleic anhydride functionalized homopolypropylene (PPH-g-MAH) – Exxelor^{TM} PO 1020 polymer resin (ExxonMobil Chemical Company), maleic anhydride level is in the range of 0.5–1.0 wt. %. This grade is designed to function as a coupling agent between reinforcing materials, such as inorganic fillers and polypropylene. Physical properties: 0.900 g/cm^3, 430 g/10 min melt flow index (230 °C/2.16 kg). Thermal properties: 162 °C peak melting temperature.

The third used coupling agent was blend of fatty acid metal soap and amide – LIBAID T-2 (Liberty Chemicals). Specification: 100–105 °C melting point, > 300 °C flash point. It is unique processing aid developed for applications where filler need to be dispersed uniformly in polymer matrix. LIBAID T-2 has sites available for hydrogen bonding and is therefore able to act as a physical coupling agent between polymer systems and a range of filler materials. This permits LIBAID T-2 to act as an efficient blending or dispersing agent in highly filled systems, providing a more uniform and homogenous initial mix.

The dosage of a compatibilizers is based on the results of our previous research results and also on the supplier recommendations.[21,22] Table I lists the amounts of components in each sample.

TABLE I. Identification and formulations of all prepared samples

Sample code	PP-R wt. %	ATH wt. %	Compatibilizer, wt. %		
			PPC-g-MAH	PPH-g-MAH	LIBAID T-2
PP–R	100	–	–	–	–
PA_1	99	1	–	–	–
PA_3	97	3	–	–	–
PA_5	95	5	–	–	–
PA_{10}	90	10	–	–	–
PA_{20}	80	20	–	–	–
PA_{30}	70	30	–	–	–
PA_{50}	50	50	–	–	–
PC	97	–	3	–	–
PCA_1	96	1	3	–	–
PCA_3	94	3	3	–	–
PCA_5	92	5	3	–	–
PCA_{10}	87	10	3	–	–
PCA_{20}	77	20	3	–	–
PCA_{30}	67	30	3	–	–
PCA_{50}	47	50	3	–	–
PH	98	–	–	2	–
PHA_1	97	1	–	2	–
PHA_3	95	3	–	2	–
PHA_5	93	5	–	2	–
PHA_{10}	88	10	–	2	–
PHA_{20}	78	20	–	2	–
PHA_{30}	68	30	–	2	–
PHA_{50}	48	50	–	2	–
PL	99	–	–	–	1
PLA_1	98	1	–	–	1
PLA_3	96	3	–	–	1

TABLE I. Continued

Sample code	PP–R wt. %	ATH wt. %	Compatibilizer, wt. %		
			PPC-g-MAH	PPH-g-MAH	LIBAID T-2
PLA_5	94	5	–	–	1
PLA_{10}	89	10	–	–	1
PLA_{20}	79	20	–	–	1
PLA_{30}	69	30	–	–	1
PLA_{50}	49	50	–	–	1

RESULT AND DISCUSSION

The thermal performance of composites was determined *via* TGA, derivative thermogravimetry (DTG), DSC and thermomechanics.

Resistance to thermal degradation of polymeric materials is an important parameter, since it determines the thermal stability of polymer composite materials and allows determining their temperature range of processing and application in various operating conditions. TGA was carried out to determine the influence of the choice of the compatibilizer type and ATH amount on the thermal stability of the samples. Fig. 1 shows the TGA diagrams for initial components (PP-R, $Al(OH)_3$), PP-R/ATH composites and for the composites in the presence of a compatibilizer (PP-R/compatibilizer/ATH) at different $Al(OH)_3$ contents.

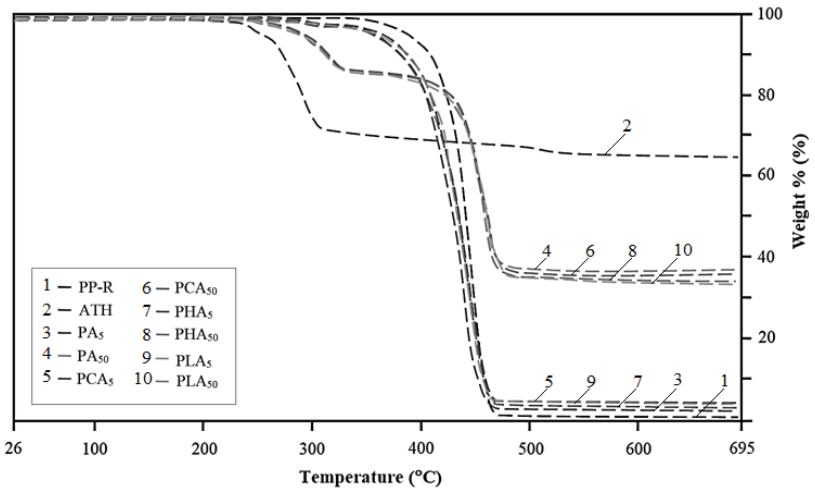

Fig. 1. TGA curves of composites based on PP-R/ATH.

As can be seen from this figure, the decomposition of the initial filler ATH begins at 234 °C and is accompanied by a mass loss of 34.661 wt. % due to decomposition and the release of water vapor from its composition. The resulting residue based on Al_2O_3 is 65.339 wt. %. On the other hand, pure PP-R undergoes

thermal destruction at a temperature of 345 °C and continues up to 475 °C, leaving a residue of 0.343 wt. %.

In the case of PP-R/ATH composites with and without compatibilizer, they present very similar curves that are superimposed on each other. As expected from the analysis of the TGA results of polymer composites, the used compatibilizer has virtually no effect on the thermal stability of the resulting composites. This circumstance indicates that the action of the compatibilizer manifests itself only in the solid state and in the melt of the composite, *i.e.*, up to the temperature of thermal destruction.

The decomposition of PP-R/ATH based composites filled with $Al(OH)_3$ is one of the complex thermal processes, especially at its initial stage. According to the TGA data in Fig. 1, the decomposition process begins at lower temperatures. A TGA study of the composites showed that their thermal stability depends on the ATH content. The initial decomposition temperature (weight loss of 1.266 %) of PA_5 was around 318 °C, which was much lower than that of pure PP-R. Furthermore, with the addition of a compatibilizer, the initial decomposition temperatures of the compatibilized blends were all increased. This circumstance allows us to assert that physical bonding of the compatibilizer to the polymer matrix can contribute to an increase in the initial stage of thermal stability.[23]

Table II shows the effect of filler content on the melting temperature (T_m) and temperature characteristics of thermal decomposition of composites and the content of residue at 700 °C. According to the data in this table, the addition of flame-retardant filler ($Al(OH)_3$) improved the thermal stability of the composites.

TABLE II. Thermal properties of composites based on PP-R/ATH; $T_{50\%}$ – 50 % decomposition temperature; T_{max} – temperature of maximum decomposition rate

Sample code	T_m / °C	T_{onset} / °C	$T_{50\%}$ / °C	T_{max} / °C	Residue at 700°C, wt. %
ATH	–	234.34	–	294.70	65.339
PP-R	145.36	345.32	451.48	451.48	0.343
PA_5	146.69	318.25	441.19	441.19	2.381
PCA_5	146.19	330.56	446.17	446.17	3.035
PHA_5	149.33	336.52	446.44	446.44	3.092
PLA_5	146.40	341.07	446.96	446.96	3.926
PA_{50}	146.67	246.72	449.30	461.40	32.722
PCA_{50}	137.77, 204.63	246.46	461.35	461.35	34.564
PHA_{50}	138.90	247.93	461.97	461.97	32.653
PLA_{50}	147.04	247.03	461.45	461.45	32.756

PP-R exhibits one stage of rapid thermal decomposition. The composites containing 5 wt. % ATH exhibit one main mass loss stage, while the composites containing 50 wt. % ATH showed two mass losses stage (Fig. 1). The thermogram of samples with 50 wt. % ATH is represented by a complex multi-stage decomposition curve, consisting of 2 main sections. The first decomposition area

was attributed to the loss of removal of water from ATH. The second region of thermal decomposition corresponded to the decomposition of the polymer matrix itself.

Early decomposition of ATH in PP-R/ATH and PP-R/compatibilizer/ATH composites is due to the endothermic dehydration of $Al(OH)_3$ at about 234 °C. The onset temperature degradation values of the composites containing ATH shifted to lower temperatures. The onset thermal destruction of composites with 5 wt. % content of ATH varies within the range of 10–20°, and with an ATH content of 50 wt. % within the range of 1°. The temperature for maximum rate of thermal destruction corresponding to the peak in the DTG plot is also maintained around the value of 446 °C for PCA_5, PHA_5, PLA_5 and 461 °C for PA_{50}, PCA_{50}, PHA_{50} and PLA_{50}. This confirms the independence of the thermal decomposition process from the degree of dispersion as well as polymer-filler interaction.

Onset decomposition temperature of the PP-R/ATH composite is lower than that of PP-R due to early decomposition of ATH. The use of compatibilizers with PP-R/ATH leads to an increase in T_{onset}. The temperature of 50 % weight loss ($T_{50\%}$) of the PP-R/compatibilizer/50 wt. % ATH of higher than that on PP-R, and the use of compatibilizers produces no significant change in $T_{50\%}$.

The obtained results show that with an increase in the amount of ATH in the composite, there is an increase in the residue due to the formation of aluminium oxide. This fact indicates that the flame-retardant additive ($Al(OH)_3$) creates an effective barrier layer that limits heat transfer into the internal volume of the polymer matrix, thereby reducing the rate of mass loss of the composites.[24] Al_2O_3 has a melting point of 2852 °C, which confirms its extremely high heat resistance. There is reason to believe that the decomposition product (Al_2O_3), contribute to a significant inhibition of the process of thermal decomposition of PP-R.[25]

Experimentally measured derivative thermogravimetric (DTG) curves of initial PP-R, ATH and composites based on them with different compatibilizer and ATH content are presented in Fig. 2. From the DTG data, it could be found that the pure PP-R had the largest thermal weight loss rate of 25.715 % min^{-1} at 451.48 °C, while which of the PCA_{50}, PHA_{50} and PLA_{50} composites was only about 15.264, 15.721 and 14.543 % min^{-1} at the temperature 461.35, 461.97 and 461.45 °C, respectively, indicating that the addition of ATH retarded the thermal degradation rate of polymer and increased the thermal stability of polymer. Thus, the above thermal analysis results showed that the introduction of ATH into PP-R resulted in lower maximum weight loss rate and higher residue (Table II) which suggested an increase of the thermal stability.[26] The addition of a compatibilizer improves dispersion of the filler particles, which results in a noticeable improvement in the thermal stability of PP-R.[17]

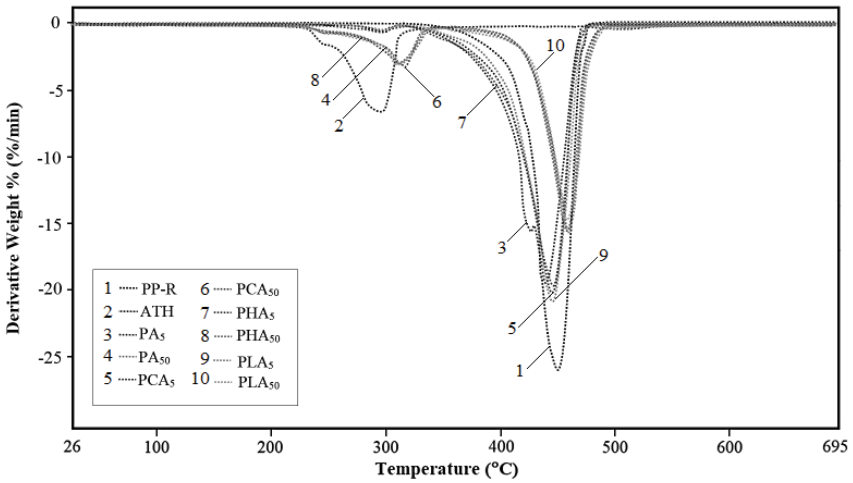

Fig. 2. DTG curves of composites based of PP-R/ATH.

DSC curves are shown in Fig. 3. DSC was performed to understand the thermal properties of composites containing various compatibilizers and to evaluate the influence of ATH loading on the crystallite melting pattern. The T_m of PP-R/ATH based composites are tabulated in Table II. Based on DSC data, we can say that the introduction of 5 wt. % ATH into PP-R with and without compatibilizers slightly affect the melting onset temperature; *i.e.*, the melting peak temperature increased from 145 °C for PP-R to 146 °C. This increase in melting temperature can be explained by the effect of a heterogeneous nucleation center, which makes it possible to obtain polymer composites with a fine-spherulitic supramolecular structure.[27] At 50 wt. % ATH, a slight shift in the melting temperature towards lower temperatures is observed, which may be associated with the formation of simple rod-shaped crystals, which affect the decrease in their melting temperature. The nucleation effect is effective at low amount (5 wt. %) of ATH. At a higher amount (50 wt.%), the simultaneous formation of a large number of particles cannot effectively induce heterogeneous nucleation centers that contribute to the formation of fine spherulite formations. Apparently, with an increase in the ATH content, there is a decrease in the enthalpy of melting and consequently, the degree of crystallinity of highly filled composites. The melting enthalpy shows a maximum value at 5 wt. % of ATH: PA_5 – 70.9170 J/g, PCA_5 – 64.2156 J/g, PHA_5 – 53.8289 J/g, PLA_5 – 68.7304 J/g. This may indicate that the uniform distribution of filler particles contributes to the formation of a more ordered structure. With an increase in the amount of ATH to 50 wt. % this value decreased to a minimum: PA_{50} – 48.7037 J/g, PCA_{50} – 48.2213 J/g and 25.4625 J/g, PHA_{50} – 37.3984 J/g, PLA_{50} – 34.1302 J/g. It should be noted that the value of this indicator for PP-R was equal to 56.6878 J/g. This indicates partial amor-

phization of the polymer composite. The supramolecular structure of the samples with a lower content of filler is characterized by the formation of a spherulitic structure, and with an increase in concentration, loosening and disordering of the structure ("amorphization") occurs.[28]

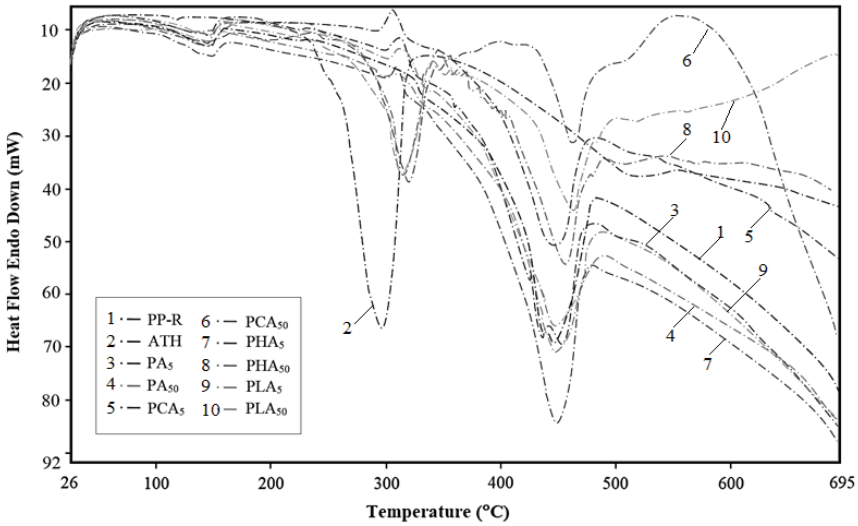

Fig. 3. DSC curves of composites based of PP-R/ATH.

During melting, ATH particles and the PP-R matrix are subject to the same thermal flow. At a lower ATH content (5 wt.%), this amount of thermal energy is quite sufficient for the decomposition of ATH. At a high ATH content (50 wt. %) relative to the PP-R matrix, the decomposition process slows down due to the shielding of the thermal effect by a large number of ATH particles, which leads to higher thermal stability of the composite. If we analyze the influence of the compatibilizer, we can establish that in its presence the enthalpy of melting of the composites becomes comparatively lower. This effect can be associated with an increase in the adhesive contact between the surface of the filler particles and the macrochains of the polymer matrix.

As can be seen from the data presented in Fig. 3 and in Table II, in contrast to the other samples, two melting peaks were observed for the PCA_{50} composite. In all likelihood, the appearance of two melting peaks may be the result of sequential polymorphism. In other words, this can be interpreted as the fact that the supramolecular structure of the composite is formed by polystructural formations with varying degrees of perfection of the crystalline phase.[29]

It is known that polymeric materials are characterized by a significant dependence of mechanical properties on temperature, which is determined by the structural features of high-molecular compounds. Therefore, the problem of stu-

dying the deformation characteristics of polymers depending on temperature is one of the important features of the thermomechanical behavior of polymers. The results of these studies are very useful in assessing the processing capabilities of polymers into products. Using thermomechanical curves, it is possible to estimate the first-order phase transition (softening temperature), as well as the behavior of composites in solid, highly elastic and viscous-flow states. Thermomechanical analysis allows us to establish the nature of the change in temperature transition from one physical state to another, which provides important information when choosing the modes of processing and operation of these materials. The obtained experimental data are presented in Fig. 4 (a, b, c and d) in the form of thermomechanical curves showing the dependence of deformation on temperature depending on the ATH content.

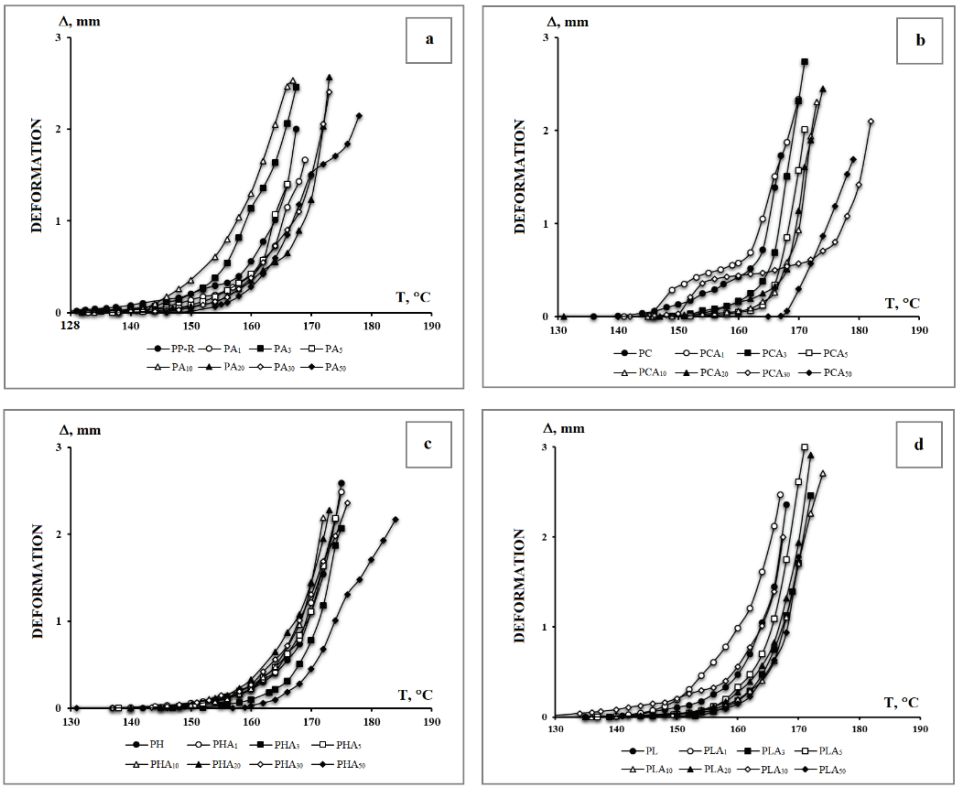

Fig. 4. The influence of ATH content on thermomechanical curves of the dependence of deformation on temperature.

From a comparative analysis of the curves in these figures, it can be seen that the presented thermomechanical curves have practically the same regularity of changes in deformation from temperature. The difference is manifested in the

change in phase transition temperature. Above softening temperatures, intensive development of deformation is observed, associated with the melting of the crystalline phase of the polymer matrix and its transition to a viscous flow state. This is a state characterized by relatively free movement of macromolecules or their segments in the melt relative to each other under the influence of a constant load.

Analyzing the influence of the amount of ATH on the regularity of changes in thermomechanical curves, it becomes obvious that with an increase in the filler content, a certain slowdown in the deformation process in the region of the viscous flow state is observed. Analysis of the given thermomechanical curves shows that the studied composites based on PP-R/ATH are characterized by two defined regions: solid and viscous-flow. With an increase in ATH concentration from 1.0 to 50 wt. %, the softening onset temperature increases from 128 to 146 °C (Table III).

TABLE III. Dependence of softening temperature (°C)on the content of PP-R/ATH based composites

Amount of ATH wt.%	Composite			
	PP-R/ATH	PP-R/PPC-g--MAH/ATH	PP-R/PPH-g--MAH/ATH	PP-R/LIBAID T-2/ATH
0	128	136	142	135
1	133	141	137	137
3	133	146	147	139
5	134	146	138	137
10	134	146	140	136
20	138	147	140	135
30	138	147	137	128
50	146	165	157	139

Similar results were obtained by studying thermomechanical properties of PP-R/PPC-g-MAH/ATH (Fig. 4b). When introducing ATH, a noticeable shift in the softening onset temperature is observed from 136 to 165 °C. A slight increase in the softening onset temperature and a shift of the curves to high temperatures is explained by the fact that with PPC-g-MAH, a significantly higher adhesion interaction between the polymer and the filler is ensured. Due to increased interaction between the polymer and the filler, an interphase zone appears with structural characteristics different from those of the matrix. As a result, during heat transfer impeding the thermal movement of macromolecules and their segments, which manifests itself in a decrease in deformability and an increase in softening onset temperatures. When filling PP-R/PPC-g-MAH with ATH, deformability decreases, which may be due to increased adhesive interaction between components. Some distinctive features are observed in the thermomechanical curves of PCA_1 and PCA_{30} composites. This difference manifests itself mainly in the area of deformations in the temperature range from 149 to 162 °C for PCA_1 and from

154 to 174 °C for the PCA_{30} composition, which, apparently, can be associated with partial amorphization of the structure of the mixture.

The results of thermomechanical analysis showed approximately the same nature of changes in thermomechanical curves for composites based on PP-R/ /PPH-g-MAH/ATH (Fig. 4c) and PP-R/LIBAID T-2/ATH (Fig. 4d) with PP-R/ /ATH. Fig. 4c shows the thermomechanical curves of PP-R/PPH-g-MAH/ATH composites. As can be seen from this figure, the tested samples are not subject to deformation over a wide temperature range. Only after a temperature of 142 °C does the process of softening of the composites begin. For PP-R/LIBAID T-2/ /ATH composites, this temperature is equal to 135 °C (Fig. 4d).

CONCLUSION

In the present study, a thermophysical and thermomechanical properties study has been done for a PP-R/ATH composites with 3 types of commercial grade compatibilizers and different content of ATH. Based on the results, the following conclusions were drawn from the study:

1. Thermophysical properties of obtained composites were analyzed using differential scanning calorimetry, thermogravimetric analysis, derivative thermogravimetry and thermomechanical curves. Results from the above thermal analysis showed that incorporation of ATH into PP-R and PP-R/compatibilizer led to improved thermal characteristics, with a lower maximum mass loss rate and higher residue.

2. An increase in the ATH content in the composite leads to a change in the structure of the PP-R and PP-R/compatibilizer and a decrease in its melting temperature. The melting enthalpy of composites containing compatibilizers was lower than composites without compatibilizers and this effect was associated with good interfacial adhesion and better dispersion of ATH. The difference in the effect of the type of compatibilizer on the thermal properties of the PP-R/ /compatibilizer/ATH composite is manifested in the higher amount of filler.

3. With the increase in the ATH amount, an increase in the softening temperature of the composites based on PP-R/ATH and PP-R/PPC-g-MAH/ATH was observed, while a wave-like change was observed for PP-R/PPH-g-MAH/ /ATH and PP-R/LIBAID T-2/ATH.

И З В О Д

УТИЦАЈ РАЗЛИЧИТИХ КОМПАТИБИЛИЗАТОРА И КОЛИЧИНЕ АЛУМИНИЈУМ-ХИДРОКСИДА НА ТЕРМОФИЗИЧКА И ТЕРМОМЕХАНИЧКА СВОЈСТВА КОМПОЗИТА НА БАЗИ СЛУЧАЈНОГ КОПОЛИМЕРА ПОЛИПРОПИЛЕНА И АЛУМИНИЈУМ-ХИДРОКСИДА

FATIMA MUSTAFAYEVA[1], NAJAF KAKHRAMANOV[1], GALINA MARTYNOVA[2] и NELI KOSEVA[3]

[1]Institute of Polymer Materials of Ministry of Science and Education Republic of Azerbaijan, S. Vurgun Str. 124, Sumgait, Republic of Azerbaijan, [2]Institute of Geology and Geophysics of Ministry of Science and Education Republic of Azerbaijan, H. Javid av. 119, Baku, Republic of Azerbaijan и [3]Institute of Polymers, Bulgarian Academy of Sciences, ul. "Akad. Georgi Bonchev" 103, 1113 Geo Milev, Sofia, Bulgaria

Ова студија истражује утицај три различита комерцијално доступна компатибилизатора (DuPont™ Fusabond® P353 polymer modifier, Exxelor™ PO 1020, LIBAID T-2) на термичка својства композита на бази случајног кополимера полипропилена и алуминијум-хидроксида (PP-R/ATH). Разматра се утицај поменутих компатибилизатора, као и количине ATH, на термофизичка и термомеханичка својства ових композита. Термичка својства добијених композита анализирана су коришћењем диференцијалне скенирајуће калориметрије, термогравиметријске анализе, деривативне термогравиметрије и термомеханичких кривих. Резултати студије показују да садржај ATH у PP-R матрици, како у присуству компатибилизатора, тако и без њега, значајно утиче на промене термофизичких и термомеханичких карактеристика. Са повећањем садржаја пунила, уочено је: повећање количине остатка при 700 °C, температуре при максималној брзини губитка масе, температуре разлагања од 50 %, као и смањење температуре почетка деградације. Утицај коришћених компатибилизатора на температуру топљења није био значајан при ниском садржају ATH (5 мас. %), док су при високом садржају пунила (50 мас. %) добијени различити резултати. Композити са компатибилизатором имали су ниже енталпије топљења у поређењу са онима без компатибилизатора.

(Примљено 12. новембра 2024, ревидирано 3. фебруара, прихваћено 19. марта 2024)

REFERENCES

1. H. Raghuram, M. Seier, T. Koch, M. P. Jones, V.-M. Archodoulaki, *Sustain. Mater. Technol*. **8** (2023) e00745 (https://doi.org/10.1016/j.susmat.2023.e00745)
2. F. Seidi, E. Movahedifar, G. Naderi, V. Akbari, F. Ducos, R. Shamsi, H. Vahabi, M. R. Saeb, *Polymers* **12** (2020) 1701 (https://doi.org/10.3390/polym12081701)
3. W. Zhao, C. Kumar Kundu, Z. Li, X. Li, Z. Zhang, *Compos., A* **145** (2021) 106382 (https://doi.org/10.1016/j.compositesa.2021.106382)
4. R. A. Mensah, V. Shanmugam, S. Narayanan, J. S. Renner, K. Babu, R. E. Neisiany, M. Försth, G. Sas, O. Das, *Polym. Test.* **108** (2022) 107511 (https://doi.org/10.1016/j.polymertesting.2022.107511)
5. Y. Ma, L. Hu, Y. Huang, F. Chu, X. Zhang, Z. Guo, S. Jia, N. Zhu, Y. Chen, Y. Gu, *Int. J. Heat Mass. Transf.* **201** (2023) 123505 (https://doi.org/10.1016/j.ijheatmasstransfer.2022.123505)
6. J. Xiao, J. Hobson, A. Ghosh, M. Haranczyk, D.-Y. Wang, *Compos. Commun.* **40** (2023) 101593 (https://doi.org/10.1016/j.coco.2023.101593)
7. A. P. Basnayake, J. P. Hidalgo, M. T. Heitzmann. *Construct. Build. Mater.* **304** (2021) 124540 (https://doi.org/10.1016/j.conbuildmat.2021.124540)
8. J. Z. Liang, C. Y. Tang, Y. J. Zhang, *J. Appl. Polym. Sci.* **118** (2010) 332 (https://doi.org/10.1002/app.32370)

9. K. Zhu, Y. Yang, C. Lin, Q. Wang, D. Ye, H. Jiang, K. Wu, *ACS Omega* **9 (**2024) 2803 (https://doi.org/10.1021/acsomega.3c08094)
10. N. Pérez, X. L. Qi, S. Nie, P. Acuña, M. J. Chen, D. Y. Wang, *Materials (Basel)* **12** (2019) 152 (https://doi.org/10.3390/ma12010152)
11. N. Samat, N. Zulkapali, Z. Halim, Z. Ahmad, A. I. H. D. Habibah, *Adv. Mater. Res.* **1115** (2015) 402 (https://doi.org/10.4028/www.scientific.net/AMR.1115.402)
12. S. Elbasuney, *Powder Technol.* **305** (2017) 538 (https://doi.org/10.1016/j.powtec.2016.10.038)
13. A. ur R. Shah, D.-W. Lee, Y.-Q. Wang, A. Wasy, K. C. Ham, K. Jayaraman, B.-S. Kim, J.-I. Song, *Trans. Nonferrous Met. Soc. China* **24** (2014) s81 (https://doi.org/10.1016/S1003-6326(14)63292-1)
14. M. R. Parida, S. Mohanty, M. Biswal, S. N. Kayak, S. Rai, *J. Therm. Anal. Calorim.* **148** (2023) 807 (https://doi.org/10.1007/s10973-022-11851-1)
15. F. A. Sabaruddin, N. Samat, A. I. H. D. Habibah, *Adv. Mater. Res.* **1115** (2015) 406 (https://doi.org/10.4028/www.scientific.net/AMR.1115.406)
16. F. N. Joynal Abedin, H. A. Hamid, A. F. M. Alkarkhi, S. S. A. Amr, N. A. Khalil, A. N. Ahmad Yahaya, M. S. Hossain, A. Hassan, M. Zulkifli, *Polymers* **13** (2021) 3180 (https://doi.org/10.3390/polym13183180)
17. K. Bedjaoui, R. Krache, A. Marcos-Fernández, M. Guessoum, *Mat. Res. Express* **6** (2019) 105334 (https://doi.org/10.1088/2053-1591/ab38e7)
18. M. K. Chang, H. C. Lee, *Int. Comm. Heat Mass Trans.* **67** (2015) 21 (https://doi.org/10.1016/j.icheatmasstransfer.2015.06.016)
19. R. Jeziorska, A. Szadkowska, M. Zielecka, M. Wenda, B. Kepska, *Poly. Degrad. Stab.* **145** (2017) 70 (https://doi.org/10.1016/j.polymdegradstab.2017.06.007)
20. N. Eszer, Z. Ishak, *IOP Conf. Series: Mat. Sci. Eng.* **368** (2018) 012017 (https://doi.org/10.1088/1757-899X/368/1/012017)
21. F. A. Mustafayeva, N. T. Kakhramanov, I. A. Ismailov, *Inorg. Mater. Appl. Res.* **13** (2022) 225 (https://doi.org/10.1134/S2075113322010282)
22. N. T. Kakhramanov, Kh. V. Allahverdiyeva, *Russ. J. Appl. Chem.* **96** (2023) 441 (https://doi.org/10.1134/S1070427223040079)
23. H. Yang, Z. Cai, H. Liu, Z. Cao, Y. Xia, W. Ma, F. Gong, G. Tao, C. Liuet, *J. Polym. Sci.* **58** (2020) 903 (https://doi.org/10.1002/pol.20190210)
24. N. H. Thi, T. N. Nguyen, H. T. Oanh, N. T. T. Trang, D. Q. Tham, H. T. Nguyen, T. V. Nguyen, M. H. Hoang, *J. Appl. Polym. Sci.* **138** (2020) 50317 (https://doi.org/10.1002/app.50317)
25. H.-K. Peng, X. X. Wang, T.-T. Li, C.-W. Lou, Y.T. Wang, J.-H. Lin, *Polym. Adv. Technol*. **30** (2019) 2045 (https://doi.org/10.1002/pat.4637)
26. E. Bachtiar, K. Kurkowiak, L. Yan, B. Kasal, T. Kolb, *Polymers*. **11** (2019) 699 (https://doi.org/10.3390/polym11040699)
27. F. Mustafayeva, N. Kakhramanov, Kh. Allahverdiyeva, *Polyolef. J.* **11** (2024) 243 (https://doi.org/10.22063/poj.2024.35560.1326)
28. S. N. Danilova, E. S. Efimova, N. N. Lazareva, A. A. Okhlopkova, A. G. Tuisov, *Polzunovskiy vestnik* **1** (2024) 197 (https://doi.org/10.25712/ASTU.2072-8921.2024.01.024)
29. Md. Khairul Hassan Bhuiyan, Md. Mahbubur Rahman, Md. Forhad Mina, Muhammad Remanul Islam, Md. Abdul Gafur, A. Begum, *Compos., A* **52** (2013) 70 (https://doi.org/10.1016/j.compositesa.2013.05.011).

Journal of the Serbian Chemical Society
JSCS@tmf.bg.ac.rs • www.shd.org.rs/JSCS
J. Serb. Chem. Soc. 90 (6) 803–821 (2025)
JSCS–5422
Original scientific paper
Published 24 June, 2025

Microplastic accumulation and reduction in shellfish (*Polymesoda bengalensis*) using NaCl solution

DESWATI DESWATI[1]*, EMRIADI EMRIADI[1], SELFI MONICA AURA[1], WIYA ELSA FITRI[2], SUPARNO SUPARNO[3] and ADEWIRLI PUTRA[4]

[1]*Department of Chemistry, Faculty of Mathematics and Natural Science andalas University, Padang, 25163, Indonesia,* [2]*Department of Public Health, Syedza Saintika University, Padang, 25132, Indonesia,* [3]*Departement of Fisheries Resources Utilization, Faculty of Fisheries and Marine Sciences, Bung Hatta University, Padang, 25133, Indonesia and* [4]*Department of Medical Laboratory Technology, Syedza Saintika University, Padang, 25132, Indonesia*

(Received 25 April 2024, revised 14 March, accepted 11 April 2025)

Abstract: This study investigates microplastic (MP) contamination in shellfish (*Polymesoda bengalensis*) and evaluates the effectiveness of NaCl treatment in reducing MP levels in consumed shellfish. Samples were collected from three estuaries in West Sumatra, Indonesia: Batang Arau, Bungo Pasang and North Punggasan. The samples were analyzed using trinocular microscopy and attenuated total reflectance-Fourier transform infrared (ATR-FTIR) to quantify MP abundance and identify polymer types. MP concentrations ranged between 750–1000 particles/kg in shellfish and 400–500 particles/kg in sediments, with Batang Arau exhibiting the highest levels. The predominant MP forms detected were fragments (82.36 %), films (13.72 %) and fibers (3.92 %), with sizes primarily between 100–300 μm. The primary polymers identified included polyvinyl chloride (PVC), polyamide (PA) and polyethylene terephthalate (PET). A series of treatments using NaCl solutions at varying concentrations (10, 20 and 30 %) and immersion durations (10, 20 and 30 min) demonstrated that a 30 % NaCl solution for 30 min effectively reduced MP levels by 85 %, decreasing MP concentration in shellfish flesh to 150 particles/kg. These findings highlight the potential of NaCl treatment as a cost-effective method for reducing MP contamination in shellfish, contributing to improved seafood safety and providing insights into MP pollution management in aquatic ecosystems.

Keywords: bioindicators; microplastics; salt solutions; shellfish; types of polymers.

* Corresponding author. E-mail: deswati@sci.unand.ac.id
https://doi.org/10.2298/JSC240411023D

INTRODUCTION

Plastic is a synthetic organic polymer often used because it is light, cheap and versatile, for example, in food packaging, medical devices, medicines and construction tools. The resulting plastic waste is a problem that attracts public attention because of its slow decomposition rate. In Indonesia, plastic waste is estimated to reach 187.2 Mt/year.[1] Plastics are composed of long-chain molecules called macromolecules. Plastic cannot decompose quickly because of its long chain of constituents. Plastic particles come in various sizes, including microplastic (MP). MPs are particles less than 5 mm in size. This MP can be formed from large plastic tears caused by biota bites and degradation due to sunlight.[2,3]

MPs are divided into two based on their origin, namely primary MP and secondary MP. Primary MP refer to MP that are intentionally produced in microscopic sizes, while secondary MP are MP that are formed through fragmentation of large plastics.[4] MPs can spread into aquatic environments, including rivers, lakes, seas, air and soil. They are an environmental problem because of their ability to absorb chemical pollutants and because they can enter the food chain, from small organisms to humans. MPs float and accumulate in sediments, allowing these particles to be accidentally ingested by marine organisms. Shellfish, as filter feeder organisms, have a way of eating by filtering plankton so that microplastic particles that float and settle in the sediment will accumulate in the shellfish's body through the activity of filtering these particles while eating.[5–7]

Shellfishes are mollusks that are sessile, filter feeders and more tolerant of changes in environmental conditions.[8,9] These filter-feeder organisms can be used as monitoring agents (bio-monitoring) of the aquatic environment because they settle at the bottom of the water and are directly exposed to contaminants. These properties support environmental monitoring, so shellfish are widely used as indicators of microplastic pollution.[10] Several previous studies have been conducted to identify MP in mussels in various waters, including 22 mussels in coastal China. The average abundance of MP obtained was 2200 particles/kg. Then shellfish in UK waters. The abundance of MP obtained ranged from 700––2900 particles/kg of shellfish.[11] Furthermore, for 25 mussels in China Beach, the MP abundance obtained ranged from 1520–5360 particles/kg of mussels[12] and research on 4 species of mussels in China, the MP abundance obtained ranged from 300–201000 particles/kg.[13] Later, MP studied mussels and sediments in Batang Arau, Bungo Pasang and Padang Sarai River Estuary, West Sumatra, Indonesia.

Humans widely consume shellfish because they have high economic value and are very good for consumption.[11] However, their vulnerability to the uptake of pollutants allows MP to enter the food chain and accumulate at higher trophic levels, becoming a concern for marine predators and human health.[14] Therefore, a strategy is needed to reduce MP pollutants in shellfish by using NaCl salt solutions.

NaCl salt is thought to reduce MP in shellfish by exploiting the difference in density between the plastic particles and the NaCl salt solution. Interaction with the NaCl salt solution causes low-density pollutants to rise to the surface of the NaCl salt solution. NaCl can attract particles along with water and then float them to the surface if the density of the particles is lower than NaCl. Previous research on using NaCl salt to reduce MP abundance in blood clams (*Tegillarca granosa*) has also been reported.[15] Based on the explanation above, research was conducted to analyze the abundance of MP in shellfish and sediment from three different locations in the waters of West Sumatra, Indonesia and study the effect of variations in the concentration of NaCl salt solution and optimal soaking time to reduce the abundance of MP in consumed shellfish. by society. MP identification begins[16] with MP separation to obtain MP particles. Next, visual identification (size and shape) and abundance of MP were carried out using a microscope and continued with a characterization of the MP functional group types using ATR--FTIR.

EXPERIMENTAL

Materials

The materials used were doubly distilled water, which served as a purified solvent to prevent contamination during sample preparation and microplastic (MP) extraction. 30 % H_2O_2 was utilized to oxidize and break down organic matter in samples, ensuring that only MPs remained for analysis. 25 % NaCl and table salt solution with zero or minimum MP were employed for density separation, exploiting the difference in density between MPs and the saline solution to facilitate particle flotation and isolation. Whatman filter paper no. 42 was selected for its fine pore size, enabling effective filtration of MPs without losing smaller particles. Shellfish samples were the primary subject of study for MP bioaccumulation, while sediment samples served to assess environmental MP load and its correlation to bioaccumulation in shellfish. Aluminum foil was used to cover samples during heating or storage, preventing airborne contamination.

Instruments

The instruments used were a food processor, which ground shellfish meat into smaller particles to enhance the efficiency of MP extraction. A cooler box maintained the integrity of samples during field collection and transport, preserving their original state before analysis. Plastic ziplock bags were used for secure sample storage to avoid any cross-contamination. A camera (Realme 6) documented each stage of the study, providing visual records for sample collection and laboratory procedures. A scalpel carefully opened shellfish shells, preserving the internal tissue for analysis. A metal shovel collected sediment samples, ensuring consistency in sample depth and area. A 5 mm filter was used to sieve and homogenize sediment samples. Various glassware was employed for handling, storing and processing samples. An oven (Memmert, Schwabach, Germany) dried sediment and activated reagents at consistent temperatures. A vacuum pump facilitated efficient sample filtration and an analytical balance provided precise measurements of sample weight. ATR-FTIR (Perkin Elmer, Waltham, MA, USA) identified polymer types of MPs based on spectral characteristics and a trinocular mic-

roscope (Optika B-350, Bergamo, Italy) enabled the visual identification of MP shapes and sizes, critical to characterizing particle morphology.

Sample preparation

Shellfish samples were frozen in a freezer at –20 °C for two days. After freezing, the shell is opened using surgical tools.[11] Sediment samples were homogenized with the help of a 5 mm mess filter. Wet sediment (100 g) was weighed using an analytical balance and dried in an oven for two days at a temperature of 65 °C.

Sample separation

20 g of dried shellfish meat was weighed and ground using a food processor, then added with 30 % H_2O_2 solution, 300 mL each. The sample was homogenized, heated for 24 h at 65 °C and then covered with aluminum foil. Next, the solution was heated and left at room temperature in the oven for 24 h. 200 mL of NaCl solution (250 g L^{-1}) was added to the sample, homogenized using a magnetic stirrer and left for 24 h.[17] The solution was then filtered through the supernatant using Whatman No. 42 filter paper with the help of a vacuum pump. MP filtered on Whatman paper are then identified visually (shape and size) with a microscope and then calculated in abundance and type of polymer using FTIR.

The dry sediment sample was weighed as much as 20 g and put into a beaker. 300 mL of 30 % H_2O_2 solution was added and the solution was heated at 65 °C for 24 h using an oven. Then 200 mL of NaCl was added and homogenized using a magnetic stirrer, covered with aluminum and left for 24 h. Next, it was filtered using Whatman filter paper No. 42. MP that have been filtered on Whatman paper are then identified visually (shape and size) using a microscope and then the abundance and type of polymer are calculated using FTIR.[17-21]

Soaking in NaCl salt solution

Soaking in a salt solution utilizes the density of NaCl and MP and the flow rate of salt water through the meat's pores to separate the MP from the shellfish meat. A total of 20 g of shellfish meat that had been frozen was slowly put into a 250 mL beaker and weighed. Then, it is put in solutions with various concentrations (0, 10, 20 and 30 %). The soaking time was varied (10, 20 and 30 min). Particles with a lighter density, for example, MP, will float to the surface of the solution. Then, the shellfish meat is separated from the solution and ground using a food processor.[22]

Shellfish meat (20 g) was weighed and ground using a food processor and then 300 mL of 30 % H_2O_2 solution was added. The sample was homogenized, heated for 24 h at 65 °C and then covered with aluminum foil. After heating, the solution was left at room temperature for 24 h. 200 mL of NaCl solution (250 g L^{-1}) was added to the sample, homogenized using a magnetic stirrer and left for 24 h.[17] The solution was then filtered through the supernatant using Whatman filter paper No. 42 with the help of a vacuum pump. MP filtered on Whatman paper are then identified visually (shape and size) using a microscope and then the abundance and type of polymer are calculated using FTIR.

Microplastic identification

Visual identification, such as shape and size, was done using a B-350 Optika trinocular microscope with 100× magnification. Next, the MP abundance in shellfish and sediment was calculated using the formula.[23-25] Identification of MP polymer types using ATR-FTIR:

$$K = \frac{n}{m} \tag{1}$$

where *K*= MP abundance (particles/kg), *n* = number of MP (particles) and *m* = dry weight of sample (kg).

Experimental design

The experimental design was a completely randomized (factorial CRD) design. The factors used consist of two factors, namely NaCl concentration (%) and soaking time (min). There are three levels of NaCl concentration, namely 10, 20 and 30 %. There are three soaking times, namely 10, 20 and 30 min. Data on the effect of the two factors and interactions between factors on the abundance of shellfish MP were analyzed using analysis of variance (ANOVA) and a Duncan test was carried out to analyze the differences. This analysis used a significance level of 0.05 with SPSS v26 software.

RESULTS AND DISCUSSION

Microplastic abundance

The identification of MP abundance in shellfish and sediment from the Batang Anai River Estuary, Bungo Pasang River Estuary and North Punggasan River Estuary, West Sumatra, Indonesia, can be seen in Fig. 1. The average MP abundance detected in shellfish ranged between 750±41 and 1000±71 particles/ /kg, whereas in sediment, it ranged between 400±108 and 500±82 particles/kg.

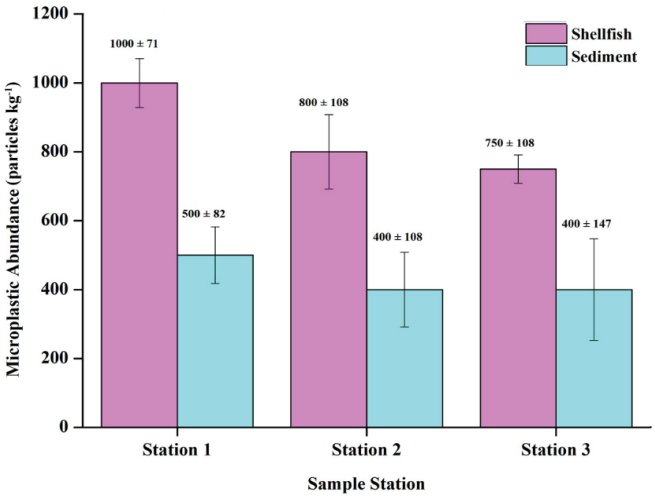

Fig. 1. Microplastic abundance (particles/kg) in shellfish and sediment samples (n=3).

In Fig. 1, it can be seen that the highest abundance of MP particles was found in shellfish samples (1000±71 particles/kg) and sediment (500±82 particles/kg) from station 1 (Batang Arau River Estuary). This is because the Batang Arau River Estuary is a tourist area busy with visitors, a densely populated residential area and a sea transportation area (such as fishing activities and ports) and the sampling location is close to the Fish Auction Place (FCP).

Generally, the higher the MP abundance in sediment, the higher the MP abundance in shellfish. The reduced abundance of MP in both sediment and shellfish at stations 2 and 3 is thought to be due to reduced disposal of plastic waste originating from household waste, fewer tourist visits and distance from sea transportation.[26,27]

Shellfish and sediments have a close relationship in marine geology and ecology. Shellfish are mollusks that generally live in sea waters. Conversely, sediment is small particles of rocks, minerals, dead organisms and other organic materials deposited on the bottom of water. Shellfish often play an important role in sediment formation and can influence the composition and structure of the sediments around them. Mussels and sediments have a close relationship that involves processes such as: 1) some types of shellfish, especially those with calcium carbonate shells, can contribute significantly to the formation of limestone; 2) shellfish generally live on the seabed or the substrate. During their lives, they can collect sediment from their surroundings. Some types of shellfish, such as oyster shells, use their gill organs to filter food particles from the water, resulting in sedimentation of surrounding particles; 3) several shellfish live with sediment on the seabed. Mussels may hide in sediment to protect themselves from predators or search for food; 4) shellfish are often an important part of marine ecosystems. They can interact with other organisms, including organisms that live in or around sediments, such as microorganisms, snails and macroalgae; 5) sediment pollution by chemicals or waste can harm the health of shellfish and sediment ecosystems; 6) several types of shellfish can be used as environmental indicators to evaluate water and sediment quality. They can show whether the environment is clean or polluted.[28]

Microplastic shape

The MP shape at three stations, both in shellfish and sediments, is dominated by fragments in the order fragment > film > fiber (Fig. 2). In this study, fragments dominated all sampling stations in shellfish and sediments because many macro plastics, such as plastic bottles, containers and other plastic packaging, can experience physical degradation due to exposure to UV light, temperature changes and friction. This decomposition process turns plastic into smaller fragments. Microplastics themselves can become smaller fragments due to environmental degradation processes. Exposure to UV light, oxidation and mechanical forces can cause MP to break down into smaller fragments. Abrasion is rubbing or scratching plastic on other objects, such as rocks, sand and other surfaces. In this process, small pieces can be separated from the plastic surface and become MP fragments.[19,29] Some plastic products, especially those susceptible to wear and tear and repeated use, may develop fragments during use. For example, car tires, brake pads and other plastic products can produce MP fragments due to friction and wear.

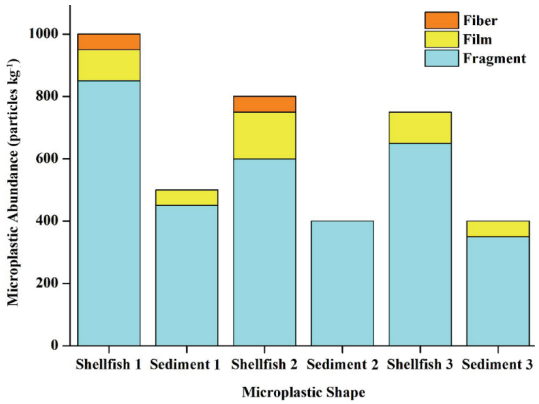

Fig. 2. Abundance of microplastic shapes in shellfish and sediment samples.

MPs in fragments are found more in shellfish than sediments for several reasons, including: 1) MPs often degrade into very small fragments, less than 5 mm. These particles are more likely to accumulate in shellfish tissue because they are similar in size to natural food particles that filter-feeding organisms, such as mussels, can filter; 2) shellfish are filter-feeder animals that eat plankton and small particles from the water. This filtering process makes shellfish susceptible to capturing MP in the water, including small fragments; 3) MPs can be widely distributed in the marine environment and reach various habitats, including seawater and sediment. However, shellfish often reside in shallow areas with higher MP concentrations; 4) shellfish often contact marine sediments while searching for food and burrowing on the sea floor. MP fragments can interact with sediments and shellfish that feed on sediments tend to incorporate MP into their bodies; 5) the chemical properties of MP can also influence how easily organisms absorb them. Some MP can absorb toxic chemical compounds from the surrounding environment, accumulating in organisms' tissues, including shellfish.[30]

Furthermore, in the second sequence, both shellfish and sediments were dominated by MP in the shape of films, except for sediments in the Bungo Pasang River Estuary (station 2), where no films were found. The film is thought to originate from the fragmentation of plastic bags and has a low density. The film is a type of secondary MP whose source comes from the fragmentation process of plastic packaging and plastic bags made from polyethylene polymer. Particle films also come from fragile plastic fragments.[31] Microbeads (pellets), MP in granular form, are one type of primary MP. Primary MP are made in microforms in beauty and hygiene products. MP microbeads usually come from polymers such as polyethylene, polystyrene and polymethyl methyl acrylate.[29] MP in pellet form is produced from raw materials from industrial activities, toiletries, soap and facial cleansers, while the foam is made from packaging and plastic bags. The form of fragments, films and fibers shows that the MP found in this study is a secondary MP formed through the photolysis process. At station 2, no film was

found in the sediment. It is suspected that a small amount of film has been consumed by shellfish and another possibility is the hydrodynamic process of water so that the current carries the MP in the sediment to other places.[32]

Fiber is only found in shellfish at stations 1 and 2. Fiber is a type of MP whose sources are nylon, polyvinyl and polypropylene. People use nylon to make clothes, carpets and ropes. Polyvinyl alcohol is usually used as a basic material for making fishing equipment, while polypropylene is often used to make carpets and ropes, which are widely used on ships.

Microplastic size

The results of the MP size study in shellfish and sediment at three sampling stations can be seen in Fig 3. Fig 3 shows that the abundance of shellfish and sediments based on MP size tends to be dominated by sizes 101–300 μm > 301––500 μm > 501–1000 μm and the other sizes are small in number. MPs with very small sizes, such as nanoplastics, can be easily inhaled, enter the respiratory systems of humans and animals and can be absorbed through the digestive tract. These particles can pose a health risk because they can penetrate tissues and organs in the body and have the potential to lose their buoyancy and sink in waters due to biofouling. Furthermore, differences in the size of MP waste are closely related to wind direction and speed,[33] the presence of biofouling[34] and hydrodynamic water conditions such as currents, waves and tides. Larger MP become trapped in larger living organisms such as fish, seabirds and marine mammals. However, MP with smaller sizes can easily enter organisms through contaminated food and water. Microplastics accumulating in organisms can cause dangerous effects, including organ damage, hormonal changes and reproductive disorders.

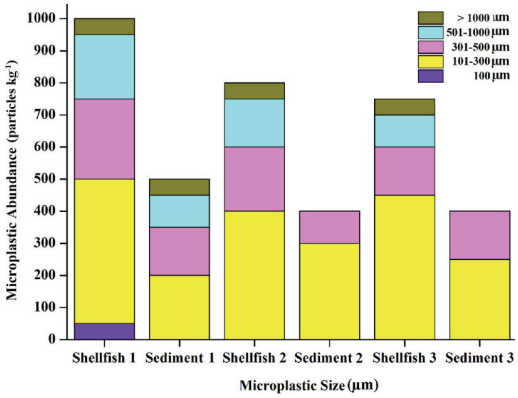

Fig. 3. Abundance of microplastic size in shellfish and sediment samples.

The size of the MP can directly affect its level of toxicity. Several studies have shown that smaller MP particles can contain harmful chemical compounds,

such as persistent organic pollutants (POPs), that can leach into the environment or the body of organisms. The content of these chemical compounds can cause poisoning and other negative impacts on living organisms.[35] MPs, especially large ones, can also act as vectors or carriers of other pollutants. MP can absorb toxic chemical compounds from the surrounding environment, such as pesticides or heavy metals and transport them to the organisms that consume them. Thus, MP may increase the exposure of organisms to harmful pollutants.

MPs are plastic fragments that are less than 5 mm in size. More specific MP sizes, such as 101–300 μm, fall into the very small MP category. The presence of MP in shellfish can be caused by various factors:[37] 1) filter-feeder organisms, such as mussels, may be more likely to consume MP measuring 101–300 μm because this size can match the particle size usually taken by these organisms; 2) biological processes in the body of mussels or other organisms may cause the separation or accumulation of MP of a certain size; 3) some MP may have certain chemical properties that make them more attractive to certain organisms. Chemical interactions between MP and filter feeder organisms can influence consumption rates; 4) small-sized MPs (*e.g.*, 101–300 μm) are more easily absorbed by shellfish through feeding and filtration processes, as these sizes resemble natural food particles. MPs of this size can become trapped in the tissue of shellfish flesh, making them more prone to accumulation within the organism. As shellfish continuously process water, they tend to filter out more of these smaller particles, leading to an increased amount of MP within their tissue; 5) once MPs are absorbed by the shellfish, these particles can become lodged within internal tissues, such as around the digestive organs or gills. Due to the continuous filtration system of shellfish, MPs accumulated within their bodies tend to persist and accumulate, especially in soft tissues like the flesh. This results in higher concentrations of MP within shellfish tissue compared to their surrounding environment; 6) sediment deposition processes in a region can influence the extent to which certain MP accumulate in organisms. Factors such as deposition velocity and sedimentation characteristics can play an important role.

Strategies for reducing microplastics in shellfish meat

Shellfish are marine organisms that are often the target of exposure to MP. Based on Fig. 4, the abundance of MP in shellfish before treatment (as control = treatment A) was 1000±71 particles/kg. The effects of MP in shellfish on their health and survival may pose a risk to higher organisms that consume them, including humans. Here are some of the effects of MP on shellfish: 1) shellfish tend to accumulate MP from the surrounding environment. These particles can penetrate the shellfish's body tissue, including vital organs such as gills and intestines; 2) MPs can affect the digestive system of shellfish. They can clog the intestines and hinder the digestive process, hindering nutrient absorption and potentially

causing health problems; 3) some types of MP contain toxic chemicals. When shellfish consume MP, these chemicals can escape and enter the shellfish's body, causing toxic effects.[37]

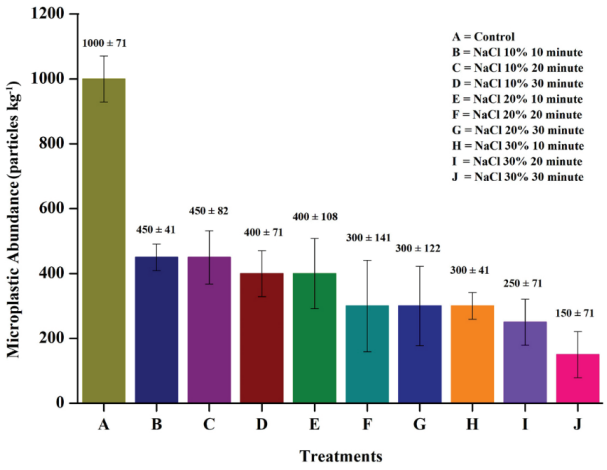

Fig. 4. Abundance of MP in shellfish meat with variations in soaking time (min) and salt concentration (%).

Therefore, to anticipate the negative impact of MP on shellfish, an experiment was carried out with a completely randomized factorial design combining two factors, namely NaCl salt solution (%) and soaking time (min), which can be seen in Table I and Fig. 4, showing that two factors, namely the concentration of NaCl solution (%) and soaking time (min) resulted in a decrease in the abundance of MP in shellfish meat.

TABLE I. Decrease in the amount of microplastics (MP shellfish abundance values) at NaCl concentration and soaking time; different superscript letters in the same row and column indicate significant differences ($p < 0.05$) in the decrease in MP abundance (ab is not significantly different from groups having a and/or b; abc is not significantly different from all groups; ac is not significantly different from groups a and/or c)

Soaking time (*B*), min	NaCl concentration (*A*), %		
	10	20	30
10	450 ± 41^{ab}	400 ± 108^{abc}	300 ± 41^{ac}
20	450 ± 82^{ab}	300 ± 141^{abc}	250 ± 71^{ac}
30	400 ± 71^{ab}	300 ± 122^{abc}	150 ± 71^{ac}

Based on Table I, the results of factorial testing show that NaCl concentration (Factor A) has a significant effect ($p < 0.05$) on reducing the abundance of MP in shellfish meat while soaking time (Factor *B*) and the interaction between NaCl concentration (Factor *A*) and soaking time (Factor *B*) had no significant

effect ($p > 0.05$) on reducing the abundance of shellfish MP. Duncan's further test showed that a 30 % NaCl solution and a soaking time of 30 min were optimal results, with a decrease in MP abundance in shellfish meat obtained by 150±71 particles/kg (85 %). In a 30 % NaCl solution and a soaking time of 20 min, MP particles were reduced to 250±71 particles/kg. 30 % NaCl solution and a soaking time of 10 min reduced the MP particles in shellfish meat to 300±41 particles/kg, as seen in Fig. 4.

Several mechanisms involve NaCl and MP: 1) NaCl can influence MP transport in the water environment. When water contains salt, the water's density increases, which can affect MP movement and transport. However, this effect may be small and influenced by various other factors; 2) although NaCl itself does not decompose MP, water containing salt can change the physical and chemical properties of MP. Environmental conditions involving salt, temperature and pressure can influence the MP degradation process; 3) ions and molecules in the salt solution can interact with the MP surface through the adsorption process. This can influence MP' surface properties, behavior and transport; 4) salts such as NaCl can be involved in MP biogeochemical cycles. These include interactions with living organisms, absorption by soil and the potential to enter the food chain.[33]

Based on Fig. 5, before treatment (control), there was MP in the form of films, fibers and fragments. However, after treatment, the MP concentration decreases as fragments, but the MP in films and fibers disappears. This shows that combining NaCl salt solution (%) and soaking time (min) effectively removes MP in films and fibers and reduces MP in fragments. The presence of salt, NaCl, in the environment, can influence the fate and transport of MPs. For example: 1) MPs can interact with salt through absorption and desorption processes. Salts in the environment can be absorbed onto the surface of MP, thereby affecting their

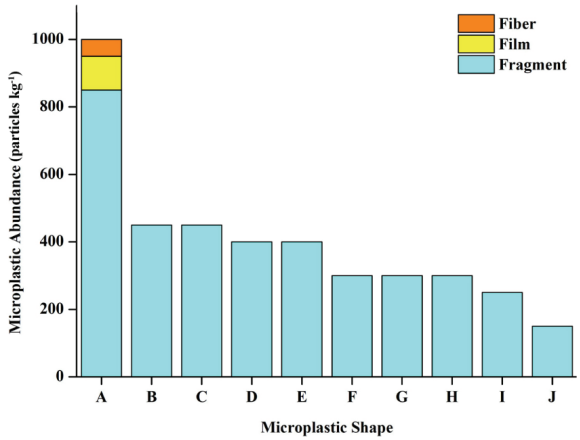

Fig. 5. Abundance of microplastic shapes in shellfish meat samples with variations in soaking time (min) and salt concentration (%).

properties and behavior; 2) the presence of salt can cause aggregation of MP particles. This aggregation can affect its transport in aquatic systems and its potential for ingestion by organisms.

The relationship between MP size, salt solution (%) and soaking time (min) involves various factors and interactions. From Fig. 6, as the salt solution (%) and soaking time (min) increase, the microplastic concentration decreases, some of the MP sizes disappear (≤ 100 μm, 501–1000 μm, > 1000 μm) and decrease (101–300 μm, 301–500 μm). When MP come into contact with a salt solution, several processes can occur: 1) the size of the MP can affect its buoyancy in salt water. Smaller MP may remain suspended in the water column for longer due to less settling due to gravity. Larger MP may settle more quickly; 2) MPs can aggregate or clump and particle size can influence this process. Smaller particles may aggregate more easily due to increased surface area and interparticle interactions; 3) the size of MP can influence their interactions with salt ions and other chemicals in solution. For example, smaller particles may have a greater surface area relative to their volume, thereby providing more opportunities for chemical reactions or adsorption of substances from the surrounding environment; 4) the size of MP can affect their bioavailability to marine organisms. Smaller particles may be more easily digested by smaller organisms, potentially leading to biomagnification through the food chain; 5) the size of MP can influence their transportation and distribution in water systems. Smaller particles may be more easily transported by water currents and distributed over a wider area.[40,41]

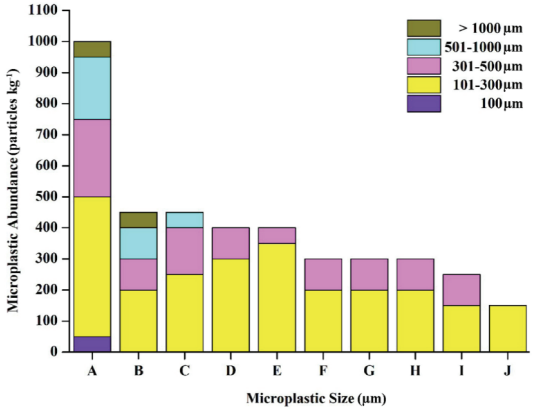

Fig. 6. Abundance of microplastic size in shellfish meat samples with variations in soaking time (min) and salt concentration (%).

Identification of MP polymer types

FTIR results before and after treatment, Fig. 7 shows the FTIR spectrum of standard polyvinylchloride (PVC) MP with MP spectra from shellfish without and with treatment with 30 % NaCl solution for 30 min. The FTIR results show that the type of polymer found is polyvinyl chloride (PVC), as evidenced by the

discovery of several main peaks characteristic of polyvinyl chloride polymers. In the standard PVC spectrum, the peak wave number was found at 2919.47 cm^{-1}, indicating C–H stretching vibrations (3000–2840 cm^{-1}); 1082.35 cm^{-1} indicates C–C bending vibration (1100–1000 cm^{-1}); and wave numbers of 686.17 and 617.41 cm^{-1} indicate C–Cl stretching vibrations (850–550 cm^{-1}). In the untreated MP spectrum, wave number peaks were found at 2916.46 and 2850.34 cm^{-1}, indicating C–H stretching vibrations; wave number 1048.78 cm^{-1} indicates C–C bending vibration; and the wave number 715.82 cm^{-1} indicates C–Cl stretching vibrations. Meanwhile, in the spectrum of MP in shellfish treated with 30 % NaCl solution for 30 min, a wave number peak was found at 2926.14 cm^{-1} indicating C–H stretching vibrations; wave number 1006.71 cm^{-1} indicates C–C bending vibration and the wave number 828.10 cm^{-1} indicates C–Cl stretching vibrations.[42,43]

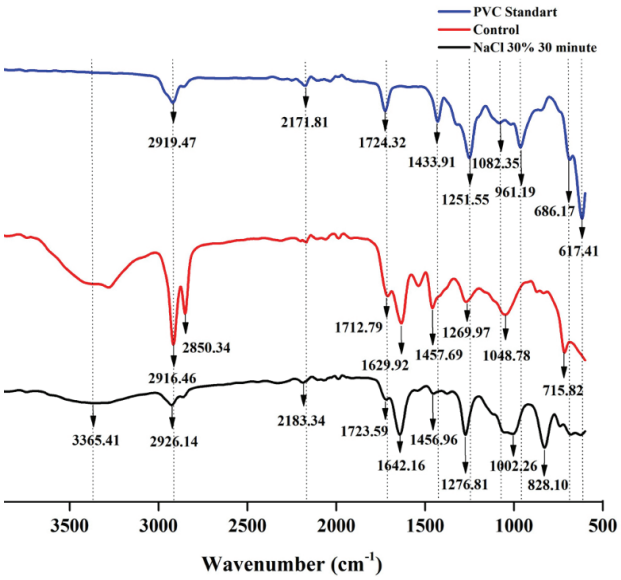

Fig. 7. Standard FTIR spectrum of PVC, without and with 30 % NaCl solution treatment for 30 min.

In Fig 7 and Table II, it can be seen that there is a missing peak (C–H vibration) in the spectrum of microplastics in shellfish treated with 30 % NaCl solution for 30 min compared to the microplastic spectrum in shellfish samples without treatment, such as C–H vibration. The peak spectrum of microplastics treated with 30 % NaCl solution for 30 min, such as C–H and C–O vibrations, tends to be weaker in intensity and not as sharp as the peaks of microplastics without treatment.

TABLE II. Wave number shift of PVC before and after treatment with NaCl

Wavenumber, cm^{-1}			Characteristics	Functional group
PVC standard	Control	NaCl 30 %, 30-min		
–	–	3365.41	N–H stretching	Aliphatic primary amine
2919.47	2916.46	2926.14	C–H stretching	Alkane
–	2850.34	–	C–H stretching	Alkane
2171.81	–	2183.34	S–C≡N stretching	Thiocyanate
1724.32	1712.79	1723.59	C=O stretching	Carboxylic acid
–	1629.92	1642.16	C=C stretching	Alkene
1433.91	1457.69	1456.96	C–H bending	Alkane
1251.55	1269.97	1276.81	C–O stretching	Aromatic ester
1082.35	1048.78	–	C–O stretching	Primary alcohol
961.19	–	1002.26	C=C bending	Alkene
–	–	828.10	C–Cl stretching	Halo compound
686.17	715.82	–	C=C bending	Alkene
617.41	–	–	C–Br stretching	Halo compound

Polyvinyl chloride (PVC) is a type of polymer that can be used in various products, including MP. Interactions between MP, NaCl and PVC functional groups may occur in certain environments, especially if the MP are exposed to water or electrolyte solutions. In PVC, the main functional group involved in the interaction is the polymer chain's chlorine group. PVC MP will open these groups to reaction with surrounding substances, including NaCl in solution.[44] Some potential interactions between NaCl and PVC on MP involve: 1) ion adsorption; Na^+ and Cl^- can be adsorbed on the surface of PVC MP through electrostatic interaction with the open chlorine groups on PVC; 2) ion exchange; Na^+ may exchange with other ions bound to PVC, affecting the surface properties of MP; 3) dissolution of PVC; under certain conditions, NaCl in solution can cause dissolution or degradation of PVC, especially if the solution concentration is high enough or other factors favor the chemical reaction; 4) physical changes; the interaction between NaCl and PVC can affect the physical properties of MP, such as surface structure, hardness or solubility.[22,44,46]

However, it is important to note that these interactions can be complex and highly dependent on specific environmental conditions, such as temperature, pH and NaCl concentration.[47]

In addition, the consequences of these interactions on MP and the environment still require further research. Fig. 8 compares the FTIR spectrum of MP between standard polyamide (PA) and the spectrum of MP in shellfish without and with treatment with 30 % NaCl solution for 30 min.

The FTIR results show that the type of polymer found is polyamide (PA), as evidenced by the discovery of several main peaks characteristic of polyamide polymers. In the standard PA MP spectrum, a wave number peak was found at 3292.84 cm^{-1} indicating N–H stretching vibrations (3330–3250 cm^{-1}); 2920.91

cm^{-1} indicates C–H stretching vibrations (3000–2840 cm^{-1}); wave number 1640.39 cm^{-1} indicates C=O stretching vibrations (1680–1630 cm^{-1}); wave numbers 1240.56 and 1029.94 cm^{-1} indicate C–N stretching vibrations (1250–1020 cm^{-1}). In the untreated MP spectrum, the wave number peak was found at 3277.24 cm^{-1} indicating N–H stretching vibrations; wave number 2924.31 cm^{-1} indicates C–H stretching vibrations; wave number 1637.05 cm^{-1} indicates C=O stretching vibrations (1680–1630 cm^{-1}); wave numbers 1247.35 and 1020.72 cm^{-1} indicate C–N stretching vibrations (1250–1020 cm^{-1}). In the spectrum of MP treated with 30 % NaCl solution for 30 min, the wave number peak was found at 3327.84 cm^{-1}, indicating N–H stretching vibrations; wave number 2892.39 cm^{-1} indicates C–H stretching vibrations; wave number 1320.44 cm^{-1} indicates C–N stretching vibrations; wave number 1020.56 cm^{-1} indicates C–N stretching vibrations.[26,27]

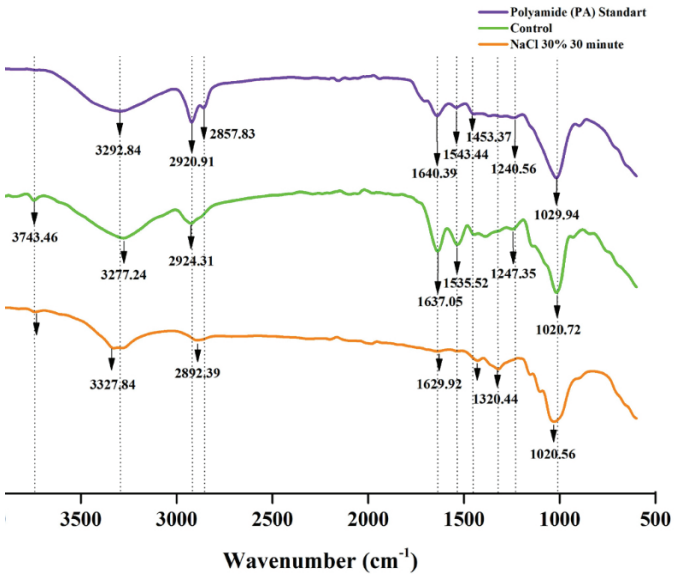

Fig. 8. FTIR spectrum of standard PA, without and with 30 % NaCl solution treatment for 30 min.

In Fig. 8 and Table III, it can be seen that there is a missing peak in the MP spectrum treated with 30 % NaCl solution for 30 min compared to the MP spectrum without treatment, such as C=O vibration. Apart from that, all the MP spectrum peaks in shellfish samples treated with 30 % NaCl solution for 30 min tended to be gentler and not as sharp as those without treatment, such as the N–H, C–H, C=O and C–N vibrations. This is due to the interaction between NaCl (table salt) and MP polyamide polymers through several mechanisms, especially due to their chemical properties. Polyamides are a group of polymers commonly

known as nylons and MP made from polyamides can interact with NaCl in water or other environments.

TABLE III. PA wave number shift before and after treatment with NaCl

Wavenumber, cm^{-1}			Characteristics	Functional group
PA standard	Control	NaCl 30%, 30 min		
–	3743.46	–	O–H stretching	Alcohol
3292.84	3277.24	3327.84	O–H stretching	Alcohol
2920.91	2924.31	2892.39	C–H stretching	Alkane
2857.83	–	–	C–H stretching	Alkane
1640.39	1637.05	1629.92	N–H bending	Amine
1543.44	1535.52	–	N–O stretching	Nitro compound
1453.37	–	1320.44	O–H bending	Phenol
1240.56	1247.35	–	C–N stretching	Amine
1029.94	1020.72	1020.56	C–O stretching	Vinyl ether

Some interactions that may occur are: 1) partial dissolution; salts such as NaCl can affect the partial dissolution of polyamide MP because NaCl dissolves in water. Its presence can modify the physical and chemical properties of the surrounding water. This can impact the solubility of polyamide MP; 2) ionic interactions; NaCl dissociates into Na^+ and Cl^- in water. These ions can interact with functional groups on polyamide that have certain charges. These ionic interactions can influence MP stability and physical properties; 3) ion adsorption; the surface of polyamide MP can adsorb ions. This adsorption can influence the surface properties and interaction of MP with their environment; 4) formation of hydrogen bonds; polyamides have amide groups that can form hydrogen bonds. The interaction between NaCl and the amide group can influence the structure and strength of polyamide MP.

CONCLUSION

The abundance of MP detected in shellfish ranged from (750 ± 41) and (1000 ± 71) particles/kg and the abundance of MP detected in sediment ranged from (400 ± 108) and (500 ± 82) particles/kg. The most frequently detected MP forms were fragments (82.36 %) > films (13.72 %) > fibers (3.92 %). The most commonly detected MP size was ≥ 100–300 μm (50.98 %). The types of polymers detected were polyvinylchloride (PVC), polyamide (PA) and polyethylene terephthalate (PET). Treatments varying the concentration of NaCl salt solution (0, 10, 20 and 30 %) and the effect of soaking time (10, 20 and 30 min) were carried out to reduce the abundance of MP in shellfish meat. The interaction of a NaCl concentration of 30 % and a soaking time of 30 min was the best result, with a reduction in MP abundance in shellfish meat of 85 %, from an MP abundance of 1000 to 150 particles/kg.

SUPPLEMENTARY MATERIAL

Additional data and information are available electronically at the pages of journal website: https://www.shd-pub.org.rs/index.php/JSCS/article/view/12882, or from the corresponding author on request.

ИЗВОД

АКУМУЛАЦИЈА И СМАЊЕЊЕ МИКРОПЛАСТИКЕ У ШКОЉКАМА (*Polymesoda bengalensis*) КОРИШЋЕЊЕМ РАСТВОРА NaCl

DESWATI DESWATI[1], EMRIADI EMRIADI[1], SELFI MONICA AURA[1], WIYA ELSA FITRI[2], SUPARNO SUPARNO[3] и ADEWIRLI PUTRA[4]

[1]Department of Chemistry, Faculty of Mathematics and Natural Science, Andalas University, Padang, 25163, Indonesia, [2]Department of Public Health, Syedza Saintika University, Padang, 25132, Indonesia, [3]Departement of Fisheries Resources Utilization, Faculty of Fisheries and Marine Sciences, Bung Hatta University, Padang, 25133, Indonesia и [4]Department of Medical Laboratory Technology, Syedza Saintika University, Padang, 25132, Indonesia

Ова студија истражује контаминацију микропластиком (MP) у шкољкама (*Polymesoda bengalensis*) и процењује ефикасност третмана NaCl у смањењу нивоа MP у конзумираним шкољкама. Узорци су прикупљени из три ушћа у Западној Суматри, Индонезија: Батанг Арау, Бунго Пасанг и Нортх Пунггасан. Узорци су анализирани коришћењем тринокуларне микроскопије и инфрацрвене спектроскопије са ослабљеном тоталном рефлексијом и Фуриеровом трансформацијом (ATR-FTIR), да би се квантификовала количина MP и идентификовали типови полимера. Концентрације MP су се кретале између 750—1000 честица/kg^{-1} у шкољкама и 400—500 честица/kg^{-1} у седиментима, при чему је Батанг Арау показао највише нивое. Међу откривеним облицима MP преовладавали су фрагменти (82,36 %), филмови (13,72 %) и влакна (3,92 %), са величинама између 100–300 μм. Примарни идентификовани полимери укључивали су поливинил хлорид (PVC), полиамид (PA) и полиетилен-терефталат (PET). Серија третмана коришћењем раствора NaCl различитих концентрација (10, 20 и 30 %) и времена потапања (10, 20 и 30 min) показала је да 30 % раствор NaCl током 30 min ефикасно смањује нивое MP за 85 %, смањујући концентрацију MP у месу шкољки на 150 честица/kg^{-1}. Ови налази наглашавају потенцијал третмана NaCl као исплативе методе за смањење контаминације MP у шкољкама, доприносећи побољшаној сигурности морских плодова и пружајући увид у управљање загађењем MP у воденим екосистемима.

(Примљено 25. априла 2024, ревидирано 14. марта, прихваћено 11. априла 2025)

REFERENCES

1. A. Nugraha, S. H. Sutjahjo, A. A. Amin, *J. Nat. Resour. Environ. Manage.* **8** (2018) 7 (https://doi.org/10.29244/jpsl.8.1.7-14)
2. C. B. Crawford, B. Quinn, in *Microplastic Pollution*, Elsevier, Amsterdam, 2017, p. 39 (https://doi.org/10.1016/b978-0-12-809406-8.00003-7)
3. M. Lončarski, A. Tubić, M. K. Isakovski, B. Jović, T. Apostolović, J. Nikić, J. Agbaba, *J. Serb. Chem. Soc.* **85** (2020) 697 (https://doi.org/10.2298/JSC190712124L)
4. L. Lin, L. Z. Zuo, J. P. Peng, L. Q. Cai, L. Fok, Y. Yan, H. X. Li, X. R. Xu, *Sci. Total Environ.* **644** (2018) 375 (https://doi.org/10.1016/j.scitotenv.2018.06.327)
5. A. A. Koelmans, N. H. Mohamed Nor, E. Hermsen, M. Kooi, S. M. Mintenig, J. De France, *Water Res.* **155** (2019) 410 (https://doi.org/10.1016/j.watres.2019.02.054)

6. A. Al Mamun, T. A. E. Prasetya, I. R. Dewi, M. Ahmad, *Sci. Total Environ.* **858** (2023) 159834 (https://doi.org/10.1016/j.scitotenv.2022.159834)
7. E. Mollova, E. Ivanova, S. Turmanova, A. Dimitrov, *J. Serb. Chem. Soc.* **89** (2024) 939 (https://doi.org/10.2298/JSC230516073M)
8. J. Ding, J. Li, C. Sun, F. Jiang, C. He, M. Zhang, P. Ju, N. X. Ding, *Sci. Total Environ.* **739** (2020) 139887 (https://doi.org/10.1016/j.scitotenv.2020.139887)
9. L. I. Bendell, E. LeCadre, W. Zhou, *PLoS One* **15** (2020) e0232879 (https://doi.org/10.1371/journal.pone.0232879)
10. A. F. Pérez, M. Ojeda, G. N. Rimondino, I. L. Chiesa, R. Di Mauro, C. C. Boy, J. A. Calcagno, *Mar. Pollut. Bull.* **161** (2020) 111753 (https://doi.org/10.1016/j.marpolbul.2020.111753)
11. J. Li, C. Green, A. Reynolds, H. Shi, *Environ. Pollut.* **241** (2018) 35 (https://doi.org/10.1016/j.envpol.2018.05.038)
12. X. Qu, L. Su, H. Li, M. Liang, H. Shi, *Sci. Total Environ.* **621** (2018) 679 (https://doi.org/10.1016/j.scitotenv.2017.11.284)
13. J. Ding, C. Sun, C. He, J. Li, P. Ju, F. Li, *Sci. Total Environ.* **782** (2021) 146830 (https://doi.org/10.1016/j.scitotenv.2021.146830)
14. S. Uddin, S. W. Fowler, T. Saeed, A. Naji, N. Al-Jandal, *Mar. Pollut. Bull.* **158** (2020) (https://doi.org/10.1016/j.marpolbul.2020.111374)
15. M. S. Arifin, J. Suprijanto, A. Ridlo, *J. Mar. Res.* **12** (2023) 447 (https://doi.org/10.14710/jmr.v12i3.36448)
16. S. M. Brander, V. C. Renick, M. M. Foley, C. Steele, M. Woo, A. Lusher, S. Carr, P. Helm, C. Box, S. Cherniak, R. C. Andrews, C. M. Rochman, *Appl. Spectrosc.* **74** (2020) 1099 (https://doi.org/10.1177/0003702820945713)
17. A. Mathalon, P. Hill, *Mar. Pollut. Bull.* **81** (2014) 69 (https://doi.org/10.1016/j.marpolbul.2014.02.018)
18. D. Deswati, B. Kurnia Hamzani, Y. Yusuf, W. E. Fitri, A. Putra, *Int. J. Environ. Anal. Chem.* **105** (2023) 636 (https://doi.org/10.1080/03067319.2023.2268523)
19. D. Deswati, O. N. Tetra, M. Hayati, A. Putra, W. E. Fitri, S. Suparno, H. Pardi, *AACL Bioflux* **16** (2023) 2601 (http://www.bioflux.com.ro/docs/2023.2601-2614.pdf)
20. D. Deswati, O. N. Tetra, U. Febriani, S. Suparno, H. Pardi, A. Putra, *AACL Bioflux* **16** (2023) 2765 (http://www.bioflux.com.ro/docs/2023.2765-2780.pdf)
21. S. Suparno, D. Deswati, W. E. Fitri, H. Pardi, A. Putra, *Environ. Nat. Resour. J.* **22** (2024) 55 (https://doi.org/10.32526/ennrj/22/20230191)
22. E. Hengstmann, M. Tamminga, C. vom Bruch, E. K. Fischer, *Mar. Pollut. Bull.* **126** (2018) 263 (https://doi.org/10.1016/j.marpolbul.2017.11.010)
23. D. A. Syamsu, D. Deswati, S. Syafrizayanti, A. Putra, Y. Suteja, *Glob. J. Environ. Sci. Manage.* **10** (2024) 205 (https://doi.org/10.22034/gjesm.2024.01.14)
24. J. Masura, J. Baker, G. Foster, C. Arthur, *Laboratory Methods for the Analysis of Microplastics in the Marine Environment: Recommendations for quantifying synthetic particles in waters and sediments*, NOAA Technical Memorandum NOS-OR&R-48, Washington, DC, 2015
25. F. A. Febria, A. Syafrita, A. Putra, H. Hidayat, C. Febrion, *Glob. J. Environ. Sci. Manage.* **10** (2024) 805 (https://doi.org/10.22034/gjesm.2024.02.24)
26. D. Deswati, N. D. Wisna, R. Zein, O. N. Tetra, S. Suparno, H. Pardi, Y. Suteja, *AACL Bioflux* **16** (2023) 381 (http://www.bioflux.com.ro/docs/2023.380-397,.pdf)
27. D. Deswati, R. Zein, I. P. Bunda, A. Putra, S. Suparno, *Pollution* **10** (2024) 90 (https://doi.org/10.22059/poll.2023.361556.1973)

28. G. Filippini, K. A. Dafforn, A. B. Bugnot, *Environ. Pollut.* **316** (2023) 120614 (https://doi.org/10.1016/j.envpol.2022.120614)
29. GESAMP, *Guidelines for the monitoring and assessment of plastic litter in the ocean*, International Maritime Organization, London, 2019
30. G. Vandermeersch, L. Van Cauwenberghe, C. R. Janssen, A. Marques, K. Granby, G. Fait, M. J. J. Kotterman, J. Diogène, K. Bekaert, J. Robbens, L. Devriese, *Environ. Res.* **143** (2015) 46 (https://doi.org/10.1016/j.envres.2015.07.016)
31. W. C. Ayuningtyas, D. Yona, S. H. J. S, F. Iranawati, *J. Fish. Mar. Res.* **3** (2019) 41 (https://doi.org/10.21776/ub.jfmr.2019.003.01.5)
32. J. P. G. L. Frias, R. Nash, *Mar. Pollut. Bull.* **138** (2019) 145 (https://doi.org/10.1016/j.marpolbul.2018.11.022)
33. M. González-Hernández, C. Hernández-Sánchez, J. González-Sálamo, J. López-Darias, J. Hernández-Borges, *Mar. Pollut. Bull.* **150** (2020) 110757 (https://doi.org/10.1016/j.marpolbul.2019.110757)
34. R. Leiser, G. M. Wu, T. R. Neu, K. Wendt-Potthoff, *Water Res.* **176** (2020) 115748 (https://doi.org/10.1016/j.watres.2020.115748)
35. C. Li, R. Busquets, L. C. Campos, *Sci. Total Environ.* **707** (2020) 135578 (https://doi.org/10.1016/j.scitotenv.2019.135578)
36. Q. Li, C. Ma, Q. Zhang, H. Shi, *Curr. Opin. Food Sci.* **40** (2021) 192 (https://doi.org/10.1016/j.cofs.2021.04.017)
37. L. Van Cauwenberghe, L. Devriese, F. Galgani, J. Robbens, C. R. Janssen, *Mar. Environ. Res.* **111** (2015) 5 (https://doi.org/10.1016/j.marenvres.2015.06.007)
38. Y. Liu, Y. Lin, J. Xie, P. Li, Y. Zhou, P. Wang, Y. Wu, *Bull. Environ. Contam. Toxicol.* **110** (2023) 96 (https://doi.org/10.1007/s00128-023-03726-4)
39. T. T. T. Vu, D. T. Nguyen, N. T. M. Nguyen, M. N. Nguyen, *Mar. Pollut. Bull.* **185** (2022) 114317 (https://doi.org/10.1016/J.marpolbul.2022.114317)
40. A. M. Abdelghany, M. S. Meikhail, N. Asker, *Integr. Med. Res.* **8** (2019) 3908 (https://doi.org/10.1016/j.jmrt.2019.06.053)
41. W. Fu, J. Min, W. Jiang, Y. Li, W. Zhang, *Sci. Total Environ.* **721** (2020) 137561 (https://doi.org/10.1016/j.scitotenv.2020.137561)
42. X. Yan, Z. Cao, A. Murphy, Y. Qiao, *J. Environ. Chem. Eng.* **10** (2022) 108130 (https://doi.org/10.1016/j.jece.2022.108130)
43. M. Munoz, D. Ortiz, J. Nieto-Sandoval, Z. M. de Pedro, J. A. Casas, *Chemosphere* **283** (2021) 131085 (https://doi.org/10.1016/j.chemosphere.2021.131085)
44. F.-F. Liu, G.-Z. Liu, Z.-L. Zhu, S.-C. Wang, F.-F. Zhao, *Chemosphere* **214** (2019) 688 (https://doi.org/10.1016/j.chemosphere.2018.09.174)
45. S. H. Joo, Y. Liang, M. Kim, J. Byun, H. Choi, *Environ. Challenges* **3** (2021) 100042 (https://doi.org/10.1016/j.envc.2021.100042)
46. C. Mejías, J. Martín, J. L. Santos, I. Aparicio, E. Alonso, *Environ. Technol. Innov.* **32** (2023) 103276 (https://doi.org/10.1016/j.eti.2023.103276)
47. W. Li, B. Zu, Q. Yang, J. Guo, J. Li, *RSC Adv.* **13** (2023) 15566 (https://doi.org/10.1039/d3ra02169f).

Journal of the Serbian Chemical Society
JSCS@tmf.bg.ac.rs • www.shd.org.rs/JSCS
J. Serb. Chem. Soc. 90 (6) S227–S228 (2025) *Supplementary material*

SUPPLEMENTARY MATERIAL TO

Microplastic accumulation and reduction in shellfish (*Polymesoda bengalensis*) using NaCl solution

DESWATI DESWATI[1]*, EMRIADI EMRIADI[1], SELFI MONICA AURA[1], WIYA ELSA FITRI[2], SUPARNO SUPARNO[3] and ADEWIRLI PUTRA[4]

[1]Department of Chemistry, Faculty of Mathematics and Natural Science andalas University, Padang, 25163, Indonesia, [2]Department of Public Health, Syedza Saintika University, Padang, 25132, Indonesia, [3]Departement of Fisheries Resources Utilization, Faculty of Fisheries and Marine Sciences, Bung Hatta University, Padang, 25133, Indonesia and [4]Department of Medical Laboratory Technology, Syedza Saintika University, Padang, 25132, Indonesia

J. Serb. Chem. Soc. 90 (6) (2025) 803–821

SAMPLING AND SAMPLE COLLECTION SITE SELECTION

The details about sample collection are given in the Supplementary material to this paper.

Sampling activities were carried out at three different locations, namely: 1) Batang Arau River Estuary, Padang City, West Sumatra, Indonesia (0° 57'58.4" S; 100° 21'08.7" E); 2) Bungo Pasang River Estuary, Padang City, West Sumatra, Indonesia (0° 51'54.7" S; 100° 20'02.7" E); 3) North Punggasan River Estuary, South Pesisir Regency, West Sumatra, Indonesia (1° 53'04.5" S; 100° 50'37.6" E), shown in Fig 1. Sediment samples were taken at the same place as the shellfish samples using a shovel and homogenized. Next, please put it in a glass bottle, store it in a cool box and take it to the laboratory.[16]

Description of sampling site selection: (1) Batang Arau River Estuary, this estuary is situated in a densely populated area and serves as a hub for tourism and fishing activities, including a port and fish auction center. High levels of activities, such as water-based tourism and household waste, contribute significantly to plastic waste, making it a location with high potential for microplastic accumulation. Consequently, Batang Arau is a key focus in contamination analysis; (2) Bungo Pasang River Estuary, this area experiences moderate anthropogenic activity, surrounded by residential neighborhoods and small-scale industries. Although the potential for microplastic contamination exists, it is lower than in Batang Arau. Bungo Pasang was selected to assess microplastic accumulation in an area with moderate human activity; (3) North Punggasan River Estuary, located along the coast in a region with minimal human activity, North Punggasan is far from industrial areas and tourist centers. Microplastic levels are expected to be low; however, it is included as a comparison site to assess possible contamination from other areas through ocean currents.

* Corresponding author. E-mail: deswati@sci.unand.ac.id

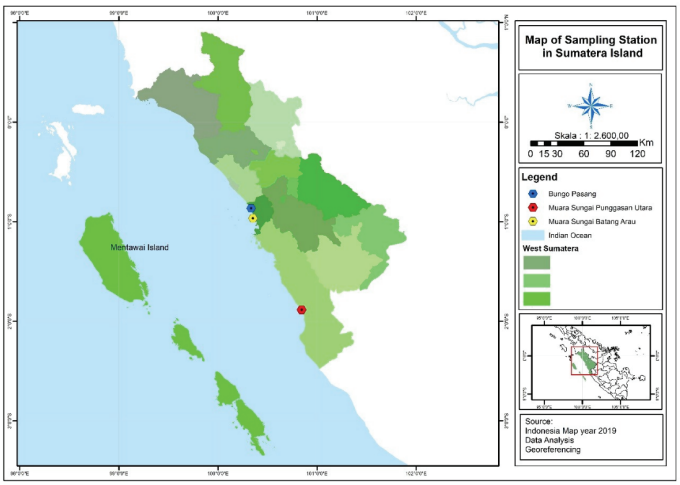

Fig S-1. Research sampling location in the waters of West Sumatra, Indonesia.[1]

Sampling period

Samples were collected during periods of peak human activity, in June of 2023, such as holiday seasons or market days, to provide an accurate assessment of MP accumulation based on activity intensity. This approach aids in understanding contamination variation across locations relative to time and human activity levels.

Sediment sampling

Sediment samples were collected from three locations (Batang Arau River Estuary, Bungo Pasang and North Punggasan) within a 1×1 meter area at each site. Sediment was taken from multiple points within this area down to a depth of 5 cm using a metal shovel, then homogenized in the field to ensure an even distribution of microplastics. Each site was selected based on the level of human activity and a total of 100 g of homogenized sediment was collected from each location to provide a representative analysis of MP contamination.

REFERENCEES

1. Indonesia Geospasial, Region of West Sumatra, Indonesia, *Indonesia Geospasial: Sistem Informasi Geografi & Penginderaan Jauh*, https://www.indonesia-geospasial.com/ (accessed: April 23, 2023).

Journal of the Serbian Chemical Society
JSCS@tmf.bg.ac.rs • www.shd.org.rs/JSCS
J. Serb. Chem. Soc. *90* (6) 823–836 (2025)
JSCS–5423
Original scientific paper
Published 24 June, 2025

Field experiment on the uptake of lead, strontium, cobalt and nickel in the wood and bark of spruce (*Picea abies* L.) and Douglas-fir (*Pseudotsuga menziesii* Mirb.)

IVANA R. MILOŠEVIĆ[1]*, SANJA ŽIVKOVIĆ[2], MILOŠ MOMČILOVIĆ[2], ŽELJKA VIŠNJIĆ-JEFTIĆ[3], MILORAD VESELINOVIĆ[4], IVANA D. MARKOVIĆ[5] and DRAGAN M. MARKOVIĆ[1]

[1]*Institute of Physics Belgrade, University of Belgrade, Pregrevica 118, 11080 Belgrade, Serbia,* [2]*Institute of Nuclear Sciences Vinča, University of Belgrade, Mike Petrovića Alasa 12–14, 11351 Belgrade, Serbia,* [3]*Institute for Multidisciplinary Research, University of Belgrade, Kneza Višeslava 1, 11090 Belgrade, Serbia,* [4]*Institute of Forestry, Kneza Višeslava 3, 11090 Belgrade, Serbia and* [5]*Worldwild Clinical Trials, Omladinskih brigada 90b, 11070 Belgrade, Serbia*

(Received 25 September, revised 13 December 2024, accepted 12 January 2025)

Abstract: Human activities have significantly altered the availability and circulation of pollutants, impacting their concentrations in the environment. This pollution notably affects trees. In this study, we conducted two separate experiments (I and II) to investigate the uptake of lead, strontium, cobalt, and nickel in spruce (*Picea abies* L.) and Douglas-fir (*Pseudotsuga menziesii* Mirb.) seedlings. These seedlings were exposed to elevated levels of these metals by adding them to the soil. Our field experiments provide insights into metal accumulation in natural environments. We measured concentrations of these elements, along with manganese and zinc, in the soil, wood, and bark using inductively coupled plasma-optical emission spectrometry (ICP-OES). The results showed increased levels of the added metals in the wood and bark of both tree species. Notably, there was a significant increase in lead and nickel concentrations in Douglas-fir wood. The lead concentration in Douglas-fir wood was 7 and 4 times higher in experiments I and II, respectively, compared to the control group of seedlings, while the nickel concentration was 18 and 10 times higher. These findings suggest that Douglas-fir wood has potential for phytostabilization of lead and nickel based on trace element concentrations and transfer factors.

Keywords: accumulation; trace elements; tree seedlings; phytostabilization; transfer factors.

* Corresponding author. E-mail: novovic@ipb.ac.rs
https://doi.org/10.2298/JSC240925009M

INTRODUCTION

Modern development and urbanization have led to the production of various pollutants, including trace elements, organic and inorganic compounds and pesticides, which can persist in the soil and harm the environment and human health. Trace elements are particularly disturbing due to their toxicity and resistance to natural degradation, accumulating in plants, animals and the environment over time.[1] Vascular plants serve as valuable indicators of environmental pollution. Different tree parts, such as leaves/needles, seeds, bark, and tree-rings, are used to monitor trace element contamination.[2–6] Trees, with their high biomass production, long vegetation periods, strong root systems and ability to tolerate and remediate pollutants, are effective in extracting trace elements.[7] This process, known as phytoextraction, helps prevent these elements from leaching into deeper soil layers and groundwater.

The bioavailability of metals to plants is influenced by their micronutrient demand and their ability to exude and eliminate toxic elements. Metal accumulation in plants is affected by the distribution of elements in different tissues, the presence of elements with similar physiochemical properties in the soil, the availability of elements in the soil, site conditions and tree species.[1] Metals with similar properties, such as ion size and charge, compete for binding sites in plants, affecting their uptake, translocation and accumulation.[8] Tree species also influence soil pH, impacting trace element availability. The release of organic acids and hydrogen ions from tree roots increases metal ion solubility and uptake.[8] Plants absorb trace elements through their roots and above-ground parts, like leaves and bark, with root uptake being the primary pathway for metals to enter trees.

Metal uptake generally increases as the concentration of metal ions in the external solution increases.[9] However, excessive concentrations of trace element in the soil can trigger protective mechanisms in plants that inhibit the absorption.[10] Therefore, the migration and accumulation of each metal within a tree involve individual and sophisticated biochemical processes and various transportation systems.[11] While the biological function of elements like Pb and Sr in higher plants is unknown and likely toxic, Ni is a part of the enzyme urease.[12] and Co is essential for several enzymes and coenzymes in higher plant systems.[13] The accumulation of trace elements in wood and bark has not been extensively studied, especially through field experiments. Donnelly *et al*. (1990) investigated lead mobility in red spruce seedlings, focusing on whether Pb ions remained in the xylem during uptake.[14] Numerous studies have focused on the uptake and translocation of radionuclides in plants, with a majority of them focused on the bark and foliar surfaces.[15,16] Metal mobility in plants depends on their metabolic function, background metal levels, and the dosage applied to foliar surfaces. Some studies have examined the toxic effects of trace element salts on tree growth and their potential for phytoextraction and phytostabilization.[10,17–20]

However, there is a significant research gap in studying trace element accumulation in wood and bark through field experiments. Furthermore, diverse trace elements accumulate at varying degrees within distinct plant species and parts, emphasizing the significance of understanding the levels of trace elements in plants. The investigation of Douglas-fir plant species in this regard remains insufficient. Studies that are based on collecting data about the accumulation of specific trace element in plants and their distribution among plant parts must be continued and diversified.[21]

The study aimed to investigate how elevated levels of Pb, Sr, Co, and Ni in soil affect their accumulation in spruce and Douglas-fir trees under natural conditions. This field experiment focused on trace element accumulation in wood and bark, with soil metal concentrations as the only variable. The research sought to understand how these metals are absorbed by the trees and to compare the sensitivity of spruce and Douglas-fir to Pb, Sr, Co and Ni, evaluating their potential for trace element accumulation.

EXPERIMENTAL

Study site and experimental design

Details about the study site and experimental design are given in the Supplementary material to this paper.

Amount of added metals

In experiment I, spruce and Douglas-fir seedlings were watered monthly with a solution containing 2 g L^{-1} of Pb and Sr, as well as 0.5 g $L^{-1}$of Co and Ni. In experiment II, the solution contained half of these concentrations. Seedlings were watered with tap water during the experiment. Metal solutions were prepared monthly using nitrate salts (all purchased from Merck: lead(II) nitrate $Pb(NO_3)_2$; strontium(II) nitrate $Sr(NO_3)_2$; cobalt(II) nitrate hexahydrate $Co(NO_3)_2{\cdot}6H_2O$ and nickel(II) nitrate hexahydrate $Ni(NO_3)_2{\cdot}6H_2O$) dissolved in tap water. Seedlings were watered for five months with solutions achieving concentrations of 2 g L^{-1} Pb and Sr and 0.5 g L^{-1} Co and Ni for the first experiment, and 1 g L^{-1} Pb and Sr, and 0.25 g L^{-1} Co and Ni for the second experiment. Total metal added was 10 mg $g^{-1}$of Pb and Sr and 2.5 mg g^{-1} of Co and Ni for experiment I, and half of that for experiment II, and those concentrations are total amounts to which plants were exposed in this experiment. All trees survived with normal growth and no signs of metal toxicity.

Sample preparation and experiment

To simplify the results, spruce and Douglas-fir trees from the first experiment are labelled “SI” and “DI”, and from the second experiment, “SII” and “DII”. Control groups are labeled “SC” and “DC”.

Four seedlings of each species were cut, and 1 cm stem disks were sampled from 10 cm above the base (Fig. S-1d of the Supplementary material), along with bark and soil samples taken from 0–20 cm depth. Most of the fine roots of trees are found in the surface soil layer at this depth.[22] Soil before plantation was also collected to obtain the amount of the metal content in the soil before the field experiment. Tree wood, bark and soil were digested using an advanced microwave digestion system (Ethos 1, Milestone, Italy). Sample digestion in the Ethos 1 followed standard manufacturer-recommended programs, with the official software

optimizing chemical volumes, temperature and pressure based on sample type and mass. About 0.5 g of powdered oven-dried samples, of spruce and Douglas-fir, were precisely weighed and mixed in the clean vessel with a mixture of 3 mL 30 % H_2O_2 (Suprapur®, Germany) and 5 mL 65 % HNO_3 (Suprapur®, Germany) and then heated with microwave energy, (with parameters t = 200 °C, KW = 1800 W, τ = 15 min and p = 90 bar). The soil was first dried at room temperature and then in order to ensure the homogeneity of soil samples, each of the samples was divided into six equal parts from which the same amount of soil was taken. This amount of soil was sieved through a plastic sieve, and then ground in a mortar to a powdery particle size. The sample was then dried in an oven to constant weight at a temperature of 60 °C. Soil samples (0.5 g) from each part of the experiment were thoroughly mixed before analysis to ensure a homogenous concentration, accurately measured, and placed in clean microwave preparation vessels with 8 mL 65 % HNO_3 (Suprapur®, Germany) and 2 mL 36 % HCl (Suprapur®, Germany). The parameters of the soil preparation program were the same as for the preparation of plant tissues. The temperature was controlled with a predetermined power program. After cooling and without filtration, the solution was diluted to a fixed volume of 25 mL. Quality control was assured by the use of procedural blanks. Precision and accuracy were confirmed by repeated analysis of NIST pine needles (1575a) as standard reference material.

The content of elements (Pb, Sr, Co, Ni, Mn and Zn) in each sample, prepared as diluted aqueous solutions, was quantified by inductively coupled plasma optical emission spectrometry-ICP-OES using a Thermo Scientific iCAP 7400 duo analyzer (Thermo Fisher Scientific Inc.). The calibration standard solutions were prepared from a Multi-element ICP IV standard stock solution (Merck). For each element determined, calibration curves were constructed and used to determine the analyte concentrations. The data acquisition and processing were performed by the Thermo Scientific Qtegra platform software. All measurements were carried out in triplicates. The pH of the soil was determined using a glass electrode (1741, La Motte Tracer-PockeTester) in a 1:5 (volume fraction) suspension of soil in deionized water. 2 g was precisely weighted, and 10 mL of deionized water was added. The suspension was stirred on a stirrer for 30 min and left for another 30 min to stand before pH measuring. The chemical analysis results were evaluated using One-Way ANOVA to compare the three groups (experiments I and II and control) for both tree species, followed by Tukey's test to identify specific group differences. Differences were considered statistically significant at the 0.05 level.

Transfer factor

The capacity of trees to extract trace elements from soil and their translocation to aboveground tissues can be evaluated by calculating the transfer factor, *TF*. Different calculations for transfer factors can be seen in the literature and most of them divide the average trace element concentration in the plant part by the concentration in soil.[23,24] Most of them showed only elevated concentrations of specific metals compared to soil or biogeochemical comparison of metals in different media (plant and soil) that occur under the same circumstances.[25] It does not show how the metal transfer from soil to plant changed on the treated site compared to the control site.[25] Including the control site (where natural processes affect metal transfer from soil to plant) in the calculations, we can get information about changes in transfer processes.[25] To investigate the transfer of externally added metals-to-soil (TF_{soil}); soil-to-wood transfer (TF_{wood}) and soil-to-bark transfer (TF_{bark}), for this experiment, *TF* was calculated (in %) by the following equations:

$$TF_{soil} = 100(I–C)_{soil}/EA \quad (1)$$

$$TF_{wood} = (I–C)_{wood}/(I–C)_{soil} \quad (2)$$

$$TF_{bark} = (I–C)_{bark}/(I–C)_{soil} \quad (3)$$

where I and C represent the mean Pb, Sr, Co and Ni concentrations obtained in the first experiment and control for two examined coniferous species (S and D), while EA is externally added concentration of metals examined. The same equations were used for the experiment II.

RESULTS AND DISCUSSION

Concentration of Pb, Sr, Co, Ni, Mn and Zn in soil, wood and bark of spruce and Douglas-fir seedlings

Mean Pb, Sr, Co and Ni concentrations in soil, wood, and bark of spruce and Douglas-fir seedlings are presented in Table I which were externally added in this field experiment. Also, mean Mn and Zn concentrations in soil, wood and bark and the measured pH of the spruce and Douglas-fir corresponding soils can be seen in Table I. Soil concentrations measured before plantation and performed field experiment were 21±1 μg g^{-1} for Pb, 78±4 μg g^{-1} for Sr, 22±1 μg g^{-1} for Co, 87±5 μg g^{-1} for Ni, 822±42 μg g^{-1} for Mn, and 118±5 μg g^{-1} for Zn. Maximally allowed concentrations in the soil for Pb, Co, Ni and Zn in the Republic of Serbia are 85, 9, 35 and 140 μg g^{-1}.[26] Soil concentrations of Co and Ni, both before planting and in the control samples, exceed the maximum levels permitted by the Regulation, likely reflecting the geochemical conditions of the experimental area. Additionally, air pollution cannot be ruled out, given the moderate traffic, residential heating, and the proximity to the largest waste dump in Vinča, which is the only landfill in the Belgrade city area.

Soil concentrations before plantation were as control concentrations (SC and DC) measured after metal addition in experiments I and II (Table I). Thus, levels of the metals of interest in the soil before additional metal watering were as in control, excluding the possibility of metal transfer from one experiment to another. Elevated concentrations in the soil (Table I) externally added did not affect plant growth during this 2-year experiment. Higher mean Pb, Sr, Co and Ni concentrations for bark can be seen for both examined tree species, than in their wood compartments (Table I).

Mean differences of Pb, Sr, Co and Ni for soil and bark of both examined species were significant, at the 0.05 level, between parallel experiments and control (one-way ANOVA), except for the Pb concentration in SII for bark. In the case of wood, mean differences were significant for Pb, Sr and Ni, except between Ni SII concentration and control. For some soil, wood, and bark mean differences between the I and II experiments weren't significant (Tukey test). For the pH, mean differences were significant, at the 0.05 level, between the II experiment and control for both tree species. Mean differences of Mn and Zn for soil, wood and bark of both examined species were significant, at the 0.05 level, between parallel experiments and control (one-way ANOVA, Tukey test), except

for the Douglas-fir DII and DC and spruce SI and SII soil Zn concentration. In some cases, for soil, wood and bark the mean differences weren't significant between the I and II experiment.

TABLE I. Mean Pb, Sr, Co, Ni, Mn and Zn (n = 4) concentrations (μg g^{-1}) in soil, wood and bark seedlings of spruce first experiment-SI; second experiment-SII; control-SC; Douglas-fir first experiment-DI; second experiment-DII and control-DC, as well as corresponding soil pH

Experiment	Pb			Sr		
	Soil	Wood	Bark	Soil	Wood	Bark
SI	827±56	0.41±0.05	4.73±0.55	680±51	101±7	256±13
SII	505±30	<0.15	1.87±0.09	325±19	54.39±3.45	246±13
SC	21±1	<0.15	1.67±0.10	75±4	31.53±1.89	81±5
DI	634±30	1.06±0,10	2.44±0.13	371±21	46.37±3.68	197±13
DII	369±19	0.61±0,08	1.28±0.06	301±15	44.32±2.72	154±9
DC	23±1	<0.15	0.68±0.05	77±4	15.85±1.07	26±2
	Co			Ni		
	Soil	Wood	Bark	Soil	Wood	Bark
SI	97±6	<0.04	0.44±0.04	278±16	0.34±0.03	2.71±0.16
SII	73±4	<0.04	0.32±0.02	199±9	0.29±0.04	1.78±0.09
SC	20±1	<0.04	0.12±0.02	88±4	0.24±0.03	1.09±0.09
DI	84±6	<0.04	0.27±0.04	226±11	0.73±0.06	1.13±0.06
DII	63±3	<0.04	0.23±0.04	182±9	0.40±0.03	1.03±0.06
DC	21±2	<0.04	<0.04	89±4	<0.04	0.36±0.04
	Mn			Zn		
	Soil	Wood	Bark	Soil	Wood	Bark
SI	950±43	8.23±0.46	18.7±1.4	128±6	18.0±0.9	67.9±3.9
SII	923±42	8.41±0.49	23.4±1.9	125±5	21.5±1.0	73.4±4.4
SC	823±42	9.22±0.57	28.9±1.9	118±7	28.4±1.6	100±5
DI	951±43	3.38±0.23	13.7±0.9	131±7	5.36±0.37	22.0±1.9
DII	954±43	2.63±0.20	12.0±0.6	122±5	3.52±0.19	25.0±1.4
DC	852±46	5.00±0.27	8.71±0.44	113±5	7.66±0.38	30.4±1.6
	SI	SII	SC	DI	DII	DC
Soil pH	6.7±0.05	6.6±0.05	6.8±0.05	6.9±0.05	6.7±0.05	7.0±0.05

Pb and Sr concentration

From Fig. 1a, it can be seen, for spruce, that the Pb content in the soil increases, and the increase is about 40 (SI) and 24 (SII) times, compared to the control soil sample. This implies an elevation of Pb concentration in the SI wood and barks for SI and SII, compared to the control (Table I). The increase was 2.8 times for SI wood and 2.8 and 1.1 times for SI and SII in the bark, respectively (Fig. 1a). Comparing the concentrations of SI and SII (Fig. 1b) for Pb in soil, wood, and bark we obtain an increased concentration in the SI experiment of about 1.6, 2.8, and 2.5 times, respectively. Increased Sr content in the soil from 75 to SI-680 μg g^{-1} and SII-325 μg g^{-1} (9 and 4 times higher compared to control) directly influences the increase of Sr concentration in the spruce wood and

bark (Table I; Fig. 1a). The concentration of Sr in the soil was about twice as high if we observe the ratio between the I and II experiment (Fig. 1b). Also, the concentration of Sr in wood is almost twice as high, ie. about 1.9 times (86 %). In the bark, this increase between the I and II experiment is about 4 % (Fig. 1b).

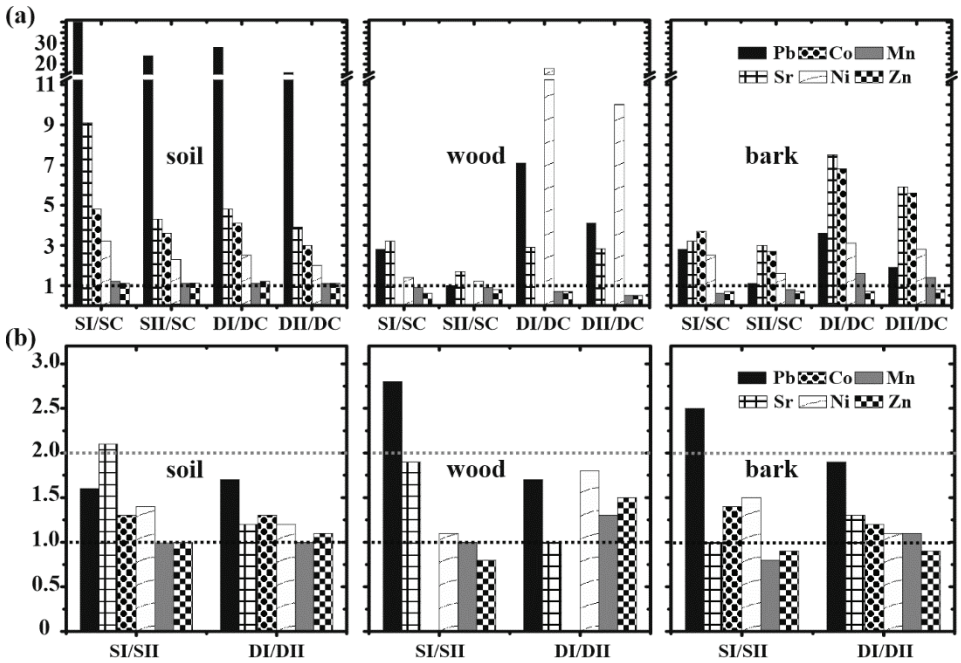

Fig. 1. Concentration ratios in soil, wood and bark: a) between the I and II experiment compared to the control and b) between the first-I and second-II experiment, for spruce-S and Douglas-fir-D. (Black line indicates a ratio of 1, representing no change in concentration, gray line represents a ratio of 2, suggesting that accumulation aligns with the two times higher externally added concentration for the I experiment; concentration ratios for cases where the detection limit was measured in the control-C were calculated using the value of the detection limit.).

In the case of Douglas-fir, it was noticed that with the increase of Pb concentration in the soil of 28 (DI) and 16 (DII) times, compared to control, the content in wood (7 and 4 times) and bark (4 and 2 times) also increases (Fig. 1a), Table I). An increase in the soil Pb content of 72 % between parallel experiments contributes to the increase of Pb in the wood of about 74 %, and the bark of about 91 %. The higher content of Sr in the soil (Table I) parallel experiments (5 and 4 times compared to control), as well as in the case of spruce, implies the higher content in Douglas-fir wood (3 times for both experiments) and bark (8 and 6 times). An increase of the Sr concentration in the soil for the I experiment of

about 23 % (1.2 times) compared to the II experiment indicates that Sr content in wood is increased by about 5 % and in the bark by 28 %.

Co and Ni concentration

Elevated Co content in soil samples (5 and 4 times higher compared to control in the case of spruce, and 4 and 3 times for Douglas-fir) had an effect on increasing the concentration in the bark (4 and 3 times compared to control for spruce, and 7 and 6 times in the case of Douglas-fir) but not on wood where Co concentration was below the detection limit (Fig. 1a, Table I). Therefore, based on this experiment, the wood of spruce and Douglas-fir are not a good choice for Co. Increased Ni concentration in soil samples (3 – SI and 2 – SII times; 2.5 – DI and 2 – DII times compared to control) also have a direct effect on increasing the concentration (Fig. 1a, Table I) in both wood (1.4 – SI and 1.2 – SII times; 18 – DI and 10 – DII times compared to control) and bark (2.5 – SI and 2 – SII times; 3 – DI and 3 – DII times compared to control). About 40 % higher content of Ni in the soil was detected and about 14 % higher concentration for wood and about 52 % for the bark compared to the II experiment in the case of spruce. For Douglas-fir, it was 24 % for soil, 83 % for wood and 10 % for bark.

Mn and Zn concentration

Mn and Zn were examined because they are, among other elements, essential for higher plants and have several functions in plants.[13] As these elements weren't added in this experiment, differences compared to control are minimal, with most ratios near 1 (Fig. 1a). Some phenomena can be seen in this experiment for the examined tree species. Their concentrations in wood and bark compared to control (Table I; Fig. 1a) which slightly decreased (except for the Mn concentration in Douglas-fir bark, which increased), despite slightly higher soil concentrations (Table I).

Slight soil concentration increases for Mn (15, 12 %) and Zn (9, 6 %) in spruce and Mn (12, 12 %) and Zn (15, 7 %) in Douglas-fir soil in I and II experiments compared to control that was observed could be the consequence of the soil pH change.[2] Other factors, such as the impact of specific tree species on soil pH and the addition of heavy metals to the soil, can also influence the adsorption dynamics of essential elements by competing with or altering the total organic content (*TOC*) during root uptake. Externally added heavy metals can interact with *TOC*, affecting the behavior and availability of Mn and Zn. The effect of *TOC* on Mn and Zn uptake may differ between tree species due to variations in root systems, uptake mechanisms, and tolerance to nutrient imbalances. However, these aspects were not measured in this study. In SI and SII the pH decrease was 0.1 and 0.2; and in DI and DII it was 0.1 and 0.3, respectively, compared to the control pH value. The decrease of Mn for spruce in parallel experiments (SI

and SII) expressed as a percentage compared to control was 11, 9 % for wood and 35, 19 % for bark, respectively. In the case of Zn, it was 37, 24 and 32 %, 27 %, respectively. For Douglas-fir wood, the decrease of Mn concentration was 32, 48 %, and the decrease of Zn concentration was 30, 54 % for wood and 27, 18 % for bark, respectively.

Studies indicate that trace elements move differently between tree organs across different tree species,[5,20,27–29] and plants retain trace elements at varying levels.[6] Traffic is a significant source of Pb, Ni and Zn pollution,[21,30] with Ni entering the atmosphere through fuel combustion, mining and urban waste burning, while Co is mainly used in rechargeable batteries for electronics.[31] The elevated Ni levels at the control site in our experiment may be due to these factors. Pb concentration in the control soil were below regulatory limits in Serbia and similar to road dust levels in areas with moderate traffic and residential heating contributing to pollution.[30] Thus, observed elevated Pb and Ni in wood and bark from both species are direct outcome of our experiments suggesting that bark and wood, especially of Douglas-fir, can collect and remediate these metals. The wood samples examined came from seedlings (with stem disks of 1 cm height and a volume of about 3.14 cm^3). If we scale this to mature trees (with 10 times the volume), we estimate that about 4.1 and 3.4 μg g^{-1} of Pb and Ni could be collected by spruce and 10.6 and 7.3 μg g^{-1} by Douglas-fir, with higher values possible when considering the full trunk. Several studies have shown elevated levels of trace elements in plants and soil in areas affected by air pollution,[5,6,31] but there is limited information on the trace element accumulation potential of many plant species. Research on Scots pines in Finland showed that Ni accumulates in wood,[29] while most elements are stored in roots.[17,18,20] Although roots were not examined, trace elements clearly moved from soil to wood and bark. Given the toxicity of Pb, Ni and Co, and their detrimental health effects with prolonged exposure,[31] it is crucial to extract these elements from the environment. Spruce and Douglas-fir could be used to phytostabilize trace elements in soil, reducing their mobility and leaching. An indication is that the addition of other metals to the soil and their accumulation in the body of wood and bark influence essential elements, and lead to a decrease in their plant parts. Higher Mn concentrations in background trees compared to those grown on sludge were found in tree seedlings.[32] Similarly, in beech roots a decrease in mineral cations (K, Ca, Mg, and Mn) was observed with increasing Pb and Cd in soil.[33] Prolonged exposure to elevated heavy metal levels, as suggested by our findings, could further reduce nutrient levels in plants and potentially lead to plant death over time. However, this conclusion requires further research beyond this experiment. The observed decrease in Mn and Zn may also result from competition between metals during root uptake, as Ni^{2+} and Zn^{2+} have similar physical and

chemical properties,[12] leading to reduced Zn levels in wood and bark due to elevated Ni in the soil.

The impact of tree species on soil pH is important, as it influences trace elements availability to plants. The effect of different tree species on soil pH is most significant in the first 10 cm of the topsoil.[34] Topsoil pH was lower under *P. abies*, while *P. menziesii* appeared to be intermediate.[34] In this study, spruce (*P. abies*) had lower pH values than Douglas-fir (*P. menziesi*) in both control and parallel experiments (Table I). As a result, higher soil metal concentrations were observed for spruce (Fig. 1a). However, this did not translate into higher metal accumulation in wood and bark, as Douglas-fir showed greater accumulation, particularly for Ni and Pb (Fig. 1a).

Transfer factors

The capacity of trees to extract trace elements from soil and their translocation to aboveground tissues can be evaluated by calculating the transfer factor, *TF*. Three calculated ratios are presented in Fig. 2.

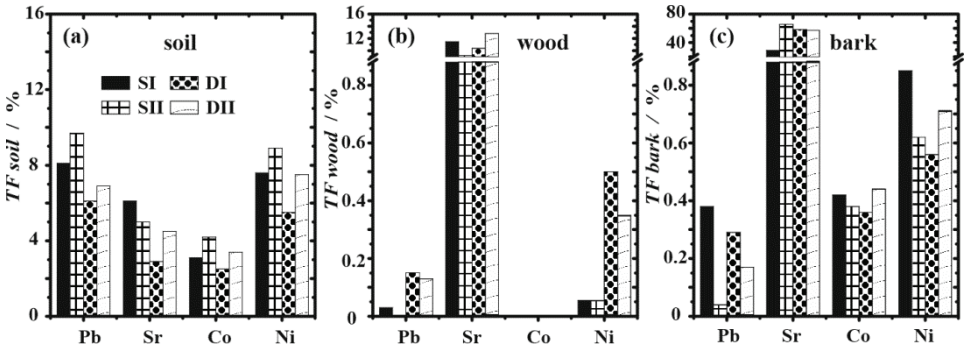

Fig. 3. Calculated transfer factors for spruce (S) and Douglas-fir (D), *TF*; a) for soil-TF_{soil}, b) wood-TF_{wood} and c) bark-TF_{bark}, expressed as a percentage.

Only a small amount (less than 10 %) of the externally added elements (EA) in the soil were in a form that is available and can be absorbed by roots and translocated throughout the plant (Fig. 2a) in these experiments. The smallest percentage of TF_{soil} was for DI Co concentration and the highest was in the case of SII Pb concentration (Fig. 2a). Generally looking, the second experiment had greater TF_{soil} probably due to the greater change in soil pH for both species. Lower pH increases the metal availability due to competition between hydrogen ions and metal ions at the uptake sites in the roots.[9] In wood and bark (Fig. 2 b and c), *TF*'s are less than 1 % (except for Sr) and the highest *TF*s are for Sr, in both species. The Sr is chemically related to Ca and plant roots normally do not discriminate between absorption of Ca^{2+} and Sr^{2+} from nutrient solutions.[23] This could be the reason for elevated *TF* in wood and bark for Sr (Fig. 2b and c).

Higher available Sr concentration in the soil in these experiments probably competes with the Ca concentration (a very important macronutrient for higher plants). Calculated TF_{wood} are greater in Douglas-fir than in spruce wood for examined elements and Ni and Pb in Douglas-fir stand out. Nickel is attributed to mobile elements,[25,32] and Ni uptake in our experiments confirms its high mobility. Pine, birch and black alder most efficiently took up Zn and Ni.[24] Although available soil concentrations of Pb compared to control (Fig. 1a) are higher than for Ni, transfer factors in wood for Ni are greater. In the case of bark, transfer factors are more pronounced than in wood. The highest TF_{bark} is for Sr, then Ni, Co and Pb. Also, small differences between spruce and Douglas-fir transfer factors for bark can be seen (Fig. 2c). The bark is intensively used as a bioindicator of atmospheric pollution but uptake of Pb, Sr, Co and Ni by tree root in these experiments indicate to their translocation from the soil to the bark. This pathway has to be taken into consideration in the highly polluted areas like the one where the elements are incorporated into the bark, especially in the case of Co which couldn't be traced in spruce and Douglas-fir wood.

These experiments showed that metals added to natural soils were absorbed by tree roots and transferred to wood and bark within two years under normal conditions. Despite the soil concentration in the first experiment being double that of the second, the increase in metal content in soil, wood, and bark was not proportional. The second experiment had higher soil transfer factors (TF_{soil}) than the first, leading to a ratio of less than 2 between the experiments. Such studies provide valuable insights into heavy metal accumulation and distribution in tree species. Since plants can significantly reduce air pollution, expanding green spaces, this method provides a highly effective solution.

CONCLUSIONS

All spruce and Douglas-fir trees survived and grew normally during the two--year experiment. The general response of the two coniferous species was an increase of elements in wood and bark compared to controls, with only a slight decrease in Mn and Zn. Sr and Ni were absorbed most efficiently. While uptake wasn't directly proportional to soil metal concentrations, both species responded to elevated levels, indicating environmental pollution. Bark was also influenced by the added concentrations in the soil which has to be taken into consideration in highly polluted areas as the significant pathway. Bark, especially for Co, also acted as a useful indicator, unlike wood where Co was not detected. Thus, Douglas-fir wood can serve as a better bioindicator of Pb and Ni than spruce. Despite higher soil metal levels in spruce, Douglas-fir accumulated more Ni (18 and 10 times higher) and Pb (7 and 4 times higher), making it a better bioindicator for these metals. Expanding green spaces is a highly effective way to reduce air pollution, as plants play a significant role.

SUPPLEMENTARY MATERIAL

Additional data and information are available electronically at the pages of journal website: https://www.shd-pub.org.rs/index.php/JSCS/article/view/13064, or from the corresponding author on request.

Acknowledgments. The authors acknowledge funding provided by the Institute of Physics Belgrade, Institute of Nuclear Sciences Vinča and Institute for Multidisciplinary Research, through the grants by the Ministry of Science, Technological Development and Innovation of the Republic of Serbia.

И З В О Д

ТЕРЕНСКИ ЕКСПЕРИМЕНТ О УСВАЈАЊУ ОЛОВА, СТРОНЦИЈУМА, КОБАЛТА И НИКЛА У ДРВЕТУ И КОРИ СМРЧЕ (*Picea abies* L.) И ДУГЛАЗИЈЕ (*Pseudotsuga menziesii* MIRB.)

ИВАНА Р. МИЛОШЕВИЋ[1], САЊА ЖИВКОВИЋ[2], МИЛОШ МОМЧИЛОВИЋ[2], ЖЕЉКА ВИШЊИЋ-ЈЕФТИЋ[3], МИЛОРАД ВЕСЕЛИНОВИЋ[4], ИВАНА Д. МАРКОВИЋ[5] и ДРАГАН М. МАРКОВИЋ[1]

[1]Институт за физику у Београду, Универзитет у Београду, Прегревица 118, 11080 Београд, [2]Институт за нуклеарне науке „Винча“, Универзитет у Београду, Мике Петровића Аласа 12–14, 11351 Београд, [3]Институт за мултидисциплинарна истраживања, Универзитет у Београду, Кнеза Вишеслава 1, 11090 Београд, [4]Институт за шумарство, Кнеза Вишеслава 3, 11090 Београд и [5]Worldwild Clinical Trials, Omladinskih brigada 90b, 11070 Београд

Људске активности су значајно промениле доступност и циркулацију загађујућих материја, утичући на њихове концентрације у животној средини, а загађење посебно утиче на дрвеће. У овој студији, спровели смо два одвојена експеримента (I и II) да бисмо испитали акумулацију олова, стронцијума, кобалта и никла у садницама смрче (*Picea abies* L.) и дуглазије (*Pseudotsuga menziesii* Mirb.). Ове саднице су биле изложене повишеном нивоу наведених метала, додавањем у земљу. Наши теренски експерименти пружају увид у акумулацију метала у природном окружењу. Мерили смо концентрације ових елемената, заједно са манганом и цинком, у земљишту, дрвету и кори користећи индуктивно спрегнуту плазма-оптичку емисиону спектрометрију (ICP-OES). Резултати су показали повећане нивое додатих метала у дрвету и кори обе врсте дрвећа. Приметно је да је дошло до значајног повећања концентрације олова и никла у дрвету дуглазије. Концентрација олова у дрвету дуглазије је била 7 и 4 пута већа у огледима I и II у односу на контролу, док је концентрација никла била 18 и 10 пута већа. Ови резултати, на основу концентрација елемената у траговима и трансфер фактора, сугеришу да дрво дуглазије има потенцијал ка фитостабилизацији олова и никла.

(Примљено 25. септембра, ревидирано 13. децембра 2024, прихваћено 12. јануара 2025)

REFERENCES

1. W. Liu, J. Ni, Q. Zhou, *Mater. Sci. Forum* **743**–**744** (2013) 768 (https://dx.doi.org/10.4028/www.scientific.net/MSF.743-744.768)
2. D. M. Marković, I. R. Milošević, D. Vilotić, *Environ. Sci. Pollut. Res.* **20** (2013) 136 (https://dx.doi.org/10.1007/s11356-012-1024-8)
3. M. Yousaf, K. L. Mandiwana, K. S. Baig, J. Lu, *Water Air Soil Poll.* **231** (2020) 382 (https://dx.doi.org/10.1007/s11270-020-04758-w)
4. W. Kusiak, J. Majka, I. Ratajczak, M. Górska, M. Zborowska, *Forests* **11** (2020) 746 (https://dx.doi.org/10.3390/F11070746)

5. H. Sevik, M. Cetin, A. Ozturk, H. B. Ozel, B. Pinar, *Appl. Ecol. Env. Res.* **17** (2019) 12843 (https://dx.doi.org/10.15666/aeer/1706_1284312857)
6. A. Turkyilmaz, H. Sevik, K. Isinkaralar, M. Cetin, *Environ. Sci. Pollut. R.* **26** (2019) 5122 (https://dx.doi.org/10.1007/s11356-018-3962-2)
7. L. Gómez, A. Contreras, D. Bolonio, J. Quintana, L. Oñate-Sánchez, I. Merino, *Adv. Bot. Res.*, **89** (2019) 281 (https://doi.org/10.1016/bs.abr.2018.11.010)
8. H. Marschner, *Mineral nutrition of higher plants*, Academic Press, London, 1995, p. 313 (https://doi.org/10.1016/C2009-0-02402-7)
9. M. N. V. Prasad, J. Hagemeyer, *Heavy metal stress in plants: From molecules to ecosystems*, Springer-Verlag, Berlin, 1999, p. 1 (ISBN: 3662077450)
10. M. Praspaliauskas, N. Pedisius, A. Gradeckas, *J. For. Res.* **29** (2018) 347 (https://doi.org/10.1007/s11676-017-0455-y)
11. N. Rascio, F. Navari-Izzo, *Plant Sci.* **180** (2011) 169 (https://doi.org/10.1016/j.plantsci.2010.08.016)
12. I. V. Seregin, A. D. Kozhevnikova, *Russ. J. Plant Phys.* **53** (2006) 257 (https://doi.org/10.1134/S1021443706020178)
13. B. J. Alloway, *Heavy metals in soils*, Springer Science & Business Media, Berlin, 2013, p. 196 (https://doi.org/10.1007/978-94-007-4470-7)
14. J. R. Donnelly, J. B. Shane, P. G. Schaberg, *J. Environ. Qual.* **19** (1990) 268 (https://doi.org/10.2134/jeq1990.00472425001900020012x)
15. Z. Q. Lin, N. N. Barthakur, P. H. Schuepp, G. G. Kennedy, *Environ. Exp. Bot.* **35** (1995) 475 (https://doi.org/10.1016/0098-8472(95)00039-9)
16. S. A. Watmough, T. C. Hutchinson, *Environ. Pollut.* **121** (2003) 39 (https://doi.org/10.1016/S0269-7491(02)00208-7)
17. A. Bonet, G. Pascaud, C. Faugeron, M. Soubrand, E. Joussein, V. Gloaguen, G. Saladin, *Int. J. Phytoremediat.* **18** (2016) 559 (https://doi.org/10.1080/15226514.2015.1086297)
18. C. Astier, V. Gloaguen, C. Faugeron, *Int. J. Phytoremediat.* **16** (2014) 790 (https://doi.org/10.1080/15226514.2013.856849)
19. M. S. Günthardt-Goerg, P. Vollenweider, R. Schulin, *Plants* **11** (2022) 523 (https://doi.org/10.3390/plants11040523)
20. O. P. Zhivotovsky, Y. A. Kuzovkina, C. P. Schulthess, T. Morris, D. Pettinelli, *Int. J. Phytoremediat.* **13** (2011) 731 (https://doi.org/10.1080/15226514.2010.525555)
21. H. Cobanoglu, H. Sevik, İ. Koç, *Water Air Soil Poll.* **234** (2023) 65 (https://doi.org/10.1007/s11270-023-06086-1)
22. S.-O. Borgegard, H. Rydin, *J. Appl. Ecol.* **26** (1989) 585 (https://doi.org/10.2307/2404084)
23. D. Butkus, E. Baltrėnaitė, *Ekologija* **53** (2007) 29 (ISSN: 0235-7224)
24. N. Mirecki, R. Agič, L. Šunić, L. Milenković, Z. S. Ilić, *Fresen. Environ. Bull.* **24** (2015) 4212 (ISSN: 1018-4619)
25. E. Baltrėnaitė, A. Lietuvninkas, P. Baltrėnas, *Water Air Soil Pollut.* **223** (2012) 4297 (https://doi.org/10.1007/s11270-012-1192-7)
26. *Official Gazette of the Republic of Serbia*, **64** (2019) 1
27. H. Sevik, M. Cetin, H. Ucun Ozel, H. B. Ozel, M. M. M. Mossi, I. Zeren Cetin, *Environ. Sci. Pollut. R.* **27** (2020) 2423 (https://doi.org/10.1007/s11356-019-06895-0)
28. G. Saladin, in *Soil Biology,* Vol. 44, Springer Science & Business Media, Berlin, 2015, p. 333 (https://doi.org/10.1007/978-3-319-14526-6_18)
29. K. Saarela, L. Harju, J. Rajander, J. Lill, S. Heselius, *Sci. Total Environ.* **343** (2005) 231 (https://doi.org/10.1016/j.scitotenv.2004.09.043)

30. S. N. Istanbullu, H. Sevik, K. Isinkaralar, O. Isinkaralar, *B. Environ. Contam. Tox.* **110** (2023) 1 (https://doi.org/10.1007/s00128-023-03720-w)
31. M. Cetin, A. M. O. Aljama, O. B. M. Alrabiti, F. Adiguzel, H. Sevik, I. Zeren Cetin, *Water Air Soil Pollut.* **233** (2022) 1 (https://doi.org/10.1007/s11270-022-05638-1)
32. D. Butkus, E. Baltrėnaitė, *Ekologija* **53** (2007) 68 (ISSN: 0235-7224)
33. S. W. Breckle, H. Kahle, *Vegetatio* **101** (1992) 43 (https://doi.org/10.1007/BF00031914)
34. L. Augusto, J. Ranger, D. Binkly, A. Rothe, *Ann. Forest. Sci.* **59** (2002) 233 (https://doi.org/10.1051/forest:2002020)
35. K. Isermann, *Handbook of Stable Strontium*, Springer-Verlag, Berlin, 1981, p. 65 (https://doi.org/10.1007/978-1-4684-3698-3_5).

Journal of the Serbian Chemical Society
JSCS@tmf.bg.ac.rs • www.shd.org.rs/JSCS
J. Serb. Chem. Soc. 90 (6) S229–S230 (2025) *Supplementary material*

SUPPLEMENTARY MATERIAL TO

Field experiment on the uptake of lead, strontium, cobalt and nickel in the wood and bark of spruce (*Picea abies* L.) and Douglas-fir (*Pseudotsuga menziesii* Mirb.)

IVANA R. MILOŠEVIĆ[1]*, SANJA ŽIVKOVIĆ[2], MILOŠ MOMČILOVIĆ[2], ŽELJKA VIŠNJIĆ-JEFTIĆ[3], MILORAD VESELINOVIĆ[4], IVANA D. MARKOVIĆ[5] and DRAGAN M. MARKOVIĆ[1]

[1]*Institute of Physics Belgrade, University of Belgrade, Pregrevica 118, 11080 Belgrade, Serbia,* [2]*Institute of Nuclear Sciences Vinča, University of Belgrade, Mike Petrovića Alasa 12–14, 11351 Belgrade, Serbia,* [3]*Institute for Multidisciplinary Research, University of Belgrade, Kneza Višeslava 1, 11090 Belgrade, Serbia,* [4]*Institute of Forestry, Kneza Višeslava 3, 11090 Belgrade, Serbia and* [5]*Worldwild Clinical Trials, Omladinskih brigada 90b, 11070 Belgrade, Serbia*

J. Serb. Chem. Soc. 90 (6) (2025) 823–836

STUDY SITE AND EXPERIMENTAL DESIGN

Details about the study site and experimental design are given in the Supplementary material to this paper.

The field experiment was carried out in Kaluđerica, Belgrade, Serbia, on Livada 1 Street as depicted in Fig. S-1 (a) and (b). Five-year-old spruce (*Picea abies* L.) and Douglas-fir (*Pseudotsuga menziesii* Mirb.) seedlings were obtained from the Institute of Forestry, Belgrade. In May 2017, 24 seedlings were planted across 48 m², divided into six groups, with four seedlings per group (Figure 1c). To prevent metal transfer, seedlings were spaced 1 meter apart. After rooting until January 2018, they were watered five times between January and May 2018 with Pb, Sr, Co, and Ni in two experiments, with the I experiment having double the concentrations of the II experiment. The third group of seedlings served as the control group. In May 2019, the seedlings were harvested.

* Corresponding author. E-mail: novovic@ipb.ac.rs

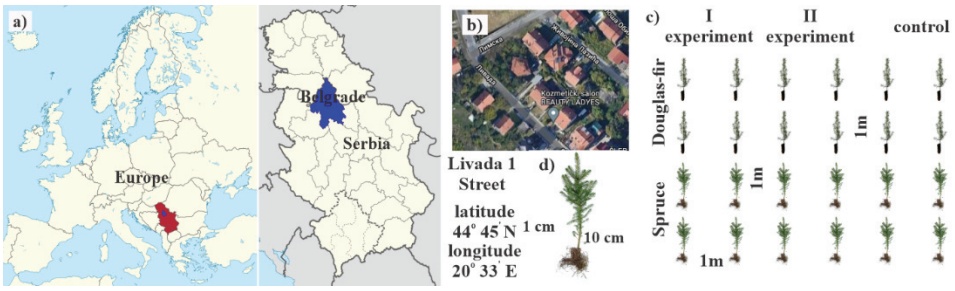

Fig. S-1. a) Sampling location of the performed field experiment, b) Google map of the location with the arrow showing the planted area, c) display of the planted seedlings with two parallel field experiments and control and d) display of the wood sampling.